Optimised self-calibrating microfluidic systems towards design optimisation

Nile Quane

A thesis presented for the degree of

Doctor of Philosophy

Supervisor: Dr. David Cheneler

Engineering Department

Lancaster University

United Kingdom

December 2020

Acknowledgements

Firstly, I would first like to thank my supervisor Dr. David Cheneler for his assistance and support during the PhD process. Without his guidance, encouragement and support the production of this dissertation would not have been possible.

Secondly, I would like to express my gratitude to T.E. Laboratories for their professional and financial support throughout this research. I would also like to particularly thank Patrick Roche and Breda Moore for their technical expertise in relation to the colorimetric sensor which has been invaluable.

Last and not least, I would like to thank my family for their invaluable support and proofreading throughout my research.

Abstract

Clean water is a finite resource, and the quality of such is best monitored by colorimetric in-situ sensors, which allow frequent, non-labour intensive sampling, and are low-cost and simple to manufacture. There are multiple types of sensors that exist in the literature, however, many are cost-prohibitive for wide deployment, or the literature does not not fully elaborate on their operation. The aim of this research was to extend the lifetime and improve the performance of a colorimetric in-situ sensor, Aquamonitrix colorimetric sensor, that was produced by T.E. Laboratories, in addition to characterising sensor behaviour. Its operation was focused on the Griess reaction, in which a vivid azo dye is produced in the presence of nitrite, that can be linearly calibrated to the absorbance by the dye from a photodectector placed at the opposite end of a microfluidic detector channel to a monochromatic light source. Using multiobjective optimisation on a numerical model of a Y-junction micromixer, it was found that both sensitivity could be increased and reagent could be conserved, by limiting the proportion of reagent used during testing to 5% to 7.5% of testing solution, as opposed to the 50% originally used by the system. The conservation of the reagent allowed for an increased sensor deployment lifetime of up to tenfold. To better understand how the parameters of analyte concentration, reagent proportion of test solution, and mean flow velocity of the solution affect sensor output, both mechanistic and data-based modelling of the continuous and stopped flow stages of the sensor were undertaken. Third-order and second-order models were identified for the continuous and stopped flow data respectively. The second-order model is analagous to the two-step Griess reaction, of which there is a first, faster step. Further characterisation of the zeroes, poles and transfer function coefficients of the third order models showed that parameterisation was possible and, using principal component analysis, reduction of parameters. Other testing on the effects of order of cycles, turbidity and heavy metals was also conducted to measure their impact on sensor output. Carryover between sensor cycles was found to be the most interfering factor on sensor output, due to the microfluidic connector components, which was eliminated after eight cycles. Overall, the performance and efficiency of the existing sensor was improved,

and the methodologies in this dissertation can be used for other continuous-flow colorimetric sensors and reactions, or even other microreactor applications, such as in green chemistry.

Contents

List of Figures

List of Tables

Nomenclature

$-\lambda^2, -\mu^2$	constants in separation of variables method
α	position of fluid interface at inlet
Δt_i	pseudotime constant
ΔV	photodetector output voltage uncertainty
Δx	channel width
Δy	channel segment length
$\epsilon(\lambda)$	molar extinction coefficient for wavelength λ
$\frac{\partial}{\partial t}$	partial time derivative
$\frac{D}{Dt}$	material derivative
$\frac{f}{\rho}$	impermeability term
λ	wavelength
λ_n	eigenvalue of Fourier series
$\mathbf{n}$	normal vector
$\mathbf{u}$	velocity vector
$\mathbf{x}$	vector of input parameters for optimisation algorithm
μ	dynamic viscosity

∇ gradient operator

ν kinematic viscosity

ρ mass density

τ_c convection time

τ_d diffusion time

τ_r reaction time

$\vec{u}$ velocity

A absorbance

$A(s), B(s)$ constants of integration

b detector channel length

B_n constant of Fourier series

b_{ijk} Legendre polynomial coefficient

$C(x, s)$ Laplace transform of $c(x, t)$

$c(x, t)$ concentration

c_i concentration of chemical species i

c_{in} concentration of reactant

$C_{xx}(x, s)$ second order spatial derivative of C(x,s)

D diffusion coefficient

$Den(\lambda)$ denominator of transfer function in Fourier series for eigenvalue λ

dz discrete length of subsection of mixing channel

$f(x)$ boundary equation

f_i cost function i

$G(s)$ gain function in frequency domain

$g(t)$ gain function in time domain

i imaginary number

K impermeability

k reaction rate constant

k_A reaction rate constant for reaction A

L characteristic length (also hydraulic diameter)

L_e entrance length for laminar flow regime

n sample size

$Num(\lambda)$ numerator of transfer function in Fourier series for eigenvalue λ

$O(\Delta x^2)$ order of magnitude error (secord order)

P perimeter of channel

p pressure

Pe Péclet number

R molecular source term

R^2 coefficient of determination

R_A source term for reaction A

Re Reynolds number

s complex frequency

Sc Schmidt number

T	convection time
t	time
T_i	time constant of transfer function i
u	scalar velocity in x-axis direction
$U(s)$	Laplace transform of input u(t)
$u(t)$	input of transfer function
u_{in}	proportion of reagent quantity at inlets ($0 \leq u_{in} \leq 1$)
u_{mean}	mean flow velocity after mixture of sample and reagent
V	voltage reading from photodetector
v	scalar velocity in y-axis direction
V_0	voltage reading for blank standard
V_{blank}	photodetector output detector for blank
V_{high}	photodetector output voltage for highest concentration standard used for calibration
W	channel segment width
x	axial position
x_0	x at position far from $x = 0$ where $t = 0$
X_s	segregation ratio
Z	total length of mixing channel

Chapter 1

Literature Review

1.1 Introduction

Clean water is a finite resource. It is important that it is carefully managed. While anthropogenic activity from agriculture and other industries has a negative impact in highly developed countries, the effects are more profound in less developed countries, where increased poverty makes the availability of clean water scarcer, putting public health at risk. Therefore, it is imperative from an ecological and health perspective that the level of pollutants that enter environmental waters do not exceed prescribed levels, not only by those set by the World Health Organisation, but enacted in legislation in the United Kingdom and the European Union by the Water Framework Directive, and in the US through the Clean Water Act [1]. To ensure that the levels of pollutants of interest do not exceed prescribed levels, they need to be continuously monitored. The most established monitoring method is through grab samples, in which the water is manually obtained, then sent for laboratory analysis. This is only representative of the water body at that position and time. The process is also both labour and cost intensive, hence the interest in in-situ systems, which can complete both sampling and analysis in a preferable manner on-site, while transmitting the collected data for remote analysis. Another advantage of in-situ sensors is that they can be placed in relatively remote or otherwise inaccessible areas, meaning that there is increased availability of data at these locations. In order for these systems to be suitable for long-term deployment, it is important that

both the sensors and collected data are robust and reliable. Pollutants of interest include nitrates and phosphates, both of which are indicative of industry and agricultural waste. These can be detected using classical colorimetric assays. In these assays, water, potentially containing a pollutant, is mixed with a reagent in a reactor [2, 3] so that the resulting colour intensity can be used to infer the concentration of the pollutant. Through a large network of in-situ sensors, it would be possible to acquire spatial data regarding the water body being monitored, as opposed to grab sampling limitations outlined above. One such example is that of the sea, where boats have been driven around from which quality indicators such as pH and nutrients have been measured[4]. If there were a large sensor network – which is only feasible using a sensor which is low-cost – from which this data could be collected from, not only would the above be rendered unnecessary, but the paradigm of using sensors to improve overall reliability and redundancy of data could be achieved as that in the field of air pollution monitoring [5], where the cost of sensors is not prohibitive.

1.2 What is microfluidics?

Microfluidics is defined as "the study of flow in artificial microsystems, including miniaturized fluidic devices [6]." The first use of microfluidics was that of gas chromatography in the 1960s [7], although at the time it was regarded as a subset of chemistry. A much more familiar example of microfluidic technology in widespread use since the 1980s is inkjet printing [8]. Interest in such applications has increased since the emergence of microelectronic mechanical systems (MEMs) in the 1980s [9] and following from this microfluidics became a distinct research topic in the 1990s [10]. More recent literature focuses on the application of technologies such as lab-on-a-chip (LOC), which has primarily biomedical applications as point-of-care (POC) devices [11] and organs-on-chip [12, 13, 14]. Kandlikar and Grand [15] proposed different length scales for conventional, mini and microchannels, the latter of which includes channel widths of between $10\,\mu\mathrm{m}$ and $200\,\mu\mathrm{m}$. Due to a higher surface area to volume (SAV) ratio than in conventional scale flow, there is increased contact with the channel walls. This

increases stiction, reducing flow velocity near the walls, and in cases of high levels of contact, can greatly increase back pressure. Convective mixing is difficult to achieve in microchannels, due to the dominance of surface forces of laminar flow. Therefore, mixing is highly dependent on chemical diffusive properties and concentration gradients.

This is expressed by the Reynolds number, where the calculation $Re = Lu_{mean}/\nu$, where L is the characteristic length, defined as $L = 2A/P$, where A is the cross-sectional area, P is the perimeter of the channel, u_{mean} is the mean flow velocity through the channel, and ν is the kinematic viscosity of the fluid in the channel, assuming an aqueous solution, to be $1 \times 10^{-6}\,\mathrm{m^2\,s^{-1}}$. Laminar flow is assumed where $Re \leq 2000$. For example, where L = 200 µm, u_{mean} = $50\,\mathrm{mm\,s^{-1}}$, $Re = 10$, which means a highly laminar flow.

The approach of using low-cost materials, such as polymethylmethacrylate (PMMA) and polydimethylsiloxane (PDMS) has introduced using LOC for wider application. One such example is in the use of environmental monitoring, which is discussed in Section 1.3.1. While the use of microfluidics has shown to be hugely beneficial in the applications above, a major and commonly encountered issue in microfluidics is mixing, which is discussed in Section 1.2.1.

1.2.1 Mixing in microfluidics

As discussed in Section 1.2, microfluidics is characterised as highly diffusive, laminar flows. In straight channels, the degree of mixing, presumed to be completely dominated by diffusion, can be geometrically determined in the steady state. For a microchannel, of length Z, and channel width W, if the confluence of the mixed fluids is at the centre, and u_{mean} is known, one can determine the mixed region as an isosceles triangle, where the centre line Z corresponds to a time constant of $\tau_c = Z/u_{mean}$. The diffusion width can be approximated using the equation $D \approx \Delta x^2/4\tau_c$, where D is the diffusion constant, $\Delta x/2$ is half the mixing width. Rearranging for D provides the definition $\Delta x \approx 2\sqrt{D\tau_c}$. To then determine the mixing length, Δx can be substituted with L, such that $Z = (L^2 u_{mean})/(4D)$. In the case above, with a $200\,\mu\mathrm{m}$ channel width, diffu-

sion coefficient $2 \times 10^{-9}\,\mathrm{m^2\,s^{-1}}$ and mean flow speed $30\,\mathrm{mm\,s^{-1}}$, this means a mixing length of $60\,\mathrm{cm}$, which accounts for 3000 times the channel width. This is indicative of poor mixing, which is denoted by the Peclet number, $Pe = Lu_{mean}/D$, where the larger the number, the poorer diffusive mixing is. A slower flow rate increases mixing time, so the minimal flow rate should be used to achieve maximum diffusive mixing. However, a low-cost implementation of motors used to empty syringes employ peristaltic or brush motors, which have a minimum speed at which they can pump steadily. Therefore, it is imperative to try and increase mixing as much as possible in an otherwise laminar environment.

Active mixing

Active mixing incorporates the use of peripheral components to exert an external force on the fluid. The objective in this type of mixing is to induce turbulence within the system where the scope for passive mixing is limited, increasing cross-sectional flows and thus mingling. There is ample literature describing mixing methodologies [16, 17, 18, 19, 20, 21]. Active methods include using pressure, electrohydrodynamics, electrokinetics, heat and acoustics [18, 22, 23].

The extra components that are incorporated into the system add additional complexity not only to the nature of the system, but also to fabrication, and increases the points of failure that are present. There is also increased energy demand by the peripheral components, negatively impacting the deployment time of an in-situ sensor. Therefore, it is preferable to use passive mixing methods, which encourage secondary flows as a means of mixing, some of which will be discussed in Section 1.2.1.

Passive mixing

Passive mixing exploits channel geometry to induce secondary flows. Methods include lamination of different fluids, enhancing diffusion, chaotic advection and promoting secondary flows. Successful lamination requires a three dimensional structure to fully fold the different layers into each other repeatedly, which is difficult to fabricate at low

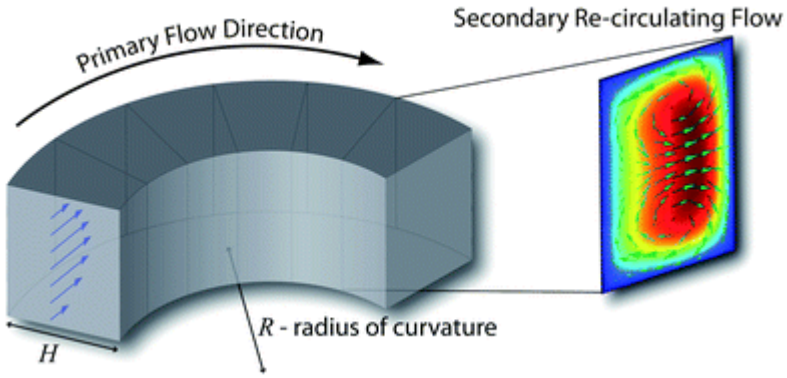

Figure 1.1: Secondary flows in curved channel. Reproduced from [30].

cost. The most simple micromixer is the T-junction micromixer, in which two fluids mix at $90°$. Its simplicity means that there is much research done on understanding how fluids mix at T-junctions, leading to extensive numerical and experimental work [24, 17, 25, 26, 27, 28, 29]. The nature of using a serpentine channel to increase cross-sectional secondary flows (perpendicular to axial flow) is common, and is underpinned by inertial microfluidics, much studied by Di Carlo [30]. The curvature in the channel induces a circular secondary flow due to centrifugal force, which pushes flow towards the inner wall out, and along the channel walls back around to the outer wall, as per Figure 1.1, improving mixing [31].

This can be characterised by the Dean number (De), as per Equation (1.1).

$$De = Re\sqrt{\frac{D}{2R_c}} \tag{1.1}$$

The important parameters are the radius of curvature R_c, diffusion coefficient (D), flow speed as well as the channel width (incorportated into Re). If De is too small ($De < 1$), then there is little to no rotation. If De is too large, then all of the cross section rotates in its entirety, resulting in little mixing. Ideal mixing occurs outside of extreme De values. The study assumes a circular channel, although rectangular shapes feature more prominently in microchannels due to manufacturing processes. There has also been work conducted in using multiobjective optimisation to improve mixing by varying Re [32]. This creates corners where the circulation will not reach due to flow field, acting as dead zones. The use of serpentine channels within a colorimetric in-situ

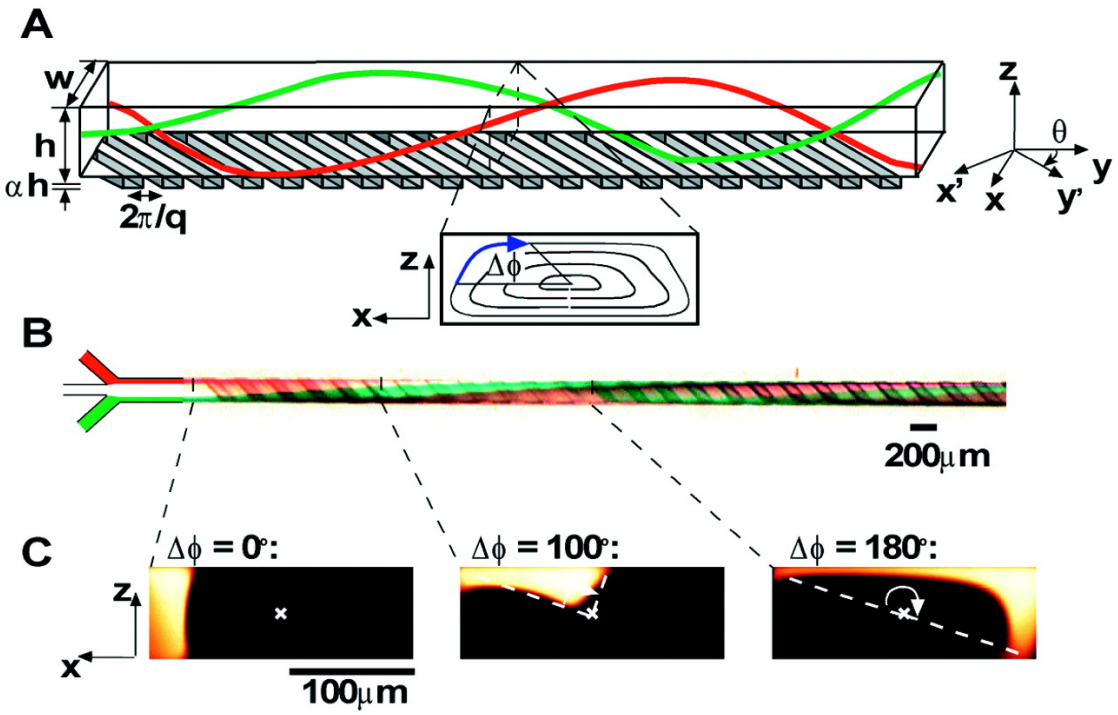

Figure 1.2: Staggered herringbone mixer. Subfigure A shows the flow direction induced in channel width w, height h, of frequency q. The subfigure B provides a top-down view of the mixer. Grooves are etched at an angle to the direction of flow. This establishes turbulence which mingles the fluids together, as seen in subfigure C for phase difference $\Delta\phi$. Reproduced from [35].

increases the quantity of reagent used.

Three-dimensional manufacturing methods are required to fabricate mixers that permit the Baker's transform, in which the layers of each fluid are folded into each other successively. This reduces the width of each fluid layer, meaning that diffusive mixing can occur much more quickly than without lamination, as $D \propto \Delta x^2$. The 3D mixer used was produced using multiple layers of PMMA [33, 34], but this again adds to complexity in manufacturing. The issue with this type of micromixer in a low-cost sensor is its cost, complexity and increased modes for failure during bonding.

One of the most widely cited micromixers is the staggered herringbone mixer by Stroock et al. [35]. The channel consists of etched grooves into the base of the channel which are placed at an angle to the direction of flow, as in Figure 1.2. This creates turbulence, which without the grooves would not occur, inducing mixing. The above mixers are greatly researched and, although have been in the microfluidic domain for quite some time, they appear to rarely be implemented in in-situ sensors which incor-

porate microfluidic sensors. Many environmental sensors – which is discussed in more detail in Section 1.3.1 – implement mostly simple designs, namely Y-junctions and serpentine channels. A reason for this is the generally chemistry-oriented nature of the research, with microfluidics being primarily used to facilitate the use of minute fluid quantities. Another reason may be due to the highly specialised nature of complex microfluidic chip manufacture. Many of the facilities required to produce complex – or even basic – designs require the use of clean room facilities, typically either class 100 or 1000 if the features are not too fine. There is also the requirement to produce prototypes to test for designs. The need for inexpensive manufacturing techniques, such as micromilling restricts microreactor design to simple geometric shapes, commonly comprising T-junctions, Y-junctions and serpentine channels. The primary methods include using a knife cutter to create a channel geometry within a layer of pressure sensitive adhesive encased in layers of laser-cut PMMA [36], and the use of CNC milling in layers of PMMA [37] or glass [38]. The channel widths which result from micromilling are restricted to $100\,\mu\mathrm{m}$. The issue of cost is reflected in the simple designs of CNC-milled PMMA chips [39, 40]. This is a limitation in part of the manufacturing method, as the environment will cause issues in ensuring the channel features are free of contamination. Additionally, the removal of swarf after milling channels becomes more difficult as the channels become smaller. Therefore, for many of the methods listed above, the cost of manufacturing processes precludes highly complex geometries, such as that in Figure 1.2, which generally require micro-lithography and/or plasma/chemical etching techniques to produce.

1.2.2 Reactive flow

An additional challenge to modelling mixing is incorpotating reactive phenonema. In addition to flow characteristics, species transport is also required, by means of a source term for the reaction. While the more general form of the reaction convection diffusion equation accounts for differences in diffusivity for different phases and fluid compressibility, it is common to assume the fluid to be incompressible, particularly in the case of

aqueous solutions and also that the only diffusion coefficients regarded are between that of water and the dilute species [41, 42, 32, 21, 43]. Provided that there are negligible thermal effects due to good heat transfer within a microfluidic structure and that reactions are neither exothermic nor endothermic, then the diffusion constant is assumed to be constant in this regard, as well as the reaction rate. The flow in simple microfluidic flows can be assumed to be two dimensional for the investigation of fluid flow to see if there is a steady flow achieved [44] or the distribution of species within a micromixer [45]. The modelling of reactive flows can be quite insightful when the reaction on the LOC is rate-limited rather than diffusion-limited. Reactions in poorly mixed solutions can lead to a reduced effective reaction rate [42]. One such work in modelling reactive flows was undertaken by Shi et al. [21], in which an iodide-iodate test reaction was modelled inside a Y-junction micromixer. The momentum, energy, species and continuity equations formed the governing equations, and solved for using the finite volume method. All channels were of height $500\,\mu\mathrm{m}$, with the inlet channels of width $400\,\mu\mathrm{m}$ and the mixing channel $800\,\mu\mathrm{m}$. The left inlet introduced iodide, iodate and dihydrogen borate anions, while the right inlet introduced H^+. The parameters in this study were the Reynolds number, inlet mixing angle, inlet flow ratio and $[H^+]$, to investigate their effect on the degree of mixing, measured as a segregation ratio X_s, and reaction. The inlet concentrations were dilute, so the entire solution was assumed aqueous. Increasing he Reynolds number was shown to increase the mingling of flow streams at the initial confluence of the fluids. The initial confluence of fluids in the Y-junction micromixer is important because this is where the mixing fluids initially mingle, and the concentration profile that is initially established at this point is influential in downstream mixing. Flow speeds are important because greater flow speeds increase the potential for turbulence at the inlets before mixing. If this is too great, then axial plugging can occur, and if this is too low then no turbulent effects will result. This is evident in Figures 2 and 3 of [21]. Beyond this initial confluence, there was not much more mingling of the fluids. It was also shown that, using the segregation ratio X_s, the optimum angle for ensuring mixing at the inlet was 120° for the flow speeds $20\,\mathrm{mL\,min^{-1}}$, $30\,\mathrm{mL\,min^{-1}}$ and $40\,\mathrm{mL\,min^{-1}}$.

Overall, this work asserted that most of the mixing to occur at a Y-junction micromixer is at that initial confluence. After this, the mixing becomes a time issue, in that a longer mixing channel provides more time for mixing.

It is also of interest to optimise the performance of the reactor. This is possible through the variation of performing multiple numerical simulations to derive the values of the parameters of interest. However, this process can be very computationally expensive when looking at a wide range of values, or where there are underlying non-linearities or interactive terms which can affect the process. Raza et al. [32] used a surrogate model based on radial based neural networks, which was constructed using samples generated by Latin hypercube sampling. Numerical simulations were run on these samples and the objective functions values obtained to ensure that the parameter space was evenly sampled. A multi-objective genetic algorithm was then run on the surrogate data to solve the objective functions to find the optimum parameter values. The optimum values formed a Pareto front, which represented the trade-off between the multiple objective functions.

Lengthening the mixing channel for a continuous flow microfluidic reactor is not always appropriate, particularly when the fluids that are being introduced are in scarce supply. This increases the fluid that is required to pass through the sytstem, and the reagent quantity to perform the reaction.

1.3 In-situ sensors

In-situ sensors provide a way of collecting data to ensure that large quantities of information on water quality indicators can be analysed. There are examples in the literature of in-situ sensors which have been around for quite some time, including an early colorimetric system by Johnson et al. [46], although the deployment time at this stage of the research was limited to 24 hours. There are several sensor types which are deployed in the field for in-situ monitoring, including those based on colorimetric methods in both continuous flow [47] and droplet-based operation [48]. Electrode-based sensors are also used, which will be briefly discussed in the context of water quality monitoring

Figure 1.3: Algal blooms from the result of a pollution event. The algal blooms are clearly distinguishable from the existing grasses.

in Section 1.3.2.

1.3.1 Environmental monitoring

Environmental monitoring is important, as even small levels of pollutants from anthropogenic activity, primarily nitrates and phosphates, result in adverse changes in the environment. Excess runoff from over-fertilisation in agriculture runs into streams, lakes and rivers. The introduction of excess nutrient levels into environmental water results in algal blooms, which distort the ecological balance of existing flora and fauna. These blooms increase the level of photosynthesis taking place in the local environment. The competition for light with other flora and fauna such as phytoplankton means that many fish asphyxiate in the oxygen-depleted, nutrient rich environment. The light being absorbed by the bloom means that there is less opportunity for photosynthesis, resulting in the stunted flora development. This process is known as eutrophication, the effects of which are depicted in Figure 1.3.

Not only are there environmental implications, but this strains municipal water supplies for human consumption and domestic use. While the analogy of high quality spatial and temporal data is not readily available through current monitoring methods, the quality of the data from expensive sensors and grab samples would be traded for the increased spatial availability provided by low-cost designs [49]. This is true in the case of early warning pollution systems, which are set to flag positive results when prescribed pollution levels have been breached [50].

1.3.2 Sensor technologies

While each sensor has similar principles underpinning their operating basis (the Beer-Lambert law in the linear range to produce a calibration curve) there are variations in how some of these are used. In the more sensitive applications for continuous flow operation, the channel length can range from $20\,\mathrm{mm}$ [51, 52, 53], $25\,\mathrm{mm}$ [54], and even $50\,\mathrm{mm}$ [55]. In the case of a droplet-based system, such as by Nightingale et al. [48], the droplets are formed when the sample and reagent mixture of fluid is suspended in a carrier fluid. The measurements are then required to be taken across the channel width (as opposed to through the length of a channel segment), as the plugs are short in length, and each droplet corresponds to a sampling time. This however reduces the optical path length to the width of the microchannel, inherently reducing sensitivity as per Beer-Lambert's law. While there are reported accuracies in the sub-millimolar range, the inherent nature of the optical path being shorter means there is a trade-off between accuracy and sensitivity. The waste in this system then separates back into the colorimetric complex and carrier fluid. Waste is required to be stored at the correct orientation relative to the system, as the used carrier fluid is recycled by the system. In the case of rough terrain or unexpected handling of the system, this would be a potential source of failure for the system.

While it is reported that there is good accuracy achieved when there is a comparison obtained between the sensor and a spectrometer for a continuous flow system by Rérolle et al. [56], the effect of channel geometries or other components which may

influence the data that is reported from the reading is not a focus of this research. The use of multiple channels has also been implemented which allow for measurement of different sensitivities [39]. The scale of microfluidic channels can vary within each of the systems. For example, the chip used by Donohoe et al. [51] reported the mixing and detector channels to be $1000\,\mu\mathrm{m}$ in width and $500\,\mu\mathrm{m}$ in depth. Below are some other technologies, including their advantages and drawbacks.

Electrode-based sensors Electrode sensors operate by having a cathode and anode in continuous contact with the water matrix. The potential difference between these has a linear relationship with the concentration of the pollutant of interest. Electrode probes are advantageous in their low-cost and high portability. They can be seen in research which involves recording water quality indicator levels at sea. This includes pH [57], nitrite [58, 59] and phosphate [60, 61]. While they are highly portable, the electrode is always in contact with the water matrix, promoting fouling, which greatly degrades the sensor. Additionally, there is significant drift reported over time with regards to these sensors, requiring frequent calibration to maintain their accuracy. Some sensors also work with digestive enzymes which require careful consideration to how they are stored, otherwise they would degrade quickly, which is undesirable for an in-situ deployment.

Droplet-based sensors Droplet-based sensors have also been implemented as a method for performing environmental analysis the colorimetric method. Rather than having a continuous flow in which the sample and reagent flow through the channels, the droplets are suspended within a carrier fluid. This provides some advantage compared to continuous flow in that the colorimetric complex is not in direct contact with the microfluidic wall chambers. Some solutions can stain materials or otherwise have deleterious effects by being in contact with the channel walls. Suspended droplets mitigate such an impact. They also create a discrete time separation between readings that are obtained from this system, therefore permitting good time-series data with a relatively low sampling time. There are some drawbacks though to implementing this method, namely the waste management. The work conducted by Nightingale et al. [62] uses ni-

trate standards, though these are at the minimum used $100\,\mu\mathrm{mol\,L^{-1}}$, corresponding to a concentration of 6.2 ppm. The detection length was the internal diameter of the PTFE tubing, which was $500\,\mu\mathrm{m}$, with an additional absorption length through the PTFE medium of $200\,\mu\mathrm{m}$. In comparison to the continuous flow colorimetric sensor, the higher pollution range can be measured, but at the expense of sensitivity. The management of both the colorimetric complex yielded for the reaction, as well as the carrier fluid, must be maintained in the same container. The sensor produced by Nightingale et al. [48] was managed through gravitational separation, taking advantage of the immiscibility of the fluids, then recycling the waste.

Some issues that arise from droplet microfluidics include crosstalk between droplets through processes such as diffusion of hydrophobic molecules into the carrier fluid, noted in Nightingale et al. [see Figure 4 of 62] which can be mitigated through surfactants. Nightingale et al. [62] noted that crosstalk can occur through gas mediation, though this was attributed to the low pH of the droplets where nitrite was converted to nitric oxide. The formation of nitric oxide is difficult to avoid due to the required low pH to ensure solubility in the colorimetric complex. There is a corrective term to account for crosstalk, taking into account the neighbouring molecules' concentrations. In addition, reduction using heat and vanadium was required to digest the nitrate to nitrite for the reaction.

In-situ calibration

In-situ sensors require calibration to ensure that the system outputs are reliable, robust and accurate. The most important data to collect is the reference point, typically either a sample blank or pure water reading. In addition to the blank test, a high standard is then included to calibrate for the upper limit of the curve. This two-point calibration provides the interpolation region for which measurements can be undertaken. A two-point calibration is limited in using as a basis to construct a calibration curve. In the case of early-warning pollution systems, having a reading as outside prescribed limits is sufficient to flag this a point of concern from a regulatory perspective.

Multi-point calibration is superior, but requires the inclusion of a series of standards, or a stock solution which is diluted on an ad-hoc basis. Secondly, to perform an on-chip dilution (the preparation of standards from a stock solution as required) would still require a standard and either deionised or MilliQ water, as well as the additional fluidic network to facilitate this calibration. These both cause an issue in that the required consumables and apparatus would increase the size of the sensor as a whole, affecting ease of deployment, complexity & cost. The sensor mass would also be increased, reducing portability.

Another issue in the calibration of such systems which is of concern is the lifetime of the standard itself which may cause an issue in calibration. While deionised water will change little on a long-term deployment, the inclusion of standards such as nitrite is a challenge as it easily oxidises. In some studies of in-situ sensors, there have also been studies of reagent and standard lifetimes. It was found that in ideal storage conditions for vanadomolybdophosphoric acid for phosphate detection was over one year [63]. In the concentration range that would be included in regulation, there are cases where the standard is expected to be made fresh for testing, which would be the case for nitrite. Even with a high concentration standard, if the dilution approach to creating the multi-standard calibration were taken, there would still be a shelf-life on the scale of months. This is contrary to the deploy-and-forget paradigm which is the aim of such sensors. Another issue with the inclusion of a wide range of standards are the optical properties of the detector channel itself. The channel has a specified length from which light can be absorbed. If the concentration is no longer dilute, then light is not absorbed the same way due to additional intermolecular reaction, and the linear relationship between absorbance and concentration breaks down.

There has been some work done to account for the corrections that need to be made for successful detection. One such quantity that should be minimised as much as possible is stray light. The light detected by the sensor in a scenario of full saturation cannot be coming from the sample as the light is being fully absorbed, and therefore must be coming from the light source itself. Although it is generally minimised and sometimes

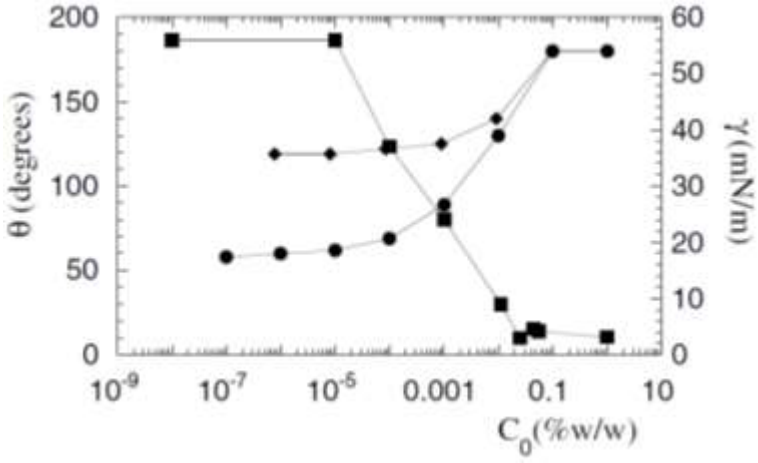

Figure 1.4: The variation of surface tension (squares) and contact angle for glass (circles) and silicon (triangles) for a water droplet with different concentrations of surfactants. Reproduced from [64].

accounted for, the effect of stray light can be reduced.

Segmented flow

Segmented flow has also been used as another method to implement an in-situ sensor. Multiphase flow typically comprises of two or more fluid flows of differing chemical and physical properties, primarily large differences in mass densities (relative magnitude difference of 1×10^3) and immiscibility due to chemical properties. Each phase is distinguishable by a separating boundary or interface. The wettability of each fluid with the channel walls is highly important in describing their behaviour, unlike conventional multiphase flow [64]. Figure 1.4 shows how the presence of surfactants in the liquid can greatly increase wettability of silicon and glass with water, with most variation occurring in less than 0.1% w/w concentration.

Dreyfus et al. [64] characterised the formation of water-oil flow patterns at a cross junction. The two inlets were perpendicular to the outlet contained the oil, and the single inlet parallel contained water. For high flow rates of both fluids, layers of oil formed a lubrication layer at the channel walls, and the water flowed in between these layers. Varying patterns occur for different flow rate combinations, which are characterised in Figure 1.5. The upper-right shows the usual scenario of laminar flow in microchannels, being of interest in biological and chemical applications, where the mixing of multiple

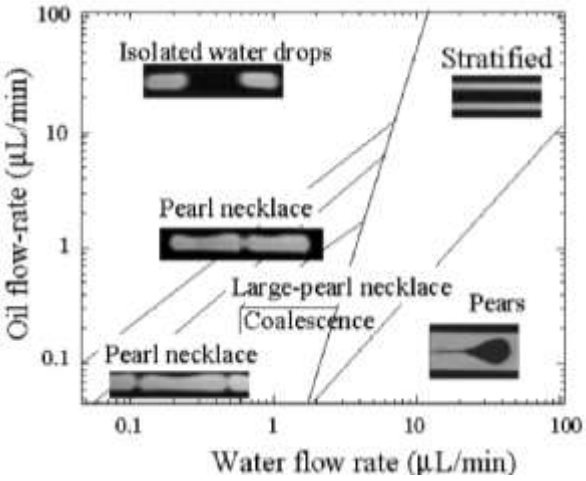

Figure 1.5: The flow pattern for oil and water after mixing at a cross junction. This is plotted against the flow rates for each liquid. Reproduced from [64].

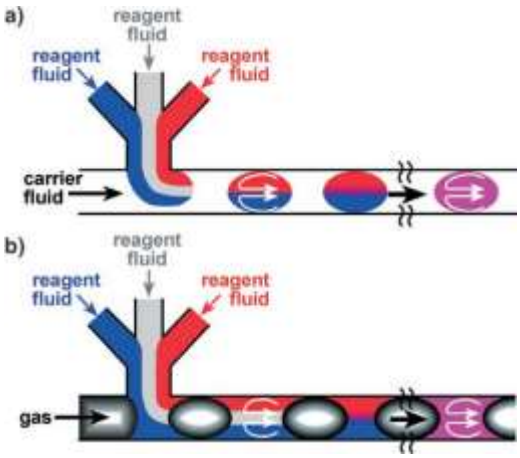

Figure 1.6: Segmented flow within a microchannel. The reagent mixture forms either a bubble in an emulsion (a) or slug in a gas bubble flow (b). The reagents can mix by internal convection currents after segmentation. Reproduced from [65].

reagents is required to be completed quickly. Gas, or another carrier phase (oil), can be used to create a segmented flow. The reagent mixture will either form bubbles within the carrier phase, or act as the slugs between gas bubbles as in Figure 1.6. Segmentation allows for internal convection of the reagent mixture which greatly reduces mixing time [66, 65]. While internal convection combats the slow rate of diffusion, carrier phases can also be used to speed up diffusion by acting as a buffer to narrow the mixing stream. This is implemented using a Y-junction with an additional inlet continuous with the outlet. As the diffusion time (τ_d) is proportional to the characteristic length L ($\tau_d \propto L^2$), this results in greatly reduced diffusion times.

1.3.3 Issues with in-situ sensors

The T-junction mixer (or any similar right angled channel section) will contain some ”dead” flow space where there is little species transport. In the case of subsequent runs, there would be a hysteresis effect, where a large difference in concentration between flow areas and dead zones between runs would be important to measure, as would be the case in high latitude marine readings [67]. Another factor which is seldom mentioned are the peripheral components. Occasionally, the peripheral apparatus which is essential to obtaining, filtering and injecting the water sample into the flow cell is omitted, as well as intermediate microfluidic components such as tubing and interconnectors, which hinders full scrutiny of the sensor.

Implementing a low-cost solution

It has been highlighted in reviews of environmental sensors that the current complexity required in a sensor for reliability makes it difficult to achieve a low-cost solution. There are examples of fabrication processes highlighted in Figure 1.7. The red lines show fabrication processes suited to thermoplastics such as PMMA. These are currently the most promising methods for producing large quantities via batch production. PDMS-based chips are not suited to micromilling as can be seen from Figure 1.7. The bonding process for PMMA chips is needed to enclose the channel. Direct bonding in this case

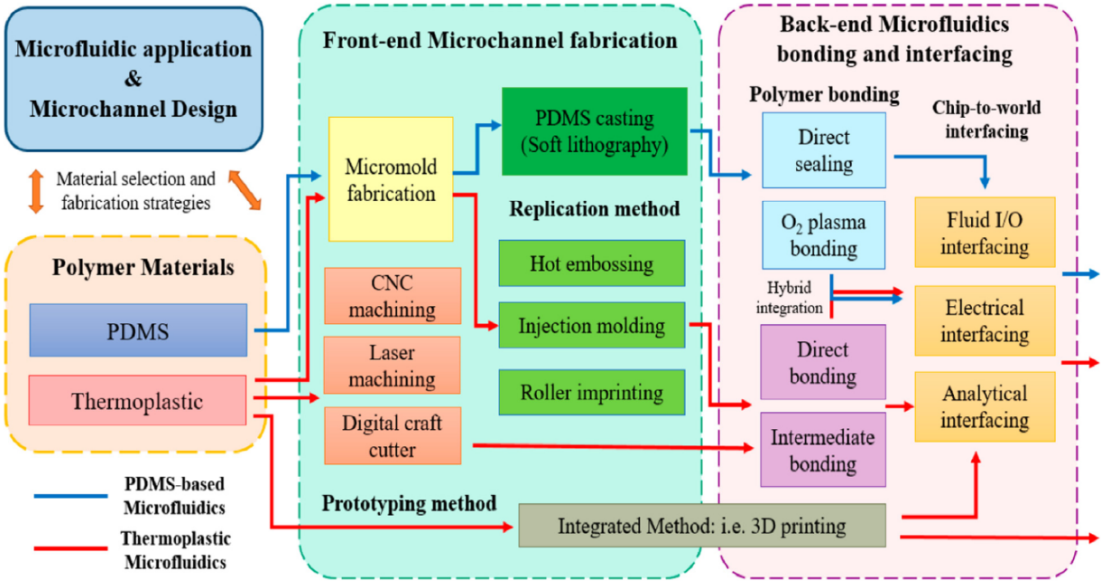

Figure 1.7: Fabrication processes required in creating different types of microfluidic chips. Image reproduced from [68].

typically arises from an organic solvent, such as chloroform vapour. While the use of lab-on-a-chip (LOC) has been exploited successfully in wearable technologies [69] and point of care applications [49], there are still challenges in achieving this in environmental monitoring. Examples of low-cost solutions to the sensor include the use of low-cost pumps incorporated into a microfluidic system, micromilled PMMA chips, and the use of LEDs as monochromatic light sources [51, 55]. Taylor et al. [55] designed a low-cost-sensor where the cost of part totalled US$3,000. A $600\,\mathrm{nm}$ LED was used to detect orthophosphate and total phosphorus, where the colorimetric test used was the molybdenum blue and stannous chloride reagents. While it is important that the sensor is frequently calibrated, the use of over frequent calibration can result in high use of reagent. Additionally, the reagent only has a limited lifespan, which in the case of the molybdovanadophosphoric colorimetric test for phosphate had a lifespan of 12 months. A low-cost colorimetric pH sensor has also been developed, with a range of 7.5 to 8.2 for seawater pH measurements [70]. The microfluidic chip which incorporates the mixing channels and housing had a reported cost of €100. PDMS was the material chosen to make the chip. This was to allow for fabrication outside of clean room setting, although this is reported as a method used for prototyping. In the case of seawater pH readings, it is also important to record the temperature when the sampling is occurring,

as these can effect the output voltage. Three optical cells were used, each consisting of wavelengths of $440\,\mathrm{nm}$, $575\,\mathrm{nm}$ and $730\,\mathrm{nm}$.

1.4 Time-series data

The in-situ nature of the sensor permits time-series data analysis. Data is collected regularly over the deployment time, used to indicate pollution levels. One thing this is omitted from much of the literature however is the data collected during runs. The data that is used to calculate the pollution level is done at a set time during the sensor cycle, as determined by the analytical method used. In the sensor developed by Cogan et al. [2], the flow was stopped for 20 minutes – to allow for full colour development – before a measurement was taken. Omitted from discussion was if there were noise generated from the sensor. White noise of zero mean and unit variance can be averaged out, resulting in a smoothed data curve. However, colorimetric methods are prone to interference a multitude of potential sources. In the case of interfering reactions, standing the solution for a long period of time can result in a false positive being produced. As the light source is monochromatic and other data sources are limited, this poses an issue in distinguishing between true positive readings and interference, which may be more sensitive to a different wavelength. For example, silver, resulting from leaching from consumer electronics, can interfere with the Griess reaction [71], while for extended reacting periods silicate can interfere with the detection of phosphate [72]. The presence of copper can also interfere with the detection of ammonia using the Berthelot method. These include varying temperature, the rate of decay of standards and the potential of interferents in the reaction, although this is well known. One effect that is omitted in many of the stopped flow reactions is the potential for plugging in the flow. This creates difficulty in mixing as the separation is in the direction of flow. To combat this, Cogan et al. [2] stopped the flow for 20 minutes to permit full colour development. While this indeed allows for full colour development, it also avoids many of the issues encountered in higher frequency sampling and analysis by allowing ample time for diffusive mixing. Although 20 minutes is sufficient time for diffusive mixing of sampling and reagent,

the sampling frequency is greatly reduced, after calibration using standards is also performed, which is acknowledged by the author. Calibration which is conducted in-situ, measuring a blank voltage reading V_{blank}, a high standard value and then taking the next value results in the measurement being taken. This calibration, although done very frequently will result in a drift effect over time in part due to degradation of the reagent. This drift occurs in two parts, in that the blank and high standard calibration readings converge over time. Accounting for this degradation will also inherently result in reduced sensitivity in the instrument. If this were to be considered, then the associated uncertainty in the readings will increase to a point where the sensor measurement will effectively only act as a positive or negative result. In a study by Fanelli [73], scientists were surveyed in regard to their admission to or knowledge of misconduct. A pooled average of 1.97% of respondents admitted to falsifying or modifying data, while one third of respondents admitted to dubious practices. This is not to say that the data in much of the literature is improper in any way, but the lack of data and the novelty of the fabrication methods makes replication of many studies quite difficult to achieve. This concern is also expressed by Sastri et al. [67], where in a marine context, the black-box nature of the sensors being produced are concerning. In trying to mitigate sources of error, it is important only to have a sensor which is performing well, but to have known errors that are associated with the sensor. The operation of the sensor should be underpinned by a mathematical model, to support how far from theory the true experimental data collected is from that theorised. In Donohoe et al. [51], the analytical performance of the colorimetric sensor using the vanadomolybdophosphoric method for the detection of orthophosphate, the methods used were the premixing of standard and concentration off-chip, and mixing on-chip. The system is described as autonomous where, according to the work, the process is mostly automated and there is no collection of data outside of the photodiode to make decisions based on operation. Neither is there a basis described to account for noise or perturbations which were experienced in the data collection from a colorimetric basis. It is noted that there are issues regarding reliability and complexity in the sensor, and there was weekly maintenance required, as well as less frequent

substantial maintenance described as being performed to address performance issues.

There is a similar autonomous claim by Cogan et al. [3] for a colorimetric nitrite sensor, but again the analytical procedure described is a routine which does not incorporate decision making. The calibration curves obtained for this method show error bars, but the sample size $n = 3$ was used to generate these. The coefficient of determination was found to be $R^2 = 0.9901$, however the concentration of the standards were not of a linear distribution. The samples are more clustered nearer the low concentration range, and the upper range is more spaced out. In the repeatability study, there were alternating plugs of blank and high standards measured in the channel seven times. It was not expressed in the time series data at which stage the measurements were taken, as the data do not reflect the reaction kinetics that are shown in Figure 6. However, the system is claimed to have component costs of €600, which is far lower than referenced nitrate analysers, their costs varying from €15,000 to €70,000.

1.5 Sensor characterisation

Throughout the literature, there are articles which outlay the construction of a device, and the data collected which are then used to determine concentrations of various pollutants of interest. The issue in many of these papers is the lack of characterisation of the sensors, which would help to indicate their rationale or operation. As many are being developed for commercial use, detailed information is proprietary and not readily available. This has been discussed by Sastri et al. [67] in a perspective paper, although the focus is on oceanic pH sensors. This makes it difficult to scrutinise the operation of the sensor itself. It would also be interesting to discuss the reasons for much of the needed on-board calibration. If it was understood how sensors degrade or change for different environmental factors, then the measurements should be able to be adjusted to provide a corrective factor for the collected data. Additionally, when the workings of the sensor are well understood, then this provides a basis for optimising performance. This is unusual as while this information is not discussed much in the field of sensors regarding water pollution, it is not at all unusual for air quality, in which numerous methods

are used to improve the function of low-cost sensors. The quantity of air quality monitors available at low-cost – for under £50 – can be found from numerous suppliers like Farnell, RS Electronics and models such as Adafruit. Their low cost permits multiple sensors to be deployed in close promixity to one another, providing additional spatial data. In work conducted by Chatzidiakou et al. [5], a low-cost air quality monitor was characterised, comparing its performance between indoor and outdoor environments.

Although the work in sensor characterisation is not vast, there are plenty of other areas in which characterisation has been performed. One such process is in tracer detection in rivers and other fluvial systems.If the downstream flow of the tracer is understood, then the effects of harmful pollutants entering a water stream can be detected, their residence time in the water and more. Data-based mechanistic (DBM) modelling [74, 75, 76] has been employed in this respect to try and predict the concentration of a pollutant downstream from a river source.

1.6 Thesis structure

The purpose of this research is to characterise the performance of a colorimetric microfluidic sensor, in order to improve the deployment time of the sensor, increase sensitivity and minimise use of onboard solutions. This is achieved through design optimisation rather than incorporating additional components, keeping costs low, which is essential in the proliferation of large numbers of such sensors. Chapter 2 examines a means for producing an analytical model for the flow within the system, within a steady state basis. This includes a purely diffusive model, a convection-diffusion model, and the inclusion of reactive components. Chapter 3 examines the current sensor operation. This includes the constituent components, the theoretical principle behind the colorimetric method as a means for concentration measurement, and the data currently collected. Chapter 4 looks at a Y-junction microreactor which will examine the continuous flow reaction of two products – an inlet containing a reagent (the Griess reagent for nitrite detection) – as well as a channel for a varying concentration. Finite difference methods simulations are used to evaluate the flow characteristics and species transport. The

parameters that were varied included the sample to reagent flow rate ratio, the concentration of the reactant, and the mean flow rate in the sensor. A numerical study of this is discussed, including the governing equations which establish the flow within the channel – namely the Navier-Stokes equation and the Poisson pressure equation – and the species transport and reactive components – namely the reacting convection-diffusion equation. This then provides for the basis for a surrogate model using Latin hypercube sampling of samples covering the wide range of parameter values. A non-dominated genetic sorting algorithm (NSGA-II) is then be used to identify the maximum yield and the minimal waste for the given reactor. Information extracted from this then provides insight into how parameter adjustment can extend instrument lifetime and improve instrument sensitivity. Chapter 5 outlines the methods used in the preparation of reagents and standards, as well as demonstrating the effects of interferents of the reactions and turbidity on sensor output. Chapter 6 then focuses on trying to characterise the response of the experimental sensor through model order reduction, as the governing equations are shown to be highly nonlinear in nature. The model produced, discussed in Chapter 7, forms the basis of a calibration method which will try to mitigate the effects of noise, mitigate deleterious effects resulting from contaminants, namely from the use of historical data and data collected from different parts of the cycle. Concluding remarks and future work are discussed in Chapter 8.

Chapter 2

Analytical modelling approach

The aim of this section is to demonstate that the reacting convection-diffusion flow problem is deterministic in nature, and to extract a usuable model for later chapters. Firstly, a derivation of a purely 1D convective flow is obtained, then separately a diffusive flow across a channel cross section, after which the reaction term is incorporated into the 1D convection problem. Secondly, a Laplace transform of the 1D convection-diffusion equation is performed. Thirdly, the diffusion problem is extended to two dimensions, including the channel width and downstream position. Lastly, the reaction term is incorporated into a 2D convection-diffusion model using separation of variables.

2.1 Introduction

As mentioned in Chapter 1, the flow in microchannels is characterised by a low Reynolds number, due to viscous flow. This means that the flow is laminar in nature, making the flow pattern trivial to model in the absence of significant turbulence which limits mixing. This can be modelled using the equations in Chapter 3. In addition to reaction kinetics, the colorimetric sensor can be assumed, in its most simple representation, as a 2D geometry in which the sample and reagent coalesce at a Y-junction. Between the junction and detector channel, the solution will mix and react, depending on multiple factors such as mixing, reaction rate, mean flow velocity, mass diffusion coefficients and characteristic channel width. The detector channel however is only capable of produ-

cing a single output per data point, that being the voltage reading of the photodetector. In the absence of environmental incident light, the light passing through the sample is absorbed by the colorimetric complex (CC), the degree of which is correlated to the concentration of the analyte in the environmental sample. If the aforementioned parameters are known, which in the case of the sensor is predetermined by the operating parameters and channel geometry, and for the reaction, these are known beforehand as colorimetric reactions are well established methods, such as the Griess reaction. In theory, it should be trivial to produce an analytical model which can reasonably predict the output recorded by the detector channel. The model input is the unknown concentration of the sample, and the ratio of sample to reagent that is introduced at the Y-junction. The model output is the absorbance reading from the photodetector at the detector channel. The other parameters form part of the model and adjust the ultimate absorbance reading e.g. increasing the flow speed will reduce the reaction time, a smaller diffusion coefficient will reduce mixing etc.

This ultimately couples the reaction kinetics to the fluid mechanics for determining yield. However, there is some complexity in coupling the reaction kinetics with the species transport that occurs before the detector channel, as this is influenced not only directly by the concentrations of analyte, CC and intermediary reactions, but also mixing that occurs in the channel.

Firstly, some inert transport models are examined, namely diffusion-only and convection-only flows. These produce a time-delay step function for the convection, and a residual model for the diffusion-only problem. Secondly, convection and diffusion are modelled together and combined using the Laplace transform. After showing that the inverse Laplace transform model is not feasible, separation of variables is used to obtain analytical models. Thirdly, a 2D model of the problem is brought together, with cross-sectional diffusion and axial convection. Lastly, reaction kinetics are included to the 2D problem.

2.2 Convection and diffusion modelling

2.2.1 Inert 1D axial convection model

A simple TF can be formed using the Laplace transform for the convection only problem. For a one-dimensional convection-only problem, let us assume:

$$\frac{\partial c}{\partial t}(x,t) = -u_{mean}\frac{\partial c}{\partial x}(x,t) \tag{2.1}$$

where the subscript denotes differentiation with respect to that variable. Performing the Laplace transform (assuming zero initial conditions):

$$sC(x,s) = -u_{mean}\frac{\partial C}{\partial x}(x,s) \tag{2.2}$$

Expressing as a function of $C(x,s)$:

$$\frac{\frac{\partial C}{\partial x}(x,s)}{C(x,s)} = -\frac{s}{u_{mean}} \tag{2.3}$$

When both sides are integrated with respect to x this results in the general solution of the form:

$$C(x,s) = A(s)\exp\left(-\frac{s}{u_{mean}}x\right) \tag{2.4}$$

$A(s)$ can be determined through the inclusion of boundary conditions. When $x = 0$ is assumed to be the the location of the input i.e. the source of the species $A(s) = u(s)$, where $C(0,s) = u(s)$ therefore:

$$C(x,s) = u(s)\exp\left(-\frac{s}{u_{mean}}x\right) \tag{2.5}$$

If the output at the end of the channel length of interest, x_0, then $Y(s) = C(x_0,s)$. The TF gain $G(s)$ can then be simple expressed as:

$$G(s) = \frac{C(x_0,s)}{C(x,s)} = \exp\left(-\frac{x_0}{u_{mean}}s\right) \tag{2.6}$$

This model results in a time delay of x_0/u_{mean}, which corresponds to the residence time within the channel. The inverse Laplace transform of this problem then becomes:

$$g(t) = u\left(t - \frac{x_0}{u_{mean}}\right) \tag{2.7}$$

This is a simple time delay model, and does not account for the different positions along the channel cross section due to the parabolic velocity distribution. In this case, the shortest convection time is at the channel centre and increases towards the channel walls.

2.2.2 Inert cross-sectional diffusion

A diffusion only process in a one-dimensional chamber can also be modelled using the Laplace transform, following on from the example in [77], where the Laplace transform of the diffusion equation is obtained. This results in an infinite number of zeros and poles which are then expressed as a finite sum of the first N first order transfer functions. If we have the Laplace transform of the diffusion process in a channel of width L, and fixed input such that:

$$\frac{\partial^2 C}{\partial x^2}(x,s) - \frac{s}{D}C(x,s) = 0 \tag{2.8}$$

Solving as an ODE:

$$C(x,s) = A(s)\sinh\left(\sqrt{\frac{s}{D}}x\right) + B(s)\cosh\left(\sqrt{\frac{s}{D}}x\right) \tag{2.9}$$

Returns the form:

$$C(x,s) = \frac{\sinh\left(\sqrt{\frac{s}{D}}x\right)}{\sinh\left(\sqrt{\frac{s}{D}}L\right)}U(s) \tag{2.10}$$

Where $C(L,s) = 0$, $C(0,s) = U(s)$. The sinusoidal denominator suggests that there is an infinite number of poles, and likewise infinite zeros of the equation. It is possible to express such a function as a summation of first order TFs. Schor [77] expanded

Equation (2.10) using the residual method, such that for each pole, the transfer function could be expressed as:

$$G(s) = \sum_{n=0}^{\infty} \frac{res(\lambda_n)}{s - \lambda_n} \tag{2.11}$$

where each residual is found using the expression:

$$res(G, \lambda) = \lim_{s \to \lambda} (s - \lambda) G(s) = \frac{Num(\lambda)}{Den'(\lambda)} \tag{2.12}$$

Where $Num(\lambda)$ is the numerator of each TF, $Den'(\lambda)$ is the derivative of denominator $Den(\lambda)$ and λ_n is the associated pole. If we take the microfluidic example of a channel width with zero flux walls $\frac{\partial C}{\partial x}(0, s) = \frac{\partial C}{\partial x}(L, s) = 0$, then we can solve for Equation (2.9).

$$\frac{\partial C}{\partial x}(x, s) = A(s)\sqrt{\frac{s}{D}} \cosh\left(\sqrt{\frac{s}{D}} x\right) + B(s)\sqrt{\frac{s}{D}} \sinh\left(\sqrt{\frac{s}{D}} x\right)$$

For the nontrivial solution, $A(s) = 0$, meaning that for $\sinh x = i \sin x$:

$$\sinh\left(\sqrt{\frac{s}{D}}\right) L = i \sin\left(\frac{L}{i}\sqrt{\frac{s}{D}}\right) = 0$$

$$\frac{L}{i}\sqrt{\frac{s}{D}} = n\pi$$

$$s = -D\left(\frac{n\pi}{L}\right)^2$$

If we assume an input at the centre of the channel $C(L/2, s) = U(s)$, then:

$$B(s) = \frac{U(s)}{\cosh\left(\frac{L}{2}\sqrt{\frac{s}{D}}\right)}$$

meaning

$$C(x, s) = \frac{\cosh\left(x\sqrt{\frac{s}{D}}\right)}{\cosh\left(\frac{L}{2}\sqrt{\frac{s}{D}}\right)} U(s)$$

If the desired output of this system is $Y(s) = C(x_0, s)$ then

$$G(s) = \frac{\cosh\left(x_0\sqrt{\frac{s}{D}}\right)}{\cosh\left(\frac{L}{2}\sqrt{\frac{s}{D}}\right)}$$

If the residuals are then generated using the same approach as above, we get

$$res(\lambda) = \frac{4\pi nD\cos\left(\frac{n\pi}{L}x\right)}{\sin\left(\frac{n\pi}{2}\right)} \tag{2.13}$$

The final form of the transfer function of this problem is:

$$G(x,s) = \sum_{n=1}^{\infty} \frac{4\pi nDL^2\cos\left(\frac{n\pi}{L}x\right)}{\sin\left(\frac{n\pi}{2}\right)\left(L^2 s + D(n\pi)^2\right)} = 4\pi DL^2 \sum_{n=1}^{\infty} \frac{n\cos\left(\frac{n\pi}{L}x\right)}{\sin\left(\frac{n\pi}{2}\right)\left(L^2 s + D(n\pi)^2\right)} \tag{2.14}$$

There is an issue posed with the $\sin(n\pi/2)$ term in the denominator. For $n = 2, 4, ...$, $G(x, s)$ is undefined. This can be solved using l'Hôpital's rule to get:

$$4\pi DL^2 \sum_{n=1}^{\infty} \frac{\cos\left(\frac{n\pi}{L}x\right) - \frac{\pi Lx}{L}\sin\left(\frac{n\pi}{L}x\right)}{\frac{\pi}{2}\cos\left(\frac{n\pi}{2}\right)\left(L^2 s + D(n\pi)^2\right)} \tag{2.15}$$

2.2.3 Inclusion of reaction term

To include the reaction term, this can be displayed more clearly using a state space representation. Using the previous approach, including both c_1 and c_2 in the same expression and performing the Laplace transform, is not practical as, due to the spatial derivative, it is not possible to define either C_1 or C_2 independently of each other. For clarity, $c_1 = c_{reactant}, c_2 = c_{product}$. To include all terms, the spatial derivative is roughly discretised using the boundary conditions $c_1(0, t) = u(t)$ and $c_2(0, t) = 0$ so that:

$$\frac{\partial c_1}{\partial x} = \frac{c_1(x_0, t) - u(t)}{x_0} \tag{2.16}$$

$$\frac{\partial c_2}{\partial x} = \frac{c_2(x_0, t) - 0}{x_0} \tag{2.17}$$

This can be expressed in state space representation:

$$\begin{bmatrix} \frac{\partial c_1}{\partial t} \\ \frac{\partial c_2}{\partial t} \end{bmatrix} = \begin{bmatrix} -\frac{u_{mean}}{x_0} - k & 0 \\ k & \frac{u_{mean}}{x_0} \end{bmatrix} \begin{bmatrix} c_1 \\ c_2 \end{bmatrix} + \begin{bmatrix} \frac{u_{mean}}{x_0} \\ 0 \end{bmatrix} u(t) \tag{2.18}$$

$$y = \begin{bmatrix} 0 & 1 \end{bmatrix} \begin{bmatrix} c_1 \\ c_2 \end{bmatrix} \tag{2.19}$$

This is only assuming two points in space. To make this more accurate, the system can be broken up into smaller components, such that there is a chain of TFs with n nodes and $n-1$ spacings. This is discussed in more detail in Chapter 6.

2.2.4 Transfer-function ready approach using Laplace transform

To initially get a controllable transfer function for the outlined problem, the Laplace transform was performed on the reacting convection-diffusion problem. To simplify the problem initially, the reacting component was put in, giving us:

$$\frac{\partial c}{\partial t}(x,t) = D\frac{\partial^2 c}{\partial x^2}(x,t) - u_{mean}\frac{\partial c}{\partial x}(x,t) \tag{2.20}$$

The with the Laplace transform this becomes:

$$sC(x,s) = D\frac{\partial^2 C}{\partial x^2}(x,s) - u_{mean}\frac{\partial C}{\partial x}(s,t) \tag{2.21}$$

If this is rearranged as a second order ODE this becomes:

$$D\frac{\partial^2 C}{\partial x^2}(x,s) - u_{mean}\frac{\partial C}{\partial x}(x,s) - sC(x,s) = 0 \tag{2.22}$$

Rearranging:

$$\frac{\partial^2 C}{\partial x^2}(x,s) - \frac{u_{mean}}{D}\frac{\partial C}{\partial x}(x,s) - \frac{s}{D}C(x,s) = 0 \tag{2.23}$$

Solving for this with respect to x, the following root is achieved:

$$\lambda = \frac{u_{mean}}{2D} \pm \frac{\sqrt{(u_{mean}/D)^2 - 4s/D}}{2} \tag{2.24}$$

This is rearranged to:

$$\lambda = \frac{u_{mean}}{2D} \pm \frac{\sqrt{u_{mean}^2 - 4Ds}}{2D} \tag{2.25}$$

The root is composed of a constant term α and the surd component β, so the term takes the form $\alpha \pm \beta$, then the equation becomes:

$$C(x,s) = A(s)\sin\left((\mu - \beta)x\right) + B(s)\cos\left((\mu + \beta)x\right) \tag{2.26}$$

As a first initial condition, $c(0,t) = u(t)$. In the Laplace domain, this becomes $C(0,s) = u(s)$

$$C(0,s) = u(s) = B(s) \tag{2.27}$$

If this is substituted into Equation (2.26) then:

$$C(x,s) = A(s)\sin\left((\mu - \beta)x\right) + u(s)\cos\left((\mu + \beta)x\right) \tag{2.28}$$

Steady state

If Equation (2.28) is assumed to be in the steady state ($s = 0$), then using Equation (2.25) the roots become $\lambda = 0, u_{mean}/D$. Then the problem can be reduced to:

$$C(x,0) = A(0)\sin\left(\frac{u_{mean}}{D}x\right) \tag{2.29}$$

It was found that due to the location of the Laplace operator within the square root of the sine and cosine terms, it was nontrivial and difficult to extract a meaningful transfer function from this without additional boundary conditions. Additionally, in most cases $u_{mean} \gg D$, so there is suspected numerical instability that would result from this if an obtainable TF were realised.

2.3 Time-domain approach

This has been extensively studied by Sahu et al. [78], where the work completed was for a 1:1 fluid mixture, in which the mixing is performed primarily diffusively. Below are some simplifications and some additions that build up on this work, including some convection only problems, the simplification to 2D, and the inclusion of a time component. The RCD equation can be attempted to be solved by using the separation of variables approach. This allows for each segment of the equation to be solved as separate ODEs, which are recombined. For a purely diffusive problem:

$$\frac{\partial c}{\partial t} = D\frac{\partial^2 c}{\partial x^2} \tag{2.30}$$

Using the separation of variables method $c(x,t) = X(x)T(t)$:

$$\frac{dT}{dt}\frac{1}{T} = D\frac{d^2X}{dx^2}\frac{1}{X} = \lambda \tag{2.31}$$

Where λ is a constant pertinent to both equations. Solving for time:

$$T(t) = T_0 \exp(\lambda t) \tag{2.32}$$

It does not make sense for the solution of $T(t)$ to grow exponentially with time. Therefore, $\lambda < 0$, or $\lambda \equiv -\lambda^2$. Solving for the spatial term:

$$X(x) = Asin\left(\frac{\lambda}{\sqrt{D}}x\right) + Bcos\left(\frac{\lambda}{\sqrt{D}}x\right) \tag{2.33}$$

Using the boundary conditions $\frac{dX}{dx}(0) = \frac{dX}{dx}(L) = 0$, then $A = 0$. Additionally:

$$0 = -\frac{\lambda}{\sqrt{D}}Bsin\left(\frac{\lambda}{\sqrt{D}}x\right) \tag{2.34}$$

To avoid the trivial answer of $B = 0$:

$$\lambda_n = \frac{(2n-1)\pi\sqrt{D}}{2L}, n = 1, 2... \tag{2.35}$$

This reduces the original problem, including all constant terms into B_n, to:

$$c(x,t) = B_n exp\left(-D\frac{(2n-1)^2\pi^2}{(2L)^2}t\right) cos\left(\frac{(2n-1)\pi}{2L}x\right) \tag{2.36}$$

2.3.1 Diffusion only – Fourier series

For the diffusion only problem, where the subscript denotes the differentiation with respect to that variable:

$$\frac{\partial c}{\partial t} = D\frac{\partial^2 c}{\partial x^2} \tag{2.37}$$

If this is made dimensionless using the mean velocity $t = L/u_{mean}$ and length scale L:

$$Pe\,\frac{\partial c}{\partial t} = D\frac{\partial^2 c}{\partial x^2} \tag{2.38}$$

Splitting the variable such that $c(x,t) = X(x)T(t)$:

$$Pe\frac{dT}{dt}\frac{1}{T} = \frac{d^2X}{dx^2}\frac{1}{X} = -\lambda^2 \tag{2.39}$$

Then solving for T:

$$T(t) = A\exp\left(\frac{-\lambda^2}{Pe}t\right) \tag{2.40}$$

Using the boundary condition $T(0) = T_0$

$$T(t) = T_0\exp\left(\frac{-\lambda^2}{Pe}t\right) \tag{2.41}$$

Solving for X gives a second order ODE:

$$\frac{d^2X}{dx^2} + \lambda^2 X = 0 \tag{2.42}$$

Solving for the roots gives:

$$m = \sqrt{-\lambda^2} = i\lambda \tag{2.43}$$

Hence the equation becomes:

$$X(x) = B\cos(\lambda x) + C\sin(\lambda x) \tag{2.44}$$

Using the boundary condition $\frac{dX}{dx}(0) = \frac{dX}{dx}(1) = 0$, $B = 0$:

$$\frac{dX}{dx}(1) = 0 = -\lambda C\sin(\lambda) \tag{2.45}$$

Taking $\lambda, C \neq 0$, then:

$$\lambda_n = n\pi \tag{2.46}$$

To recombine the separation as a Fourier series:

$$c(x,t) = \sum_{n=0} C_n \cos(n\pi x) \exp\left(-\frac{n^2\pi^2}{Pe}t\right) \tag{2.47}$$

To solve for C_n, the initial conditions $c(0 \leq x \leq 0.5) = 1$ and $c(0.5 < x \leq L) = 0$.

For the C_0 term:

$$C_0 = \int_0^1 f(x)dx = \frac{1}{2}$$

And C_n:

$$C_n = 2\int_0^1 f(x)\cos(n\pi x)\,dx \tag{2.48}$$

$$C_n = 2\int_0^{1/2} 1\cos(n\pi x)\,dx + 2\int_{1/2}^1 0\cos(n\pi x)\,dx \tag{2.49}$$

$$C_n = \frac{2}{n\pi}\sin\left(\frac{n\pi}{2}\right) \tag{2.50}$$

So the Fourier coefficients are valued at:

$$C_n = \begin{cases} 0 & n = 2, ... \\ \frac{2}{n\pi} \sin\left(\frac{n\pi}{2}\right) & n = 1, 3, ... \end{cases}$$

Bringing the final form to:

$$c(x,t) = \frac{1}{2} \sum_{n\,odd} \frac{2}{n\pi} \sin\left(\frac{n\pi}{2}\right) \cos\left(n\pi x\right) \exp\left(-\frac{n^2\pi^2}{Pe} t\right) \tag{2.51}$$

It is clear from the $-n^2$ in the exponential term and the n term in the denominator that the higher eigenvalues contribute little to the final solution. Additionally, as time increases, the solution will settle at $c(x, \infty) = 1/2$. It is simple to convert this to a dimensional form of the steady state through a simple derivation of:

$$u_{mean} c_y = D \frac{\partial^2 c}{\partial x^2} \tag{2.52}$$

where y is the direction of channel flow and x again is the channel width. Using the same derivation above, the solution arrived to is:

$$c(x,y) = \frac{c_0}{2} + \sum_{n\,odd} \frac{2}{n\pi} \sin\left(\frac{n\pi}{2}\right) \cos\left(\frac{n\pi}{L} x\right) \exp\left(-\frac{D}{u_{mean}} \frac{n^2\pi^2}{L^2} y\right) \tag{2.53}$$

Where $c_0 = c(x \leq L/2, 0)$.

The plot of a steady-state solution for the diffusion problem is shown in Figure 2.1. Each line shows the concentration profile at the lateral position across the microchannel for successive downstream positions. For this problem, $D = 2 \times 10^{-9}\,\mathrm{m^2\,s^{-1}}$, $u_{mean} = 31\,\mathrm{mm\,s^{-1}}$, $L = 300\,\mu\mathrm{m}$. The legend shows the y position for near values, before showing the far field solution, which is complete mixing at $c(x, y \to \infty) = 0.5$. This can be extended if to where the interface of the sample and reagent is not at the centre of the channel, generalising with a factor α, such that $0 \leq \alpha \leq 1$, where the centre of the channel is represented by $\alpha = 0.5$. If this is changed such that the initial condition

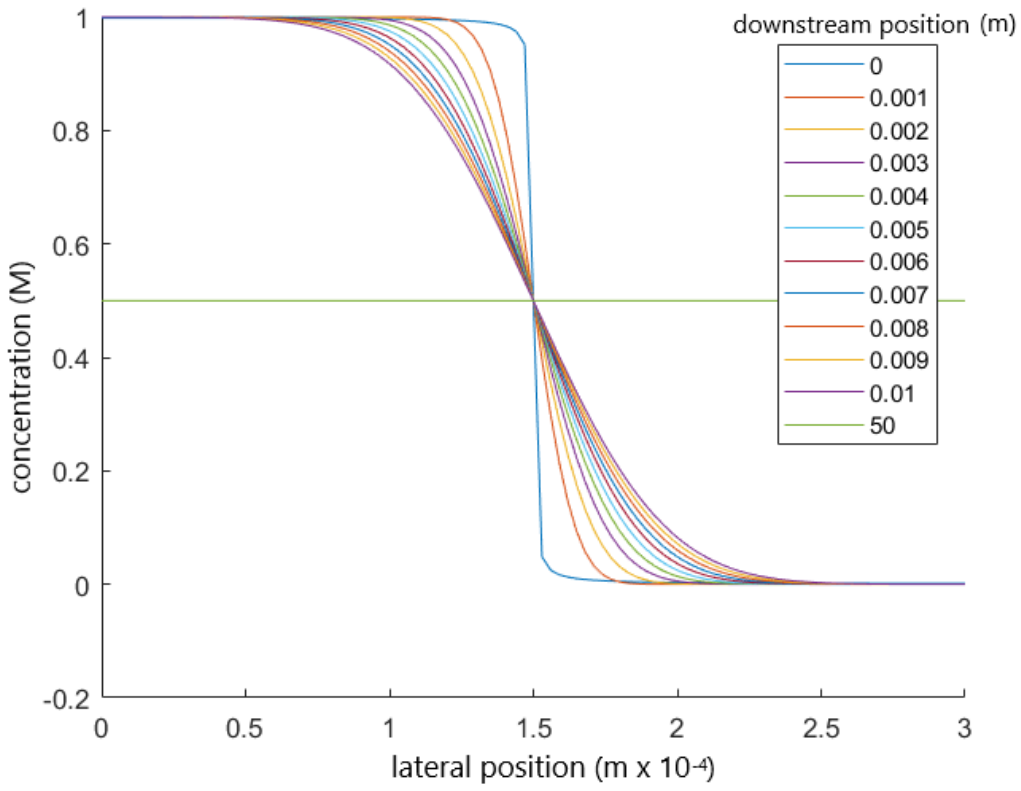

Figure 2.1: Plot of the convection-diffusion steady-state equation, as per Equation (2.53).

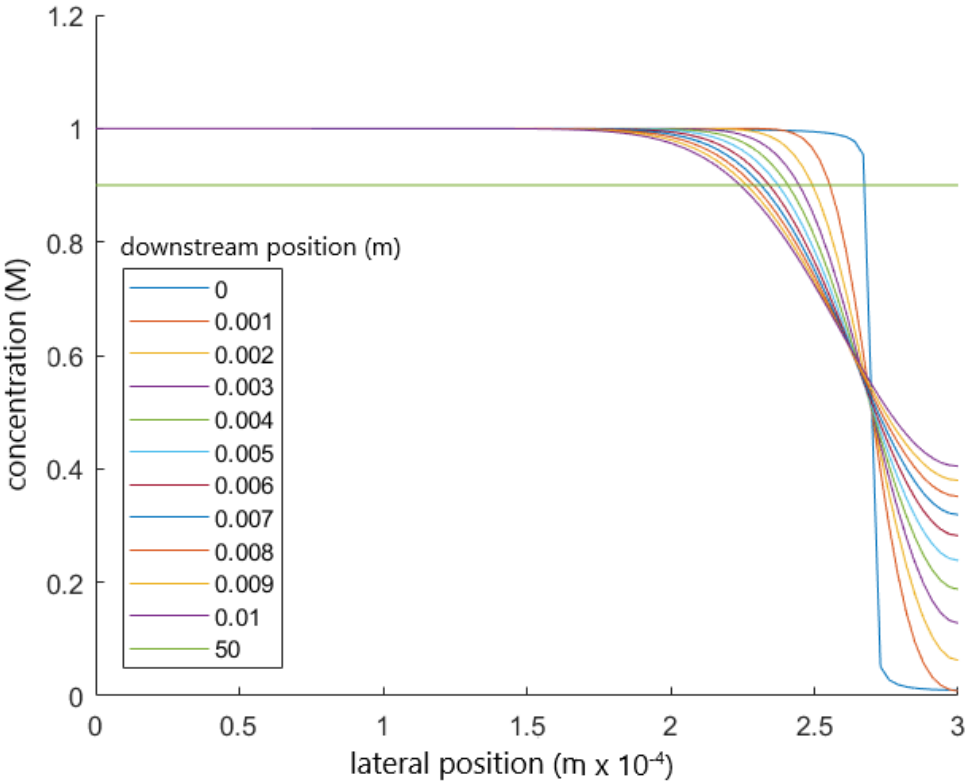

Figure 2.2: Plotted data similar to Figure 2.1, but $\alpha = 0.9$. This is based on Equation (2.54).

$$f(x) = \begin{cases} 1 & 0 \leq x\alpha L \\ 0 & \alpha L < x \leq 1 \end{cases}$$

Then the equation again changes to:

$$c(x,t) = \alpha c_0 + \sum_{n=1} \frac{2}{n\pi} \sin(n\pi\alpha) \cos\left(\frac{n\pi}{L}x\right) \exp\left(-\frac{D}{u_{mean}} \frac{n^2\pi^2}{L^2} y\right) \tag{2.54}$$

2.4 2D model

A fully unified 2D model, incorporating both the lateral position across the microchannel and the channel position using the sections above, would incorporate the convection-diffusion equation, with cross-sectional diffusion and axial convection. If this is done

as per separation of variables:

$$XY\frac{dT}{dt} = D\frac{d^2X}{dx^2}YT - u_{mean}X\frac{dY}{dy}T \tag{2.55}$$

$$\frac{dT}{dt}\frac{1}{T} = D\frac{d^2X}{dx^2}\frac{1}{X} - u_{mean}\frac{dY}{dy}\frac{1}{Y} = -\lambda^2 \tag{2.56}$$

Leading to:

$$\frac{dT}{dt}\frac{1}{T} = -\lambda^2$$

$$u_{mean}\frac{dY}{dy}\frac{1}{Y} = -\mu^2$$

$$D\frac{d^2X}{dx^2}\frac{1}{X} = -(\lambda^2 + \mu^2)$$

Solving for Y and T as first order ODEs:

$$T(t) = T_0 \exp\left(-\lambda^2 t\right) \tag{2.57}$$

$$Y(y) = Y_0 \exp\left(-\frac{\mu^2}{u_{mean}}y\right) \tag{2.58}$$

The final variable takes the sinusoidal form, and assuming $C'(0, y, t) = 0$

$$X = A\cos\left(kx\right), k = -\frac{\lambda^2 + \mu^2}{D} \tag{2.59}$$

Using the BC $C'(L, y, t) = 0$:

$$\sin\left(kL\right) = 0$$

$$kL = n\pi$$

$$X(x) = A_n \cos\frac{n\pi}{L}x \tag{2.60}$$

Recombining the separated variables leaves:

$$c(x,y,t) = \sum^{\infty} A_n \cos\left(\frac{n\pi}{L}x\right) \exp\left(-\frac{\mu^2}{u_{mean}}y - \lambda^2 t\right) \tag{2.61}$$

From this point the problem is overly generalised to define values of λ and μ without further information. If the reaction term is included as $-kX(x)Y(y)T(t)$ in Equation (2.55), this results in an additional constant value, the reaction rate constant k. The separation of variables is not done simultaneously on the reactand and product concentrations, for example the reaction source term for the species transport equation of the product includes the reactant concentration e.g.

$$XY\frac{dT}{dt} = D\frac{d^2X}{dx^2}YT - u_{mean}X\frac{dY}{dy}T + kX_{reactant}Y_{reactant}T_{reactant}$$

The equation would be required for each species, and these are coupled to each other, although not directly linked. This also does not include terms for reactions which include 2 reactants:

$$XY\frac{dT}{dt} = D\frac{d^2X}{dx^2}YT - u_{mean}X\frac{dY}{dy}T + kX_{reactant}Y_{reactant}T_{reactant}X_{reactant,2}Y_{reactant,2}T_{reactant,2}$$

It was determined from the above methods that in the absence of being able to derive a complete model from more basic scenarios – such as the first order reaction only term and convection-diffusion equations in two dimensions – that a numerical approach was warranted. Later in this research, in Chapter 6, using the data collected from the numerical simulations, a reduced order model is constructed which best reflects the input and output of the sensor.

2.5 Conclusion

Several analytical apporached have been examined as a basis for modelling species transport within the sensor. There were issues in incorporating convection, diffusion and reaction kinetics in the same model. While it is possible to derive an analytical model for an inert species and simple channel geometries, increasing complexity – particularly the inclusion of reaction kinetics – adds terms to these that render the problem difficult to model. Where there are multiple phenomena included, such as reaction kinetics in addition to convection and diffusion, then the problem requires more initial and boundary condition to avoid being overly generalised. Without enough imposed conditions, the problem remains an open-ended representation, such as the inclusion of a Fourier series as in Equation (2.51). As the aim of the study was to model a reacting convection-diffusion flow, there was no approach which yielded a fully unified analytical model which was suitable for use in an optimisation algorithm. Moreover, it is also required to model the fluid dynamics within the sensor. The computational power of a microcontroller is limited, and if such a model was to be incorporated onto the sensor, then that expense would not be feasible to be run in real time or using battery power. This is done through the Navier-Stokes equation, for which outside of specific scenarios there is no known analytical solution. Ultimately, from this work, it was not possible to create a closed model to predict sensor output, to determine the concentration of CC, and therefore the analyte's concentration in the input sample. Therefore, it was decided that a numerical simulation was required to obtain sufficient data to allow for use in an optimisation algorithm. This would include similar initial and boundary conditions as mentioned above. The reaction kinetics can be calculated once the steady-state flow field of the system derived thus the numerical approach was deemed better. Chapter 4 proposes to solve for the yield through the use of numerical methods.

Chapter 3

Sensor design

3.1 Principle of operation

3.1.1 Absorbance

The measurement of water quality indicators (WQIs), such as pollutants, is based on classical colorimetric assays. These are well established tests in which a reagent and sample solution are mixed. In the presence of the pollutant, a reaction occurs resulting in a distinct colorimetric complex (CC), which indicates the presence of the substance. In addition, the concentration of CC formed is dependent on the concentration of the pollutant which is initially present.

The Beer-Lambert law is used to calculate this concentration. The attenuation of light through the solution (in dilute concentrations) is dependent on the wavelength and proportional to the concentration of that solution and the optical path length. This is expressed in the form of Equation (3.1).

$$A = \epsilon(\lambda)\, b\, c \tag{3.1}$$

where $\epsilon(\lambda)$ is the molar attenuation coefficient (dependent on wavelength λ), b is the optical path length, and c is the concentration of the pollutant or WQI in the solution. The concentration c is an indirect measurement of the WQI, as it is more explicitly the concentration of the CC present absorbing the light.

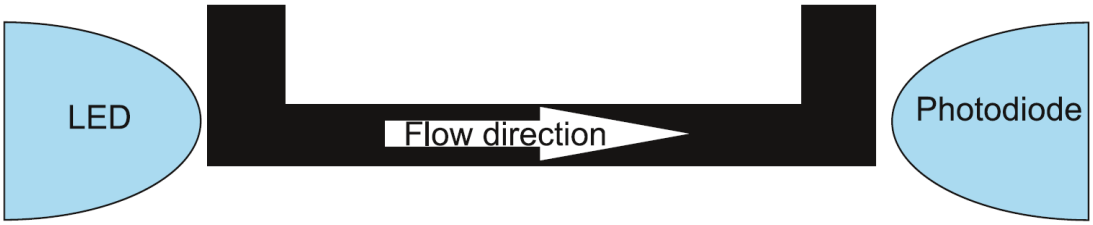

Figure 3.1: Diagram of detector channel.

3.1.2 Limitations

The use of the Beer-Lambert law is limited to the linear range for concentration and absorbance. As the concentration of the WQI increases, there are more interactions between molecules in the solution, which affect the optical properties of the solution. Therefore, as the concentration increases outside of the dilute concentration range, the Beer-Lambert law no longer applies. Further saturation of the solution results in complete absorbance of light within the detector channel.

A simple practical set up for measuring absorbance and calculating absorbance, in accordance with the Beer-Lambert law, is displayed in Figure 3.1. It is a simple sensor setup which comprises a monochromatic light source and photodetector at opposing ends of a microchannel of fixed length containing the reagent and sample solution. There is a limit to the amount of light which can be absorbed by the sample. If there is still light being recorded by the photodetector, it is due to scattered light from the light source or other sources of incident light. This is known as stray light.

3.1.3 Exogenous factors

Outside of the above limitations there are other considerations which can affect the result of an absorbance reading. These include reaction time, interferents, turbidity and sensor degradation. This will be discussed in Sections 3.6 and 3.7.

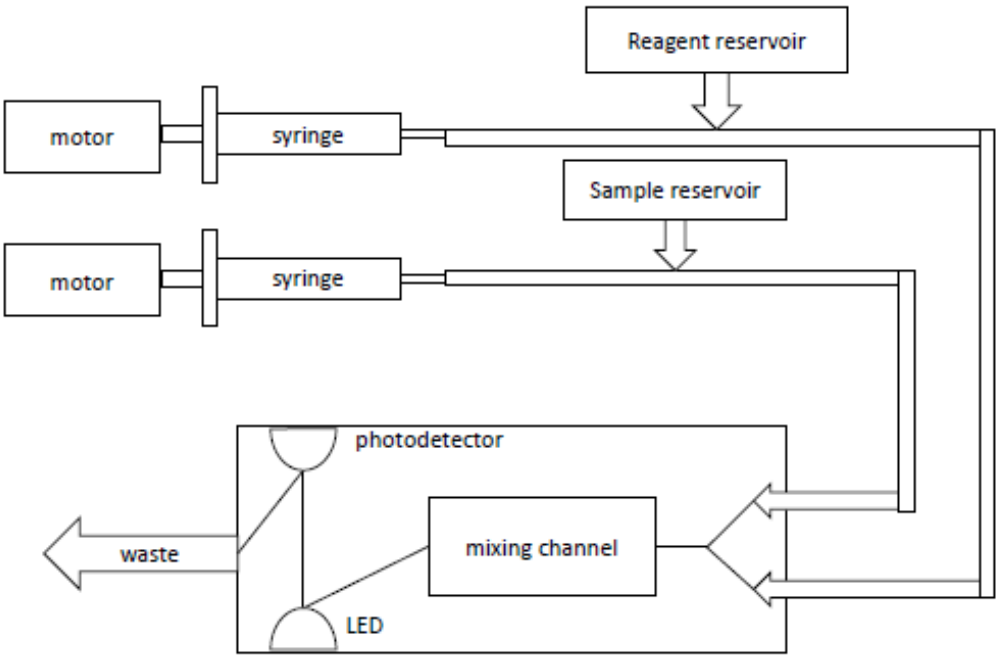

Figure 3.2: A schematic of a prototype Aquamonitrix colorimetric sensor.

3.2 Construction

A schematic of the colorimetric sensor prototype is displayed in Figure 3.2, and a photograph in Figure 3.3. The system compromises on-board reagent and standards. The are pumped into a microfluidic chip, where they are mixed and delivered to a LED and photodiode pair. The absorbance in the colorimetric complex is correlated to the pollutant concentration by the Beer-Lambert law. The waste product is then flushed from the system to a waste reservoir. All components are operated by an on-board microcontroller.

3.2.1 Electrical

The sensor was operated by a Teensy 3.6 microcontroller. This included a constant current driver that controlled LED brightness, a photodiode which recorded incident light intensity that came through the sensor from the LED through detector channel, motor drivers that controlled the DC brush motors which operated the syringe pumps. There was also a real time clock included to log the date and time of recorded measurements.

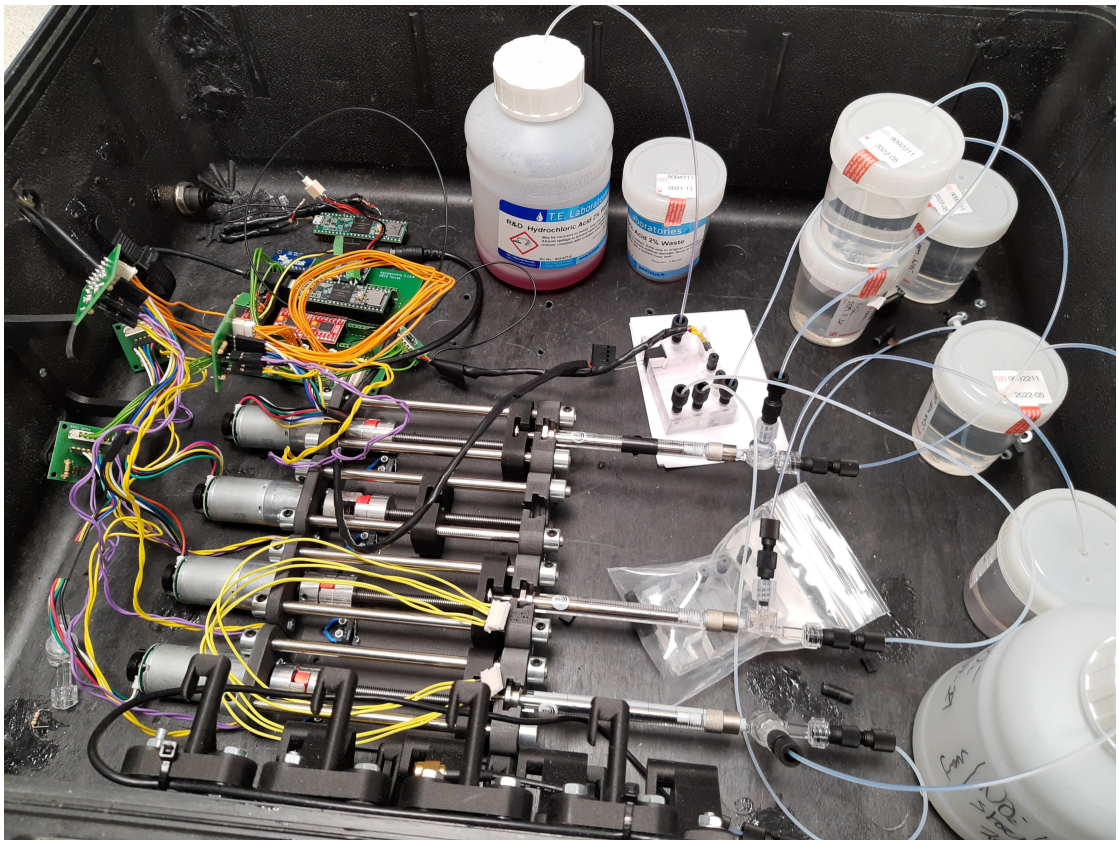

Figure 3.3: A photograph of a prototype Aquamonitrix colorimetric sensor.

3.2.2 Mechanical

The syringes were housed in a custom fabricated 3D printed frame which allowed for independent operation of each pump through separate operated DC brush motors. Blood bags housed the reagents and standards used for testing. The sample was extracted from the monitored water body using peripheral pumps, filters and piping to introduce into an on-board reservoir, where it was stored for ready sampling by the connected syringe.

3.2.3 Chemical

The on-board reagent is based on classical colorimetric assays which varies with the water quality indicators (WQIs) being monitored. The Griess reaction [79] is a classical reaction where an acidic reagent comprising N-(1-Naphthyl)ethylenediamine dihydrochloride (NEDD) and sulfanilamide produces an azo dye in the presence of small concentrations of nitrite (0.1-5 ppm). This test can also be used to measure nitrate, however this requires an intermediary digestive step. A reading of a direct sample and digested

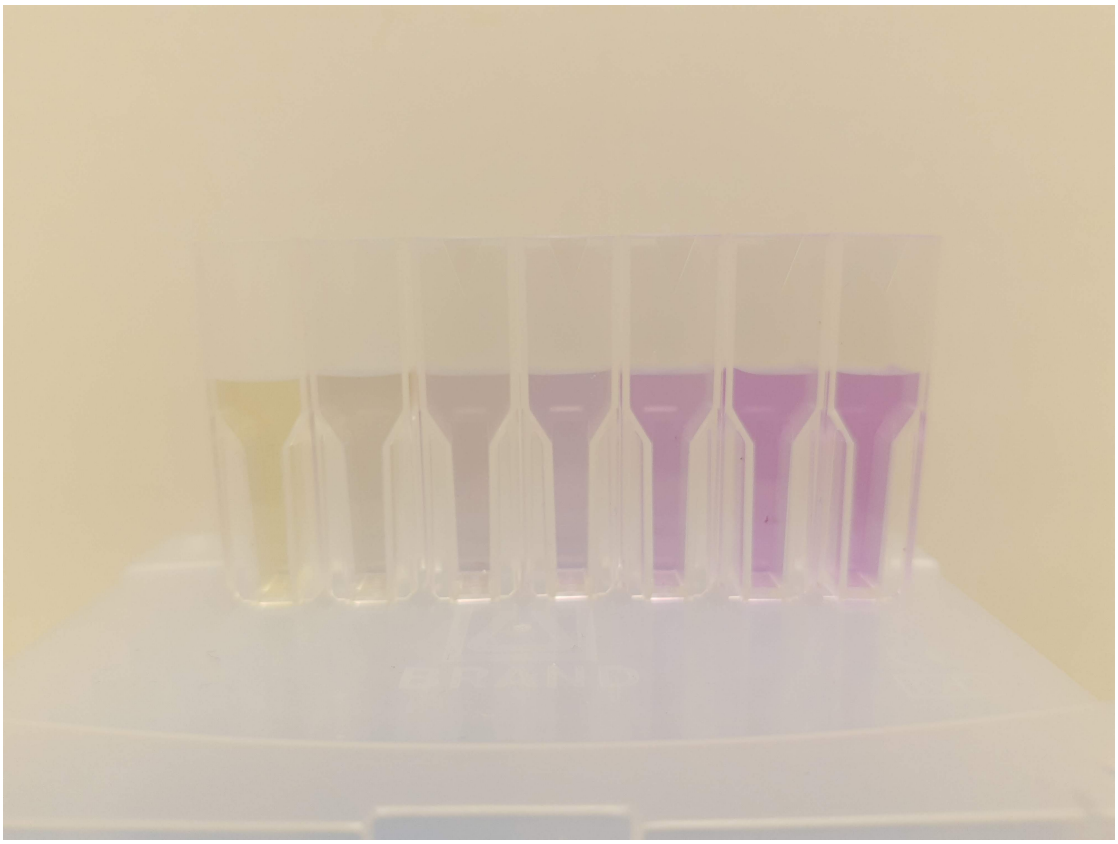

Figure 3.4: pH indicator used on pH buffers ranging from 4 to 10 from left to right in each individual cuvette. Yellow is formed in more acidic, with a change to purple in more basic solutions.

sample allows for the measurement of both nitrite and nitrate. This can be completed with vanadium or also with the use of a cadmium column [80].

The azo dye produced has a high optical absorbance between $525\,\mathrm{nm}$ and $575\,\mathrm{nm}$. pH can also be detected using an indicator reagent. A reagent composed of phenol red, bromophenol blue and chlorophenol red allows for the measurement of pH between 4 and 10 [81]. This produces a dynamic colour scale which is yellow in the lower range and a similar purple colour to the azo dye produced in the Griess reaction, as in Figure 3.4.

Phosphates can also be measured using different reactions depending on sensitivity. The molybdenum blue method is suitable for smaller concentration ranges (0.1-3 ppm). There is also a vanadate-molybdate method which produces a yellow dye in the presence of phosphate in the upper concentration range. There has also been promise shown in detecting and measuring arsenic concentrations using the leucomalachite green method,

producing a green complex, which has high absorptivity at $617\,\mathrm{nm}$ [82].

3.3 Microfluidic chip fabrication

The chip was made using layers of transparent PMMA, in which one layer contains the channels and another the inlets and outlets to the channel network. The PMMA layers were prepared by etching channels into the surface of one of the layers. The most cost-effective method for channel etching is using a CNC milling machine with a small drill bit. This method results in rectangular-shaped channels. It also does not require micromilling to be performed in a cleanroom environment, permitting widespread commercial adoption. Care needs to be taken during the micromilling process in that the resulting swarf is cleared from the channels. Otherwise, this can result in blockages in the finished microfluidic chip. The second layer encloses the channels, and provides an interface to other components through inlet and outlet holes. These are usually threaded to allow for compatibility with standard tubing apparatus. Various sizes and methods exist, but in this study, size M6 was selected, as commercial components could easily be integrated into the channel using this size.

3.3.1 Bonding

To affix the layers together, they were placed in an enclosed space above a layer of ethanol. The ethanol vapour formed above the liquid in the enclosed space. This mildly dissolved the exposed faces of the PMMA layers. After they had been exposed for some time, the layers were clamped together under pressure at a temperature of $80\,^{\circ}\mathrm{C}$. Unbonded sections of an empty chip were identified by seeing refraction between layers upon visual inspection at an angle, where refraction would occur through the enclosed thin layer of air. If there were some unbonded chip sections, liquid ethanol was introduced into the system, and again the layers were clamped together for a few hours to bond them.

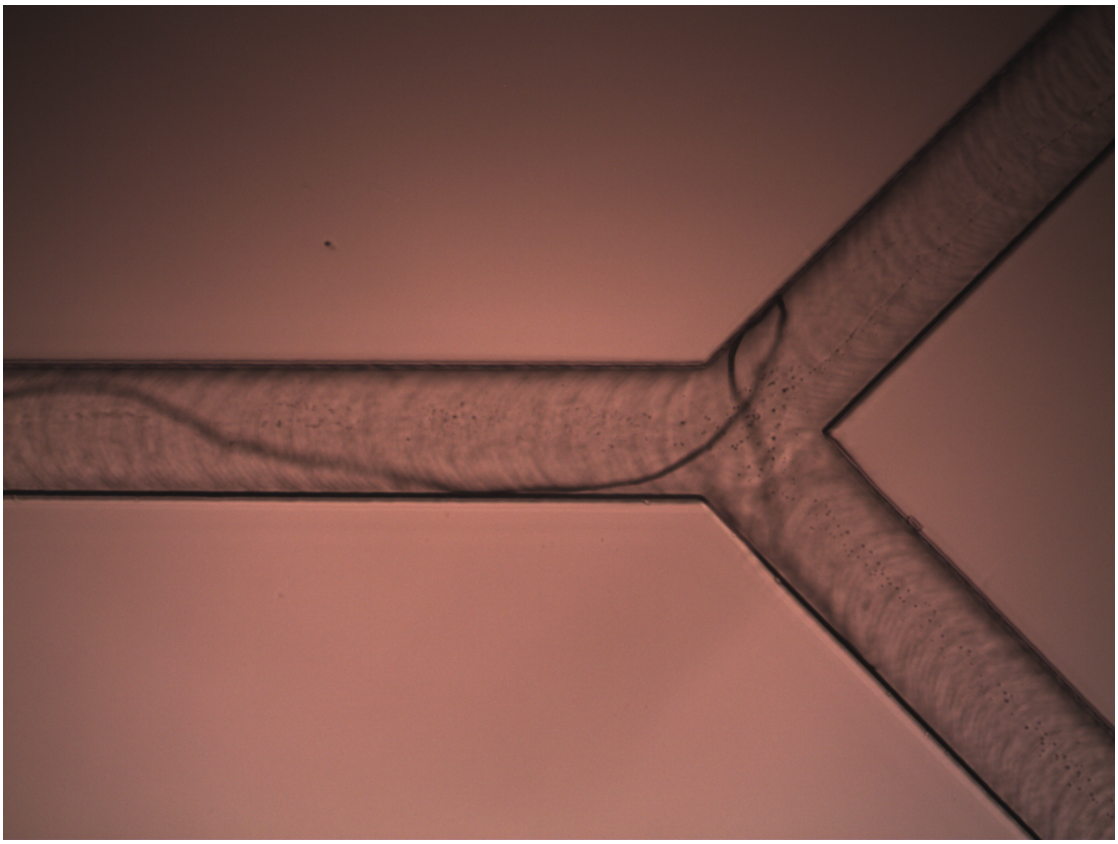

Figure 3.5: Fibre stuck in a microchannel. The channel diameter is $200\,\mu\mathrm{m}$. Also, there are circular grooves in the channels which are an artefact of CNC milling.

3.4 Microchannel surface

The microchannels, when placed under a microscope, showed the circular groove buffer marks, associated with the CNC milling. The importance of a clean environment is to avoid channel obstructions, such as from a fibre or hair. The circular grooves from CNC milling and an entrapped fibre are shown in Figure 3.5.

3.5 Standard operating method

The sensor was operated in a three-step method – displayed in Figure 3.6 – in which a blank solution (0 ppm) and high standard (typically 3 ppm, Irish Environmental Protection Agency [83] describes nitrate levels of less than 4 ppm as high quality) were run before the sample which was to be measured. These standards were used as a basis for continuous calibration, which was intended to mitigate absorption effects, by using the

sample as part of the calibration, incorporating turbidity or the presence of another substance which may absorb at the same wavelength. The below describes the operation of one cycle, however, it is the same for the low standard, high standard and sample cycles.

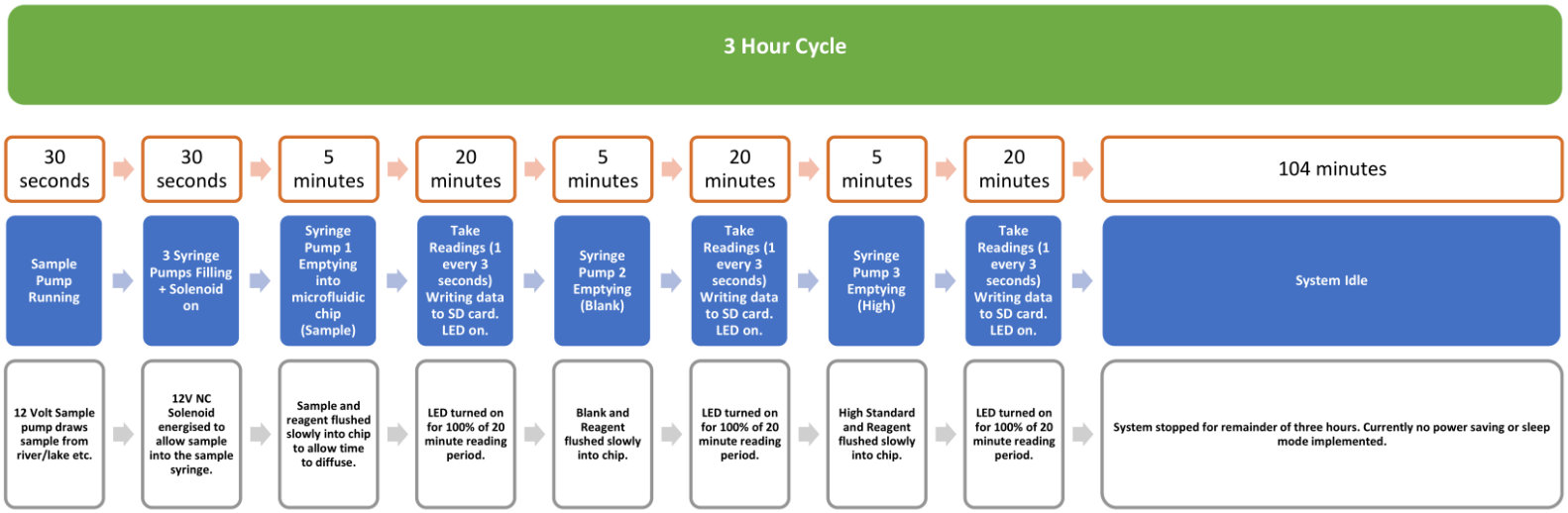

Figure 3.6: Timing diagram for continuous calibration and sample measurement.

If the syringes were any position other than empty, either due to any previous malfunction or power failure, then the syringes were emptied, and fluid ejected to waste. When the syringes were empty, the DC motors were activated, and the syringes drew the reagent (and standard if applicable) from blood bags containing the reagents/standards or from the reservoir if performing a measurement. As the syringes began to draw, a dual check valve restricted flow so that fluid can only tavel from the blood bag or reservoir and sample to the syringe, and then from the syringe to the microfluidic chip. The tubing lengths were kept short to minimise fluid volume within the syringe. There is also dead volume associated with some components such as the dual check valve. For the $0.3\,\mathrm{mm}$ (internal diameter) of circular polyurethane tubing, the volume of fluid resting in the channel equated to $70.7\,\mu\mathrm{L\,m^{-1}}$ of tubing.

The filling rate and quantity were user determined. When the syringes were filled to the prescribed volume, the syringe pumps began to eject the fluid, again at user determined rates. The dual check valve restricted flow so that flow was only directed toward the microfluidic chip, mitigating back flow into the reservoir or blood bags. The flow through the detector channel reached a steady state when the rate of colour development was matched by what was being flushed to waste. After the syringes had been emptied, all mechanical components were deactivated. The LED light source and photodetector were switched on, and for a time of 20 minutes, the voltage of the photodetector was recorded. This allowed for further colour development in the channel, which is important for slower reactions and lower concentrations. The colour development was proportional to the concentration of the reactant. When the low and high standard concentration voltages were recorded, then the sample cycle was run and that concentration voltage was recorded. The two-point calibration curve was used to calculate the sample concentration based on the voltage recorded for the sample. The low, high and sample cycle was repeated every three hours.

3.6 Known sources of error

3.6.1 Stray light

Stray light, as mentioned in Section 3.1.2 results from light which is incident on the photodetector but has not passed through the optical path. This increases the absorbance readings obtained from the sensor and thus have a reduced sensitivity.

3.6.2 Temperature

As temperature has an effect on reaction kinetics, this will impact the rate of colour development in the colourimetric reactions, which if using a fixed reaction time to check for measurement will result in different absorbance readings for the same WQI concentrations. A standalone temperature logger was included within the sensor system, which was used to identify any large temperature fluctuations during deployments.

3.7 Deleterious effects

3.7.1 Bubbles

Bubbles in microfluidic systems can cause deleterious effects in the system. They can be formed in the system due to cracks which may have formed in the piping components or seals which have loosened over time. The introduction of the bubbles in the detector channel has negative effects as they affect the optical properties in the fluid and displace the colorimetric complex which results in absorbance occurring. They are difficult to remove, due to surface tension and limited flow control within the chip. Some solutions include the occasional flushing of the system with a weak solvent, such as sodium hydroxide, which has a lower surface tension with air than an aqueous solution [84].

3.7.2 Staining

For prolonged periods, it is possible for staining to accumulate along the channel walls, including the sides axially at each end of the photodetector channel. This can potentially result in decreased sensitivity over an extended period, as the residual colour can absorb some light after having passed through the detector channel.

3.7.3 Turbidity

Turbidity is present in most natural waters that are sampled. It is caused by small particles in the water, including organic and inorganic particulates, mircoorganisms, clay, silt and algae [85]. Turbidity causes an issue as it will scatter light passing through the detector channel, reducing incident light arriving at the photodetector. In an absorbance-based sensor, this appears as increased pseudo-absorption rather than scattered light. While the coarse mesh at the system inlet will filter out larger particles (such as debris, sand and plant matter) to avoid these blocking the water intake, there will still be some suspended or dissolved particulates (such as sediment and micro-organisms) present. Narrow channels increase the efficiency of the sensor by decreasing channel size and fluid throughput but poses two main issues. Firstly, the back pressure within the system increases drastically, as due to Hagen-Poiseuille law, the pressure is inversely proportional to the fourth inverse power of the channel diameter. Secondly, if the particulates and microorganisms are on a similar scale to the characteristic length, then blockages may occur, which are deleterious to the system.

3.7.4 Interference

Some reactions are prone to interference from other species which may be present in the water sample. Heavy metal cations can also interfere with the absorption of light in this reaction. This is investigated later in Chapter 5 which examines the effects of different interferents in the Griess reaction.

3.8 Output and noise

Output noise is derived from inherent electrical noise in the system. The noise process much of the time can be attributed to being white noise, in that it has zero mean and unit variance. This can be removed with an averaging filter if it holds true. One of the most common methods used to filter out this noise is through a moving average filter, using a previous amount of n points. The longer the window, the greater the averaging and more aggressive the smoothing. This can have some deleterious effects however when examining peaks and slopes, in that an averaging filter narrows and flatten peaks and curves, the effect becomes more pronounced as the window is widened. Therefore, it is important that a minimal filtering effect is applied to preserve as much of the underlying output data as possible. One method which is established in spectroscopy is the use of the Savitzky-Golay filter [86]. This operates by using a sliding window, and by using the centre and adjacent points either side, an n^{th} order polynomial is approximated to the curve. This is more advantageous from a spectroscopic sense in that there is no narrowing or flattening of peaks, although it can only be performed en bloc rather than real time. Much of the underlying output data are conserved. The difficulty in attenuating the noise in a sensor is selecting a window size so that degree of noise which affects the absorbance reading is minimised and therefore the measured output data from the sensor are as clean as is obtainable.

3.8.1 Error propagation

Uncertainties in voltage are propagated through Beer-Lambert's Law. The Beer-Lambert law can be expressed as absorbance having a linear relationship to both the molar extinction coefficient as well as the optical path length, defined in Equation (3.1). The voltage measurement from a photodetector can be used to determine absorbance, as the voltage has a linear relationship to the change in light intensity.

$$A = -\log \frac{V}{V_0} \tag{3.2}$$

where V is the measured photodetector voltage of the sample, and V_0 is the blank voltage reading, used as a baseline value. It can be seen that the maximum voltage value corresponds to near no absorbance. As the voltage is the directly measured output as opposed to the absorbance, the error due to noise is propagated through Equation (3.2). To determine ΔA, the derivative is obtained and then manipulated:

$$\Delta A = \frac{\partial A}{\partial V} \Delta V$$

To get the below expression:

$$\Delta A = -\frac{1}{\ln 10} \cdot \frac{\Delta V}{V} \tag{3.3}$$

As can be seen with Equation (3.3), the higher absorbance (lower voltage) values also result in greater uncertainty in the upper range of absorbance data collected, as $\Delta A \propto 1/V$. Readings from lower concentration solutions are more sensitive to error (Equation (3.3)) from stray light.

3.8.2 Turbidity

There is also an effect from the suspended particules in the solution flowing through the detector channel. While there is the effect of low concentrations mentioned above, there is additionally some effects which result from the flow of the liquid. It is noted that in solutions of notable turbidity, there are additional particles which are large enough to scatter light away from the photodetector. This effect occurs at all wavelengths in the visible spectrum. This effects results in a detected pseudo-absorbance, which is difficult to distinguish from absorbance of light from the medium for a monochromatic light source in the photodetector. There are some methods used to separate out this effect though this is discussed in Chapter 5.

3.8.3 Quantisation error

There was a quantization error associated with the sensor. As the signal read by the photodetector was analogue, this need to be converted using an analogue-digital converter (ADC) for reading by the microcontroller. As the ideal response for an ADC and perfect response are not the same, there is an error which is introduced as a result. Additionally, some analogue values may also be rounded to the same nearest discrete value. At any time, the quantization error is defined as the difference between the input analogue value and the output voltage value. From a rounding perspective in this research, the gain of the ADC is set at such that the least significant bit is $250\,\mu\mathrm{V}$, thus this error is associated as $\pm 125\,\mu\mathrm{V}$. To reduce the effect of this, the ADC process can be adjusted by introducing a shift of $125\,\mu\mathrm{V}$ to reduce this effect. Temperature also has an effect on the performance of an ADC, although for the purpose of on-site deployment this is not of primary concern as the standard operating temperatures ranged from $243\,\mathrm{K}$ to $400\,\mathrm{K}$ which was well within any natural deployment, in regards to noise and data rate [87].

3.8.4 Interference

Interference, although not noise, affects the output, and can result in false readings. This can stem from known interferents from a reaction, which for classical colorimetric assays are well known. For example, the Griess reaction is known to have interference from a number of cations, including metals such as iron(2+), gold(3+), mercury(2+), lead(2+), silver(+), chloroplatinate and metavanadate [88]. As mentioned above, turbidity can also make it difficult to determine true absorbance from light scattering from suspended particles. American Public Health Association [88] also mentions that there is interference possible from nitrogen trichloride and free chlorine, although this is deemed unlikely as due to the incompatibility with nitrogen with all of these compounds' coexistence in the same solution.

3.8.5 Drift

Drift is also another factor to consider in the quality of output data. Sensors drift for a variety of factors over time, due to electrical components and chemical degradation. One of the chemical processes to consider is that of a low concentration standard, such as nitrite. Nitrite is unstable at low concentrations, and for long-term deployments the inclusion of a low standard means that this will degrade over a short time span. It is possible to increase the stability of the standard through the inclusion of an acid such as nitric acid, however it is recommended in [88] that there should be no acidification of the sample prior to measurement, as low pH can interfere with colour development.

3.8.6 Kalman filtering

If the underlying behaviour of the sensor is known, then a more accurate output reflecting the true behaviour can be constructed using a filter, such as a Kalman filter. The Kalman filter allows for a more accurate reading of the true underlying state of the system, accounting for known noisy processes where the pure system is known, or at least estimated. The noise can be included in the input and the output, and the Kalman filter works to produce a best guess of the underlying state where the underlying model is understood. The Kalman filter can be used in real-time, and advantageous in that regard as the only parameters required to produce an estimate are the input and previously measured output.

3.9 Microcontroller

The microcontroller used was a Teensy 3.6. This was connected to multiple components, including an RTC DS3231 real time clock, motor controllers, ADC ADS1115, (all from AdaFruit Technologies) and a custom 3D printed syringe holder connected to motor controllers. A constant current driver ensured the LED remained at a set brightness. A syringe pump was used to control the rate of flow within the system. Each of the syringes on the pump was a S.G.E. gas tight Luer lock $1\,\mathrm{mL}$ syringe from Tragan Scientific

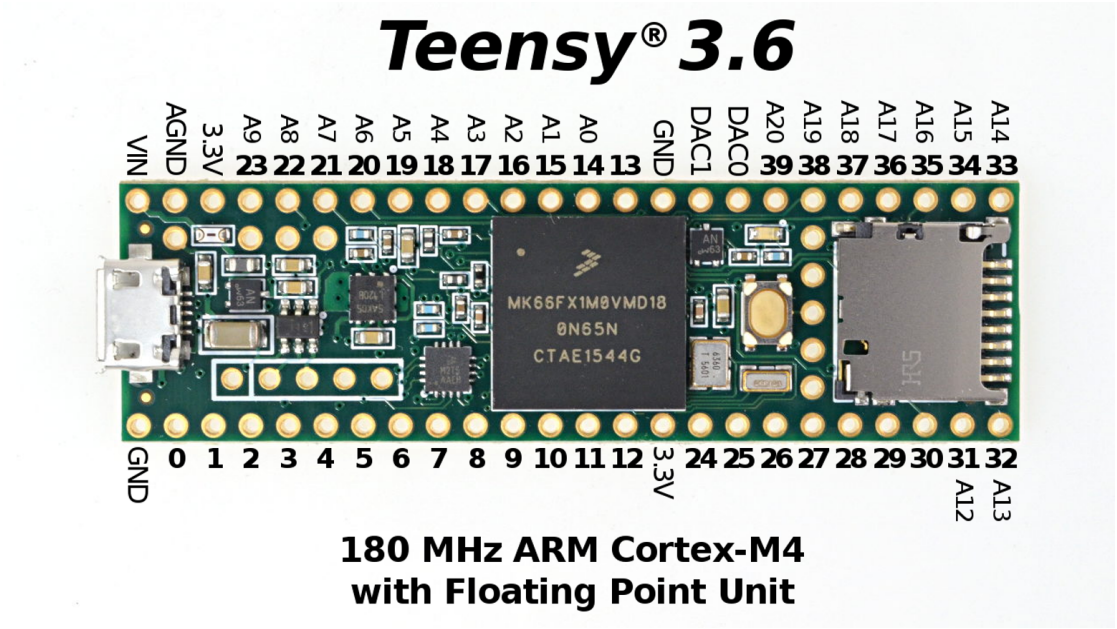

Figure 3.7: Teensy 3.6. This is a sample of the microcontroller that was used to operate the sensor.

Australia Pty Ltd. Each syringe was connected to an independent brush motor (RF-370CA-15370 from Mabuchi Motor Company), allowing for each of the syringes to run. The whole system was encased in an opaque black Peli 1600 Case from Peli Products S.L.U. The PMMA microfluidic chip was designed and provided by T.E. Laboratories Ltd. Micromilling of the PMMA was carried out by EFJ Engineering (Dublin, Ireland). The PMMA layers were bonded through solvent vapour bonding, as described by Ogilvie et al. [89]. Power was supplied by a 12 V lithium ion battery (Voltaic V88). Nitrite standards were prepared using sodium nitrite (Sigma Aldrich).

It includes a variety of components such as a mounted SD card to write to and store data and a USB port to allow for firmware updates and serial monitoring and plotting when connected to a computer. There are digital and analogue pins which allow for respective control of components in each paradigm. There is an LED pin, which can be writen to as a pulse width modulation output to control the brightness. The microcontroller can be operated in either $3.3\,\mathrm{V}$ or $5.5\,\mathrm{V}$. For this research, the Teensy was operated at $3.3\,\mathrm{V}$.

3.10 Sample collection code

The code which was uploaded to the code incoporated each of the above components to work in operating the syringes, collecting data from the photodiode, and then outputting and writing the data to disk.

3.10.1 Algorithm

1. The data handling was set up so that a new file/folder was written to the disk.

2. The system looked to see if any of the limit switches were triggered. If the syringes were detected to be out of place, then the syringes were emptied and set back to the ejected position.

3. The syringes began to draw liquid into the prescribed ratios at full speed, up to a total fill volume of $1\,\mathrm{mL}$. The ratio 1:1 meant that each syringe filled with 0.5 mL, while the ratio 9:1 meant that the reagent syringe made up 0.1 mL of total fluid volume.

4. While the syringes are filling, the photodiode begins to read data at 20 Hz with the LED off. This is to check to see if there are any sources of light interference coming from outside the system.

5. The syringes reached their fill position, before ejecting at a speed commensurate to their fill volumes, so that they would finish at the same time. At this point the LED switches on and readings are taken. Some data from the previous run is collected just before the fluid inside is flushed from the system. In the case of the lower end of the calibrated range or for slower reactions, there is not much detected at this stage.

6. The syringes are fully emptied. The LED and photodiode remain switched on, taking readings within the detector. At this stage, any slower reactions are detected here with decreased voltage as any colour development takes place.

3.10.2 Arduino code

The full code is included in Appendix A.

3.11 Alignment of chip

To ensure that new chips were aligned, an LED holder and photodetector holder were produced using a 3D printer. The construction was such that the pieces slotted into either side of the photodetector channel, such that the LED and photodiode were opposite ends of the detector channel. The LED holder had a small aperture which was printed to line up with the detector channel, and to limit the light transmitted throughout the PMMA sheet. The photodiode holder additionally had an aperture, albeit this was larger to accommodate the face of the detector channel.

However, when running these intially, there tended to be some issues with getting readings. Sometines, there was a high voltage reading, even when the detector channel was completely saturated. This was attributed to poor shielding of stray light within the system, allowing for excess light to enter the system. Due to sensitivity of the photodiode, any large amount of stray light reaching the photodetector resulted in deleterious effects. In one case, the photodetector detected no absorbance when a fully saturated solution was contained in the detector chanel.

To combat this, copper tape was used to shield as much of the light around the hole, leaving a much smaller space around where the detector channel meets the edge of the channel. Copper, in addition to the stray light from the LED, also absorbs any infrared light which may emanate from within the sensor casing. The copper tape was applied to the wall of the channel in few segments to ensure as little extra material as possible. This was important as when the photodiode holder was inserted, the copper was removed if there was insufficient flattening between the holder and the tape on the chip.

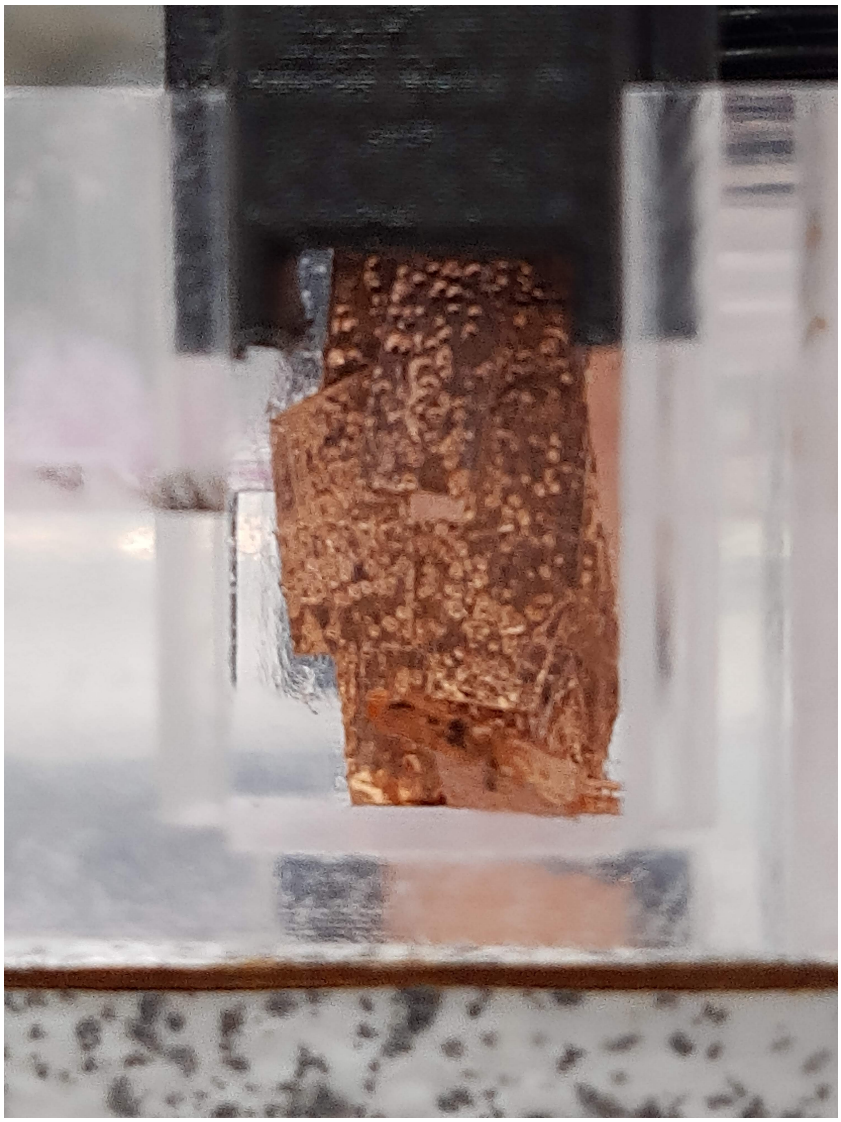

Figure 3.8: End of detector channel. Copper tape was used to block as much stray light as possible.

Chapter 4

Computational modelling and optmisation

Optimal reagent flow rates in colorimetric sensors have not been thoroughly explored in the literature. Typical reagent amounts used in microreactors are 10% or 50% of total mixture volume [48]. Other considerations include using an imbalance in inflow rates between reagent and sample, to increase intermingling, encouraging mixing [90]. If the reagent use is minimised, then the deployment time of the sensor can be extended. The aim of this chapter is, using a numerical model, to present a methodology for optimising the process parameters of a Y-junction continuous reactive flow system with the end goal being the efficient commercial operation of a microreactor and simplification of the control decision process. This was achieved using multi-objective optimisation of finite-differences based CFD simulations of the reactive-convection-diffusion equation modelling the mixing of sample and reagent within the microreactor. The objective functions for the optimisation minimise unused reagent, and therefore maximises the yield of the colorimetric complex for given reaction kinetics. The optimisation algorithm employed can identify operating parameter values along a Pareto front that satisfy the objective functions, such as reagent inflow ratio, reactant concentration, and mean flow speed, in the mixing channel for a given reaction and microreactor design. Two dimensional simulations are conducted to decrease solution time whilst maintain-

ing accuracy, permitted by assuming a high height-to-width aspect ratio. The reaction kinetics were chosen to mimic the Griess reaction, used in the nitrite colorimetric assay. Thus, the optimisation is limited to a two-dimensional Y-junction facilitating a two-step reaction with fixed reaction rates.

4.1 Introduction

In environmental monitoring, there is a need to develop in-situ chemical sensors capable of detecting pollutants in the environment over long time periods in order to identify trends and temporary events, such as illegal dumping [91]. The alternative method is grab-sampling, which requires significant costs and labour, and can only generate limited data.

Deployment time depends on the rate of consumption of on-board reagents. Therefore, to extend deployment time, it is desirable to use the minimum quantity of reagent required to return a detectable (and maximised) yield. Microfluidics-based microreactors facilitate the use of minute sample and reagent quantities to perform these colorimetric assays, allowing for a longer period before the on-board waste needs to be emptied and safely disposed of, and the reagents and standards refilled. This approach allows for the most efficient use of reagent, by maximising the yield of a reaction given a situation of limited supply.

An issue with this technology, however, is ensuring sufficient mixing occurs within the microreactor. Microfluidic flow is characterised by smooth laminar flow, high internal pressure and length scales between $1 \times 10^{-6}\,\mathrm{m}$ and $1 \times 10^{-4}\,\mathrm{m}$. Under the conditions of slow flow speed, characterised by a low Reynolds number $Re \leq 2000$, and small length scales, species transport and hence mixing, is diffusion limited. When mixing is improved, yield is increased, in turn maximising sensor response and sensitivity.

Numerical simulation, such as computational fluid dynamics (CFD) is often used to verify theoretical micromixer design, commonly using commercial software such as COMSOL or ANSYS [16, 92, 17, 93, 94, 20, 32, 21]. In these studies, the governing equations are usually the incompressible Navier-Stokes and convection-diffusion equa-

tions, often computed in a 3D, regularly spaced structured mesh [93]. There is also open source software in development for CFD: FiPy [95], OpenFOAM (C++ based), and FEniCS [96]. uFlow [97] is a programme which facilitates micromixer design on consumer-grade software but is limited to full-height cylindrical column obstructions in a microchannel, and does not account for reacting flow. Though not as widely adopted as ANSYS or COMSOL, the extensibility and cross-platform compatibility of codes generated in Python and similar means these solutions are becoming more prevalent in scientific computing in industry. The solution presented here is created in Python and builds on the philosophy of open-source software to ensure an extensible and platform agnostic solution available to any institution.

4.2 Method

4.2.1 Physical properties

The problem posed was a dual-inlet micromixer, where the reagent and reactant were mixed. The resulting yield was expected to vary with the sample-to-reagent ratio coming into the inlet (u_{in}), where absent to sole reagent flow was denoted by $0 \leq u_{in} \leq 1$, where 0 is no reagent present. The concentration of the reactant and the mean flow speed were denoted by u_{mean} and c_{in} respectively. The mean flow speed of the mixed solution was fixed for varying u_{in}, which meant that when u_{in} was reduced, the speed of the reactant inlet was adjusted such that the mean flow speed in the mixing channel remained constant. The mean flow speed of the mixed solution was fixed for varying u_{in}, which meant that when u_{in} was reduced, the speed of the reactant inlet was adjusted such that the mean flow speed in the mixing channel remained constant. Species transport was modelled using the reacting convection-diffusion equation as per Equation (4.2). The low flow speed and small characteristic length L meant that the diffusive term was dominant in Equation (4.2).

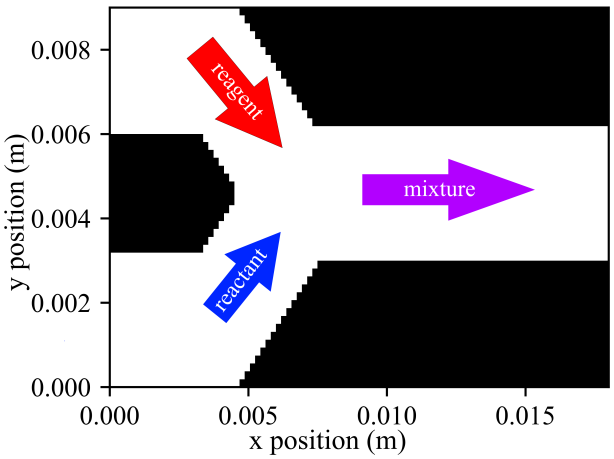

Figure 4.1: Two-dimensional spatial domain of the problem showing the boundary conditions of the problem.

Geometry A Y-junction shaped micromixer was selected for simulation with an inlet angle of $60°$. The micromixer was structured such that confluence and each of the inlets were all the same width. There was also a channel width separation between the two parallel inlets prior to mixing. Figure 4.1 shows the two-dimensional problem, with inlets, outlet and flow direction defined. The arrows show the direction of flow, and the associated species form each. The inlet concentrations were of fixed value at the inlet, with the reagent and reactant originating as per arrow. The mixture then reacts before exiting via a zero-flux condition normal to the outlet.

The preceding distance sufficiently exceeded the entrance length L_e (calculated using Equation (4.1)) to ensure the stabilisation of the laminar flow profile due to the small length scale and fluid viscosity.

$$L_e \approx 0.03\, L \cdot Re \tag{4.1}$$

where L is the channel width, Re the Reynolds number and ν the kinematic viscosity of water. The fluid was assumed to be aqueous in nature, incompressible and isothermal, as were any reactions in the micromixer. The flow was assumed to be steady, as the delivery of the fluid into the microreactor was provided by a smooth motor from a non-elastic channel, meaning that pressure was consistent throughout the flow, and no oscillations or delay between the motor and the reactor were experienced. Each

of the species' concentrations were assumed dilute so species-species interaction was negligible in scale to fluid-species interaction, meaning the aqueous properties of the fluid were unaltered. The parallel plates assumption justified a 2D representation of the mixer, by assuming a large channel aspect (width-to-height) ratio. The physical domain was composed such that the channels were constantly filled with aqueous fluid, enclosed by an impermeable solid.

4.2.2 Governing equations

Species transport Once the flow solution was obtained, the species transport problem was solved numerically using Equation (4.2).

$$\frac{\partial c_i}{\partial t} = D\nabla^2 c_i - \mathbf{u} \cdot \nabla c_i + R_A \tag{4.2}$$

where c_i is the concentration of a species i at a defined position and time $c_i(x, y, t)$, $\mathbf{u}$ is the location-specific fluid velocity, and R_A is a source term for a reaction A, which is a function of the species' concentrations. The reaction modelled here was assumed to be a second order two step-equation, with a fast first-step and second slow step, based on the Griess reaction. The reaction rates selected were $800\,\mathrm{L\,mol^{-1}\,s^{-1}}$ and $15\,\mathrm{L\,mol^{-1}\,s^{-1}}$, approximated values taken from a chemometric study of this reaction [98]. Five species were modelled which included the analyte, first reagent, intermediate species, second reagent and product, labelled $c_1, ..., c_5$ respectively. The reactions were non-reversible. A simplified representation of the reaction is shown in Equation (4.3).

$$c_1 + c_2 \rightarrow c_3 + c_4 \rightarrow c_5 \tag{4.3}$$

Therefore, for the first reaction A, the source term is as defined by Equation (4.4).

$$R_A = k_A c_1 c_2 \tag{4.4}$$

Similarly for reaction B, this term is as defined by Equation (4.5).

$$R_B = k_B c_3 c_4 \tag{4.5}$$

This leads to five coupled species transport equations, Equations (4.6) to (4.10).

$$\frac{\partial c_1}{\partial t} = D\nabla^2 c_1 - \mathbf{u} \cdot \nabla c_1 - R_A \tag{4.6}$$

$$\frac{\partial c_2}{\partial t} = D\nabla^2 c_2 - \mathbf{u} \cdot \nabla c_2 - R_A \tag{4.7}$$

$$\frac{\partial c_3}{\partial t} = D\nabla^2 c_3 - \mathbf{u} \cdot \nabla c_3 + R_A - R_B \tag{4.8}$$

$$\frac{\partial c_4}{\partial t} = D\nabla^2 c_4 - \mathbf{u} \cdot \nabla c_4 - R_B \tag{4.9}$$

$$\frac{\partial c_5}{\partial t} = D\nabla^2 c_5 - \mathbf{u} \cdot \nabla c_5 + R_B \tag{4.10}$$

Fluid flow Flow was modelled using the incompressible, steady-state Navier-Stokes equations, as per Equation (4.11).

$$\frac{D\mathbf{u}}{Dt} = -\frac{1}{\rho}\nabla p + \nu\nabla^2\mathbf{u} - \frac{f}{\rho}\mathbf{u} \tag{4.11}$$

where p is pressure, ρ is fluid mass density, f/ρ is an impermeability term, and D/Dt is the material derivative, as in Equation (4.12).

$$\frac{D}{Dt} = \mathbf{u} \cdot \nabla \tag{4.12}$$

Another consideration was the incompressible continuity equation, Equation (4.13).

$$\nabla \cdot \mathbf{u} = 0 \tag{4.13}$$

The incompressibility condition meant that there was no explicit relationship between

pressure and flow velocity in the governing equations. The Poisson pressure equation was used in this study, defined by Equation (4.14), which allows velocity and pressure to be solved on co-located nodes. Equation (4.14) was derived from the divergence of Equation (4.11).

$$-\frac{1}{\rho}\nabla^2 p = \left(\frac{\partial u}{\partial x}\right)^2 + \left(\frac{\partial v}{\partial y}\right)^2 + 2\frac{\partial u}{\partial y}\frac{\partial v}{\partial x} \tag{4.14}$$

4.2.3 Discretisation

The finite difference method was chosen as the discretisation method. The code that has been produced is specific to the problem posed for this research, it is simple and sufficient for evaluating the below problems. The governing equations were discretised using the first and second order central differencing schemes (CDS), represented in Equations (4.15) and (4.16). This was chosen initially as the simplest implementation of the problem. The size of the mesh was limited for computational efficiency. As the number of nodes at the boundaries were quite small, lower order BCs were used to accommodate this, and to ensure that as many nodes as possible were not subject to BCs.

$$\frac{\partial u}{\partial x} = \frac{u_{i+1} - u_{i-1}}{2\Delta x} \tag{4.15}$$

$$\frac{\partial u}{\partial x} = \frac{u_{i+1} - 2u_i + u_{i-1}}{\Delta x^2} \tag{4.16}$$

Most of the discretisations were completed using CDS, except for the convective component of Equation (4.11) which was discretised using the first order upwind scheme, as in Equation (4.17). CDS has a second order truncation error, while the upwind scheme has a first order truncation error. The first order upwind scheme was discretised as:

$$\frac{\partial \mathbf{u}}{\partial x} = u^+ \frac{u_i - u_{i-1}}{\Delta x} + u^- \frac{u_{i+1} - u_i}{\Delta x} \tag{4.17}$$

The values of u^+ and u^- were chosen as boolean values, such that

$$u^+ = \begin{cases} 1 & \frac{\partial u}{\partial x} > 0 \\ 0 & \frac{\partial u}{\partial x} \leq 0 \end{cases}, \quad u^- = \begin{cases} 1 & \frac{\partial u}{\partial x} < 0 \\ 0 & \frac{\partial u}{\partial x} \geq 0 \end{cases}$$

For Equation (4.2), using CDS on the convection component resulted in instability and divergence. To counteract this, a first order upwind scheme was used, introducing a first order truncation error. To account for this, a corrective term was inserted into the equation, evaluated using Equation (4.18).

$$\frac{\partial c}{\partial x} - \frac{c_i - c_{i-1}}{\Delta t} = \frac{1}{2}\Delta x \frac{\partial^2 c}{\partial x^2} + O\left(\Delta x^2\right) \tag{4.18}$$

4.2.4 Navier-Stokes equation

Equation (4.11) was discretised using the aforementioned methods. The transient term was assumed to be zero-valued, as only the steady state solution of the equation was of interest. If each derivative in Equation (4.11) is discretised using CDS, then velocity at each location can be evaluated using Equations (4.19) and (4.20). In each of these equations, the term K refers to f/ρ as defined in Equation (4.11).

$$u_{i,j}^{n+1} = \frac{\nu\left(\frac{u_{i+1,j}+u_{i-1,j}}{\Delta x^2} + \frac{u_{i,j+1}+u_{i,j-1}}{\Delta y^2}\right) - v_{i,j}\frac{u_{i,j+1}-u_{i,j-1}}{2\Delta y} - \frac{p_{i+1,j}-p_{i-1,j}}{2\Delta x}}{\frac{u_{i+1,j}-u_{i-1,j}}{2\Delta x} + K + 2\Delta x^{-2} + 2\Delta y^{-2}} \tag{4.19}$$

$$v_{i,j}^{n+1} = \frac{\nu\left(\frac{v_{i+1,j}+v_{i-1,j}}{\Delta x^2} + \frac{v_{i,j+1}+v_{i,j-1}}{\Delta y^2}\right) - u_{i,j}\frac{v_{i,j+1}-v_{i,j-1}}{2\Delta x} - \frac{p_{i,j+1}-p_{i,j-1}}{2\Delta y}}{\frac{v_{i,j+1}-v_{i,j-1}}{2\Delta y} + K + 2\Delta x^{-2} + 2\Delta y^{-2}} \tag{4.20}$$

4.2.5 Poisson pressure equation

The pressure equation is derived from the divergence of the Navier-Stokes equation, rearranging such that the pressure derivative is a function of the other equation variables. Part of what makes this work is the assumption that the fluid is incompressible, as many

terms in the intermediate steps between Equation (4.11) and Equation (4.13) are an identity of $\nabla \cdot \mathbf{u} = 0$. The discretisation of Equation (4.14) is:

$$p_{i,j}^{n+1} = \frac{\rho\left(\left(\frac{u_{i+1,j}-u_{i-1,j}}{2\Delta x}\right)^2 + \left(\frac{v_{i,j+1}-v_{i,j-1}}{2\Delta y}\right)^2 + 2\frac{u_{i,j+1}-u_{i,j-1}}{2\Delta y}\frac{v_{i+1,j}-v_{i-1,j}}{2\Delta x}\right)}{2\Delta x^{-2} + 2\Delta y^{-2}} + \frac{\frac{p_{i+1,j}-p_{i-1,j}}{\Delta x^2} + \frac{p_{i,j+1}-p_{i,j-1}}{\Delta y^2}}{2\Delta x^{-2} + 2\Delta y^{-2}} \quad (4.21)$$

4.2.6 Reacting convection-diffusion equation

Similarly to Equation (4.2) If the source term in Equation (4.2) assumed to take the form $R_A = k\, c_i\, c_j$ then:

$$\frac{\partial c_i}{\partial t} = D\nabla^2 c - \mathbf{u} \cdot \nabla c_i + k\, c_i\, c_j \quad (4.22)$$

$$\frac{c^{n+1} - c^n}{\Delta t} = \frac{D}{\Delta x^2}\left(c_{i+1} - 2c_i + c_{i-1}\right) - \frac{\mathbf{u}}{2\Delta x}\left(c_{i+1} - c_{i-1}\right) + k\, c_i\, c_j \quad (4.23)$$

where $n+1$ represents the value at the next time step. On the right hand side, all terms are from time step n but are omitted for clarity. The variables u_{max} and v_{max} were valued at the maximum values found for each of u, v from the solution of Equation (4.11). This was required to ensure stability in each time step evaluating Equation (4.24). For the RCD equation in two dimensions, rearranging for $c_{i,j}^{n+1}$, the equation is:

$$c_{i,j}^{n+1} = c_{i,j}^n + \frac{D\Delta t}{\Delta x^2}\left(c_{i+1,j}^n - 2c_{i,j}^n + c_{i-1,j}^n\right) + \frac{D\Delta t}{\Delta y^2}\left(c_{i,j+1}^n - 2c_{i,j}^n + c_{i,j-1}^n\right) - \frac{u_{max}\Delta t}{2\Delta x}\left(c_{i+1,j}^n - c_{i-1,j}^n\right) - \frac{v_{max}\Delta t}{2\Delta y}\left(c_{i,j+1}^n - c_{i,j-1}^n\right) + R_A\Delta t \quad (4.24)$$

4.2.7 Boundary conditions

The boundary conditions (BCs) included both Dirichlet and Neumann type BCs. The Dirichlet BCs included no-slip walls ($\mathbf{u}_{walls} = 0$), a zero pressure outlet ($p_{outlet} = 0$). Fixed values were applied at the inlets for the reactant and reagent concentrations. The first inlet pertained to c_1 (reactant), while the second inlet had equal fixed values for c_2 and c_4 (reagent inlet). The reactant inlet has a fixed concentration such that $c_{inlet,reactant} = c_{in}$, and $c_{inlet,reagent}$ had a fixed concentration which related to the reagent composition. As mentioned in Chapter 3, in the case of the Griess test for nitrite, this is a two step reaction, in which a diazonium salt is formed between the nitrite and acid, before it couples with NEDD to form an azo dye [99]. The inlet velocity profiles were fixed as laminar flow profiles, evaluated using Equation (4.25). The Neumann BCs included zero-gradient for both species transport and flow velocity normal to the outlet ($\nabla c_{outlet} = \nabla u_{outlet} = 0$). In addition, there was no flux through the channel walls ($\mathbf{n}_{walls} \cdot \nabla c_{walls} = 0$).

$$u(r) = 1.5 u_{mean} \left(\left(\frac{L}{2} \right)^2 - r^2 \right) \tag{4.25}$$

Where r is the position along the outlet, $-L/2 \leq r \leq L/2$, and $u(r = 0) = 1.5\, u_{mean}$.

4.2.8 Solver methods

Velocity and pressure were explicitly calculated, using an appropriate under-relaxation value of 0.1 between iterations to ensure stability. One velocity iteration was followed by five pressure iterations. Iterations were repeated up until either a maximum of 2×10^5 iterations were completed, or until the relative tolerance between iterations was less than 1×10^{-5}. Following this, the same theory was applied to the reacting flow simulation until either a maximum time had been reached, or a steady state solution had been achieved, using the same above relative tolerance. In addition to under-relaxation, there was also a Courant number of 0.2 which was used between time steps for the RCD

equation solution, to ensure stability for the explicit solution.

Pressure correction To solve pressure correctly, an additional term ($\nabla \cdot \mathbf{u}$) was added into Equation (4.14). The modified Poisson equation is defined by Equation (4.26). The pseudotime constant Δt_i in the corrective term was selected using the minimum value possible which reduced the velocity divergence introduced into the numerical simulation while still converging to a solution.

$$-\frac{1}{\rho}\nabla^2 p = \left(\frac{\partial u}{\partial x}\right)^2 + \left(\frac{\partial v}{\partial y}\right)^2 + 2\frac{\partial u}{\partial y}\frac{\partial v}{\partial x} - \frac{1}{\Delta t_i}\left(\frac{\partial u}{\partial x} + \frac{\partial v}{\partial y}\right) \tag{4.26}$$

The discretisation of the corrective term was taken to be:

$$-\frac{1}{\Delta t_i}\left(\frac{u_{i+1,j} - u_{i-1,j}}{2\Delta x} + \frac{v_{i,j+1} - v_{i,j-1}}{2\Delta y}\right)$$

Which was added to Equation (4.14) to make:

$$\begin{aligned} p_{i,j}^{n+1} = & \frac{\rho\left(\left(\frac{u_{i+1,j}-u_{i-1,j}}{2\Delta x}\right)^2 + \left(\frac{v_{i,j+1}-v_{i,j-1}}{2\Delta y}\right)^2 + 2\frac{u_{i,j+1}-u_{i,j-1}}{2\Delta y}\frac{v_{i+1,j}-v_{i-1,j}}{2\Delta x}\right)}{2\Delta x^{-2} + 2\Delta y^{-2}} \\ & + \frac{\frac{p_{i+1,j}-p_{i-1,j}}{\Delta x^2} + \frac{p_{i,j+1}-p_{i,j-1}}{\Delta y^2}}{2\Delta x^{-2} + 2\Delta y^{-2}} \\ & - \frac{1}{\Delta t_i}\left(\frac{u_{i+1,j} - u_{i-1,j}}{2\Delta x} + \frac{v_{i,j+1} - v_{i,j-1}}{2\Delta y}\right) \end{aligned} \tag{4.27}$$

Algorithm The algorithm for running the simulations are summarised in the flow diagram in Figure 4.2. Further detail is described below:

Momentum and pressure algorithm:

- The Neumann BCs were applied.
- The Dirichlet BCs were applied.
- Equation (4.11) was evaluated, with subsequent under-relaxation.

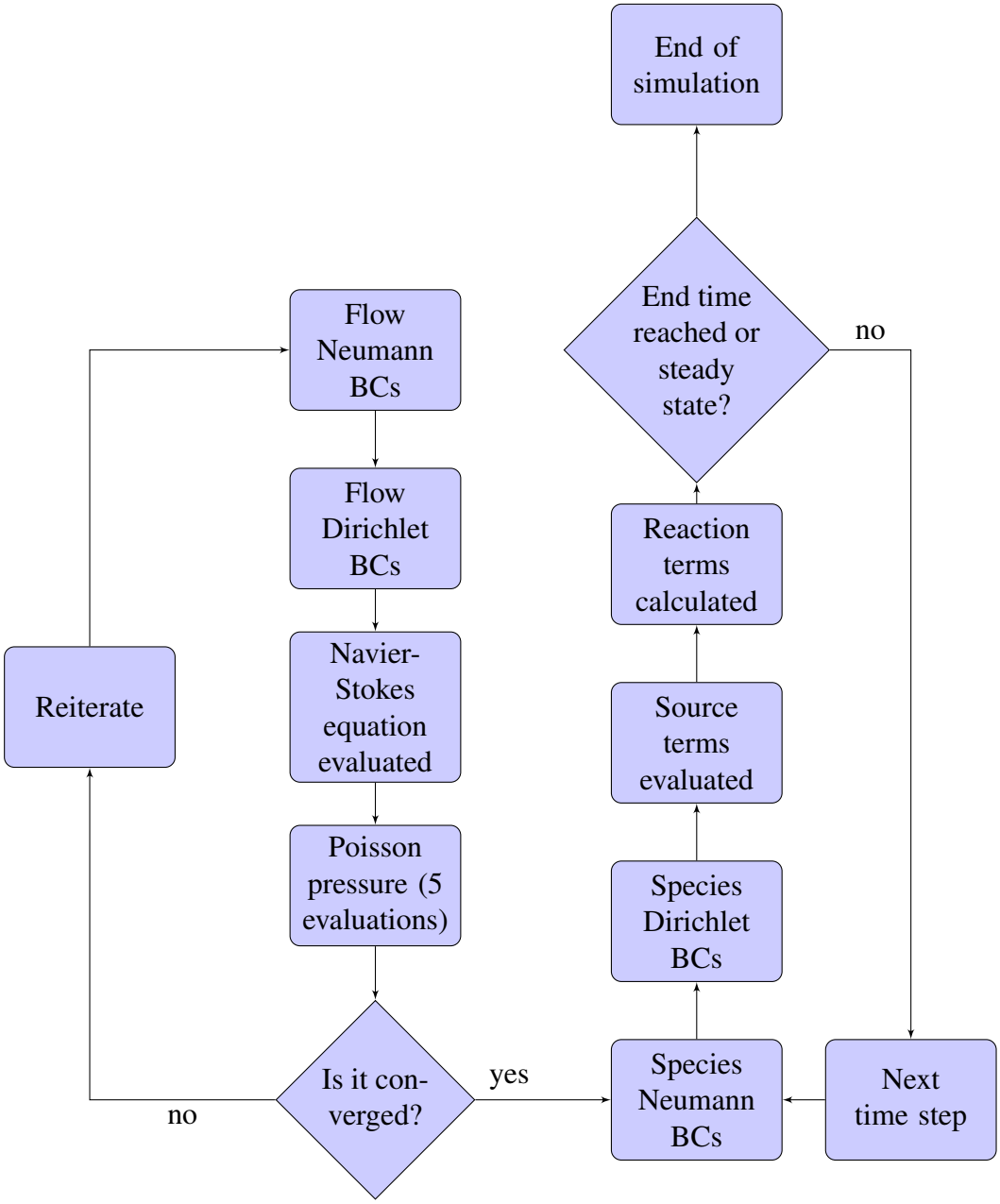

Figure 4.2: Flow chart for fluid dynamics solution.

- Equation (4.26) was evaluated 5 times in succession, with subsequent under-relaxation for each time.
- If the largest relative change in velocity was below 1×10^{-5} between iterations, then the solution was deemed to have converged.

Species transport and reaction algorithm:

- The Neumann BCs were applied.
- The Dirichlet BCs were applied.
- Equations (4.4) and (4.5) were calculated.
- Equations (4.6) to (4.10) were evaluated given a time step of the smallest time constant times the Courant number.
- If the relative change in species was below 1×10^{-5} or the final time step had been achieved, then the solver stopped.

4.2.9 Grid independence study

The grid independence study was performed by looking at the outlet velocity value between fourfold successive refinements of the grid, to ensure that the solution was not dependent on the grid resolution. Independence was deemed to be achieved when the peak velocity value at the outlet varied less than 2% between grid refinements.

4.2.10 Surrogate model creation

A surrogate model was implemented and the optimisation routine was performed on this. This was to reduce the number of CFD simulations that needed to be run, as running separate CFD simulations for each sample was excessive use of available computational resources. The parameter values were restricted to the following ranges: $0.05 \leq u_{in} \leq 0.5$, $1 \times 10^{-6}\,\mathrm{mol\,L^{-1}} \leq c_{in} \leq 50 \times 10^{-6}\,\mathrm{mol\,L^{-1}}$, $32.1 \times 10^{-3}\,\mathrm{mm\,s^{-1}} \leq u_{mean} \leq 96.3 \times 10^{-3}\,\mathrm{mm\,s^{-1}}$. The reagent concentration was fixed at $1 \times 10^{-6}\,\mathrm{mol\,L^{-1}}$.

Table 4.1: Parameters used in the multi-objective optimisation.

Optimisation parameter	value
Number of generations	50
Population size	200
Children per individual sample	2
Cross probability	0.7
Mutation probability	0.2

The model was produced using multilinear regression, using the simulation parameter values c_{in}, u_{in} and u_{mean} – as well as interacting and higher order terms – as inputs. The outputs were the total flux at the outlet of both the product (yield) and the reagent (unconsumed reagent i.e. waste), using Equations (4.28) and (4.29). To include the interactive and higher order terms, terms were created using the Legendre polynomials. This was to minimise co-linearity between higher and lower order normalised terms. The input and output data were scaled to the domain and range $(-1, 1)$ using minimum-maximum normalisation as part of the process. This new basis of Legendre polynomials was used to generate the surrogate model, defined in Equations (4.30) and (4.31). Cross-validation was used to assess the accuracy of the regression model. The mean squared error (MSE) was used to determine the closeness of the regression model output to the simulation output.

4.2.11 Multiobjective optimisation

The optimisation was performed using the NSGA-II (Non-dominated Sorting Genetic Algorithm II) algorithm [100]. NSGA-II was chosen over other optimisation methods, as the parameter values selected between generations of parameter sets can be mapped to the Pareto front of the objective function outputs. In contrast, the SIMPLEX algorithm is used where the problem posed is linear in nature. The Monte Carlo method was not used as the problem was deterministic in nature.

An initial population of samples – containing the three input parameters (grouped as $\mathbf{x}$) – was generated randomly, using the same bounds as in Section 4.2.10. After

evaluation of each of the cost functions (the same as the objective functions), the best scoring samples were recorded and a new population produced. Each cost function was evenly weighted, such that the maximised yield and minimised waste were equally taken into account. The best scoring samples from each generation were recorded, and these were the samples that formed the Pareto front. The parameters which controlled the simulation included the size of the initial population, number of children per sample between generations and mutation. The list of parameters used in the optimisation are provided in Table 4.1.

$$f_1 = c_{product} \cdot (\mathbf{u} \cdot \mathbf{n}_{outlet}) \tag{4.28}$$

$$f_2 = c_{reagent} \cdot (\mathbf{u} \cdot \mathbf{n}_{outlet}) \tag{4.29}$$

$$f(\mathbf{x}) = \sum_{k=0}^{N_3} \sum_{j=0}^{N_2} \sum_{i=0}^{N_1} b_{i,j,k} p_{i,j,k}(\mathbf{x}) \tag{4.30}$$

$$p_{i,j,k}(\mathbf{x}) = L_i(x_i) \cdot L_j(x_j) \cdot L_k(x_k) \tag{4.31}$$

4.2.12 Dimensionality

While the problems were solved in 2D, the use of 3D was also explored as an initial basis for modelling. The additional dimension is the channel height, as the 2D simulation only included width and length. This allowed for an output which calculated the cross-sectional average concentration across the outlet. However, the 3D models took many hours to solve compared to the 2D models, when using FDM in three dimensions and CDS for all discretisations. To compensate for this, operator splitting methods were explored in an attempt to reduce the 3D problem to a number of 2D problems. One of the methods explored as an alternative was the advection direction implicit (ADI) method, where each direction is solved for implicitly in separate steps, while solving for the other dimensions explicitly. Due to the time required to formulate all of the

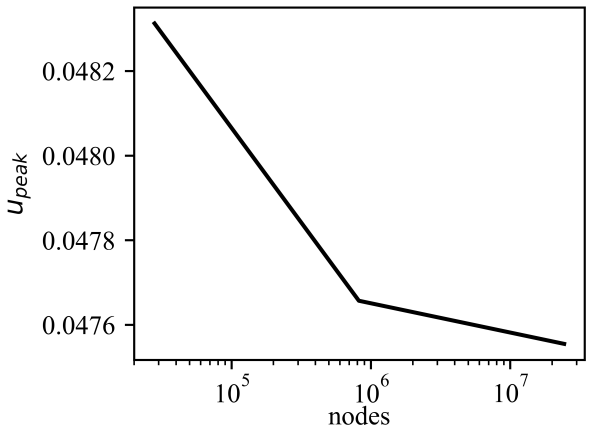

Figure 4.3: Independence study performed on the velocity flow problem. The figure shows that the independence was achieved for 8.2×10^5 nodes. Also to note that for each velocity value, the pseudotime constant used corresponded to ($\Delta t_i = 5 \times 10^{-5}\,\mathrm{s}, 5 \times 10^{-5}\,\mathrm{s}, 7.5 \times 10^{-5}\,\mathrm{s}$) respectively.

equations for 3D, and the runtime for each of the simulations, the research was restricted to 2D.

4.2.13 Software packages

The python implementation of multilinear regression used was from scikit-learn [101], and that of NSGA-II from DEAP [102]. Figures were generated using matplotlib [103].

4.3 Results

4.3.1 Grid independence study

The study found that independence was achieved for $\Delta x = L/16$, corresponding to 8.2×10^5 nodes. Figure 4.3 shows the convergence of the peak velocity value near the outlet. The difference in value between the peak velocity value achieved numerically and the expected numerical value, obtained by using Equation (4.25), was less than 1%. There was some difference between the analytical and numerical values. This was reduced by using the smallest pseudotime constant possible for the pressure correction term avoided divergence. This was found to be $\Delta t_i = 5 \times 10^{-5}\,\mathrm{s}$ for each grid resolu-

Table 4.2: Surrogate model order assessment, where all cross terms are included, based on the Legendre polynomial series.

Order	R^2	MSE
(1,1,1)	0.920	0.0240
(1,2,1)	0.927	0.0280
(2,1,1)	0.953	0.0162
(2,2,1)	0.962	0.0176
(2,1,2)	0.961	0.0173
(2,2,2)	0.865	0.1045
(3,1,1)	0.962	0.0159
(3,1,2)	0.972	0.0169
(4,1,1)	0.968	0.0162

tion, except for the highest resolution where $\Delta t_i = 7.5 \times 10^{-5}\,\mathrm{s}$. There was also some second order truncation error due to the discretisation method used for Equation (4.11).

4.3.2 Surrogate model creation

Data generation The surrogate model produced was evaluated using the coefficient of determination (measure of fit), denoted as R^2, and MSE. Table 4.2 shows the evaulation process of differing orders of Legendre polynomials used to generate a model based on the earlier generated simulation data. Each of the columns are the highest order term of each parameter (u_{in}, c_{in}, u_{mean}), the coefficient of determination of the resultant regression model, and the mean squared error of the model, found using tenfold cross-validation. The best scoring orders of Legendre polynomials for each parameter were $(3, 1, 1)$. An improved fit to the underlying model was identified by an increase in R^2 with a corresponding decrease in MSE. For underfitting, the opposite was true, in that MSE increased and R^2 decreased, for example $(2, 2, 2)$, while an increase in both R^2 and MSE suggested overfitting, such as $(2, 2, 1)$. The coefficients (pertaining to the underlying scaled Legendre polynomials) for the $(3, 1, 1)$ model are shown in Table 4.3. The correlation between any polynomial pairing within the 100 samples was inside the value range $(-0.3, 0.3)$.

Table 4.3: Coefficients from the regression model, corresponding to the Legendre polynomials. The subscript refers to the order of the terms (u_{in}, c_{in}, u_{mean})

	b_{000}	b_{001}	b_{010}	b_{011}
f_1	-0.60522572	-0.26725832	0.37938667	-0.21212199
f_2	-0.16088697	0.55636641	0.00643831	0.00799292
	b_{100}	b_{101}	b_{110}	b_{111}
f_1	-0.3749331	0.23480473	-0.43433342	0.25080721
f_2	0.63304414	0.31143557	-0.00163493	0.02650434
	b_{200}	b_{201}	b_{210}	b_{211}
f_1	0.2157251	-0.19845382	0.05694145	0.1296476
f_2	-0.11891176	-0.08094448	-0.056412	-0.03120968
	b_{300}	b_{301}	b_{310}	b_{311}
f_1	0.00492149	-0.07054822	-0.15989852	0.15466139
f_2	-0.12237017	-0.06394282	-0.04072421	0.01975708

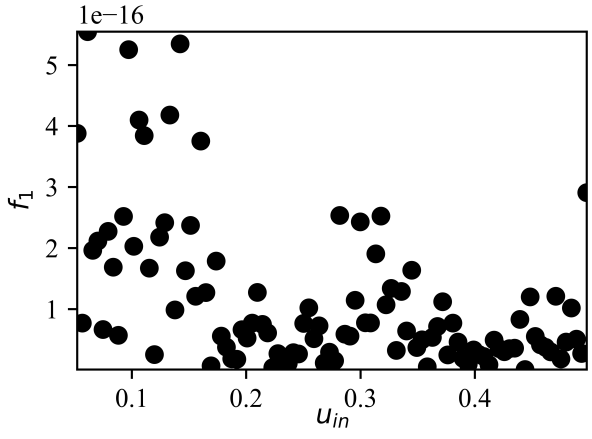

Figure 4.4: A plot of f_1 vs u_{in}, yield as a function of proportion of reagent in test solution.

The highest yields were obtained using lower reagent proportions.

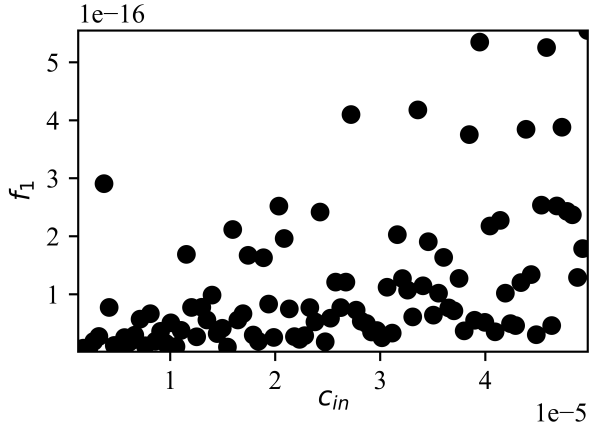

Figure 4.5: A plot of f_1 vs c_{in}, yield as a function of the sample concentration. Higher yields were obtained at higher sample concentrations.

4.3.3 Multiobjective optimisation

Objective function results Figures 4.4 and 4.5 are scatter plots that compare both u_{in} and c_{in} to yield. The yield decreased with increasing reagent proportions in the test solution. Also, the yield increased with an increased sample concentration in the solution. There were multiple factors leading to this result. Firstly, at the confluence of reagent and product at the reagent inlet, the fluid interface is located nearer the channel wall when u_{in} is smaller. Additionally, the parabolic flow speed means that the mixture flows axially at a slower flow speed than at the centre of the channel. This increases residence time, allowing more time for a yield to be generated. Secondly, with reagent occupying a larger fraction of the mixing channel, yield is not necessarily increased as most reaction occurs along the interface. Reagent displaces analyte, meaning that yield is ultimately limited.

The waste as a function of u_{in} and c_{in} does not show as clear of a correlation with f_2 as f_1. The scatter charts of u_{in} against unusued reagent in Figure 4.6 suggests a positive correlation, while for c_{in} this appeared to be completely random, as in Figure 4.7. It can be inferred that u_{in} is highly influential in predicting yield and effective in determining waste, however c_{in} is somewhat helpful for yield but not a reliable indicator for waste produced.

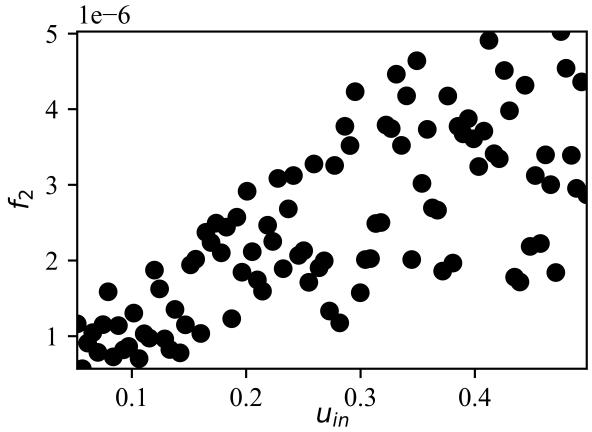

Figure 4.6: A plot of f_2 vs u_{in}, unusued reagent as a proportion of reagent in the test solution. Waste and reagent ratio are positively correlated i.e. more reagent in the test solution results in more unused reagent.

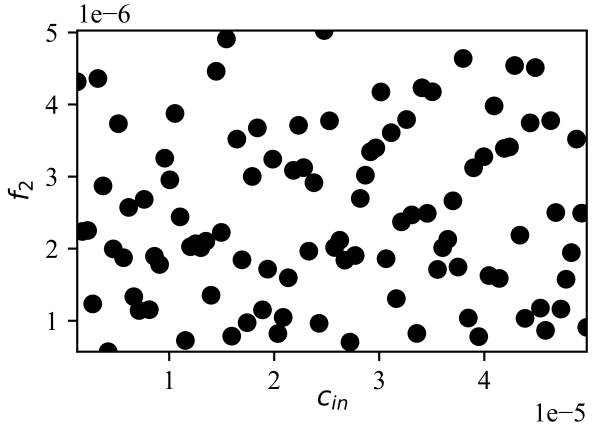

Figure 4.7: A plot of f_2 vs c_{in}, sample concentration as a function of unused reagent. There is no correlation evident between reactant concentration and unused reagent.

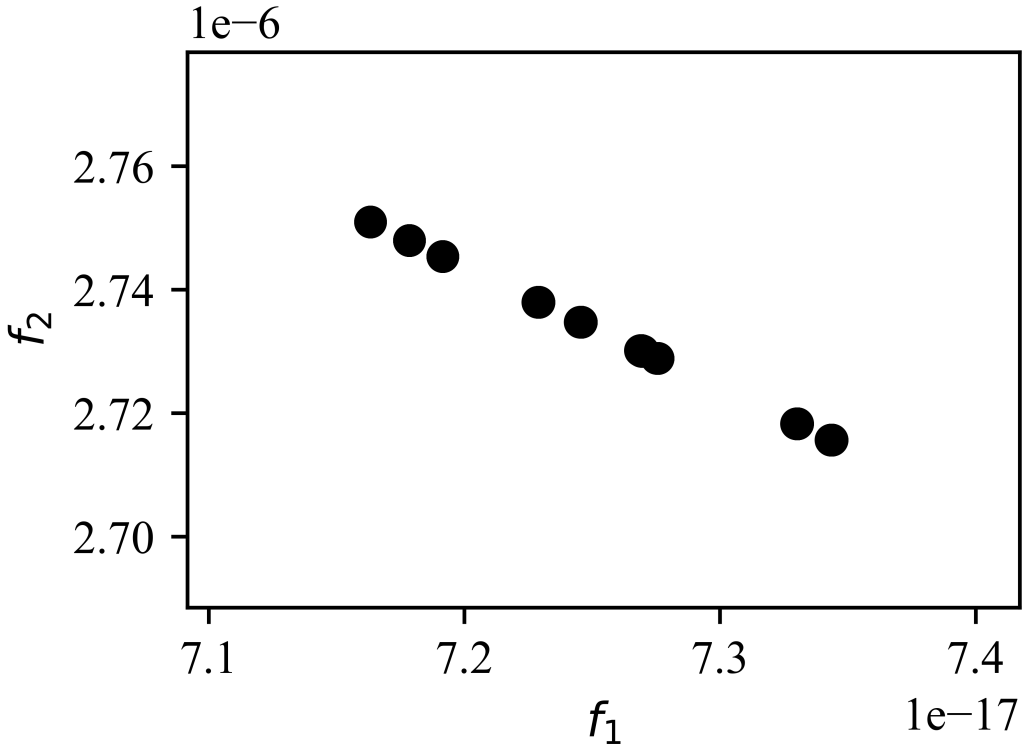

Figure 4.8: Pareto front resulting from the multiobjective optimisation routine. This is a small linear region in which to increase yield (f_1), the waste also has to be increased.

Flow speed The parameter u_{mean} has been omitted from here below as for all samples the minimum sampled value was optimal, as a slower flow increases residence time, both increasing yield and reducing waste (when considered in terms of flux). Time is also a practical consideration in microreactor yield, as an infinitesimal u_{mean} means the convection time approaches infinity. u_{mean} is directly controlled by the pumping mechanism. There may be other practical considerations as inexpensive components will have mechanical limits on the minimum speed they operate. Additionally, there may be extra-experimental constraints on time which makes this infeasible. If this is too slow, there may be saturation of the product, which is undesirable for colorimetric reactions in environmental sensors.

Pareto front Figure 4.8 shows the minimum yield and maximum waste values that resulted from the optimisation. The Pareto front was a small linear region in the solution space. It can be seen from the corresponding points on the scatter plots in Figures 4.9

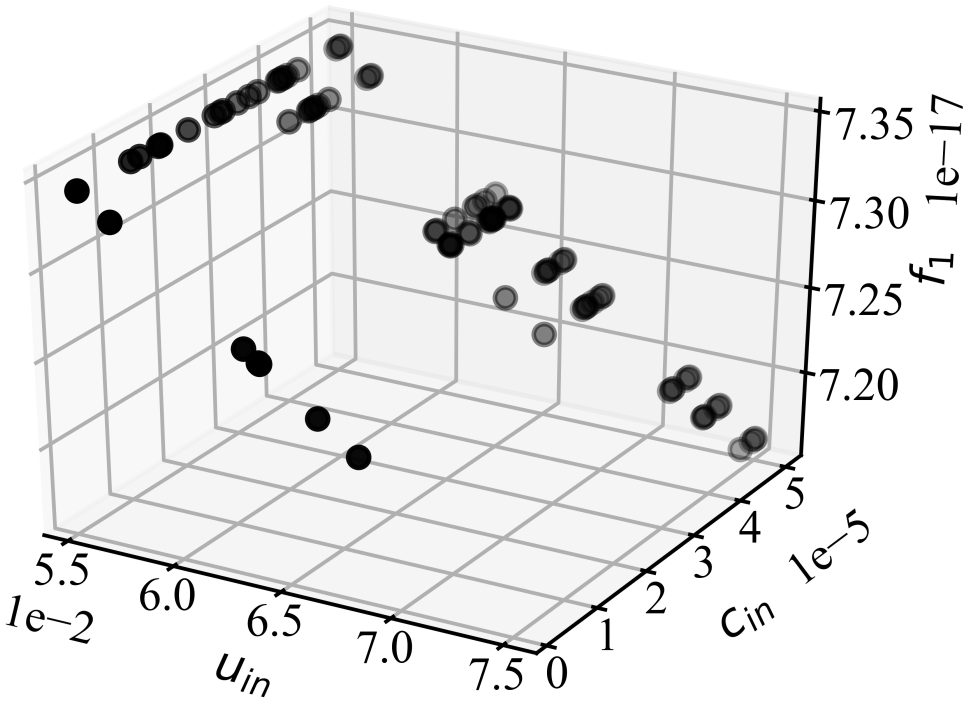

Figure 4.9: Optimum values of f_1 plotted against u_{in} and c_{in}.

and 4.10 that each concentration value in the plot can be paired with the relevant reagent ratio. In Figure 4.9, it is shown that the most yield results in using a ratio proportion of 5%, with decreasing efficacy until 7.5%. Higher c_{in} values are more frequent, although there are some points similarly at the lower c_{in} value range between 5 and 7.5%. u_{mean} has been omitted as the minimum value used in the optimisation was found to be the optimum in all samples on the Pareto front, as it governs residence time. In Figure 4.10, the smaller c_{in} and u_{in} values is where most of optimum f_2 values on the front are clustered, as an increase of both parameters result in different positive and negative correlations. The best results were obtained by using a low flow velocity, and low reagent proportion, in the range $0.05 \leq u_{in} \leq 0.075$.

Limitations The limitations in the method used have been mentioned above but are consolidated here for clarity. There were some regarding the CFD computation, which was completed using first and second order methods, and using the Poisson pressure equation on a finite-difference grid. This is not to discount the merits of using finite

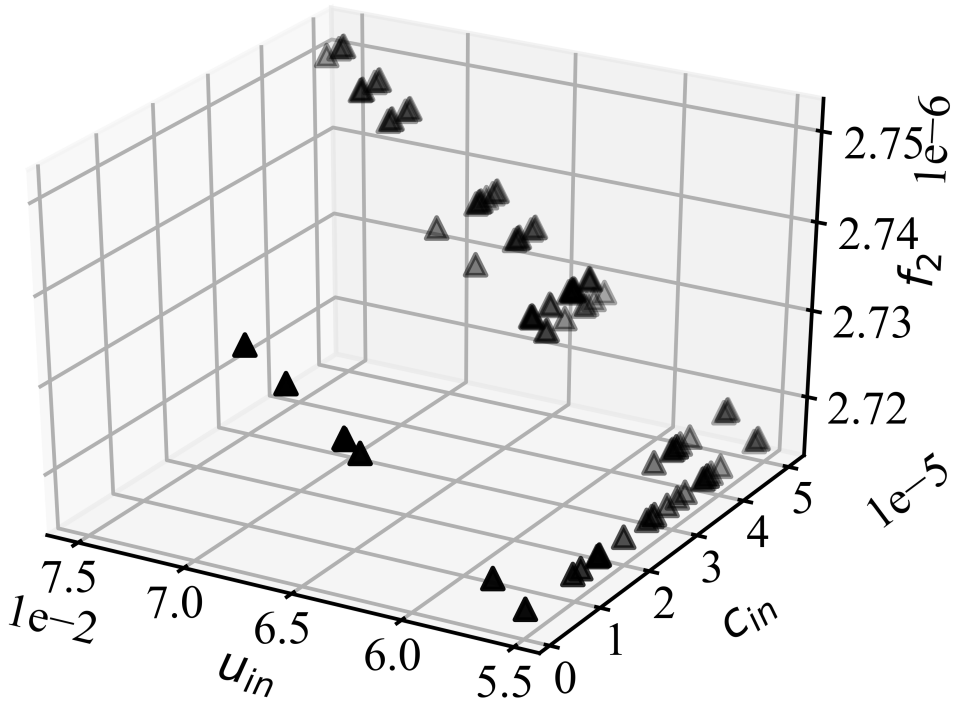

Figure 4.10: Optimum values of f_2 plotted against u_{in} and c_{in}. The axis has been inverted for clarity in displaying the data.

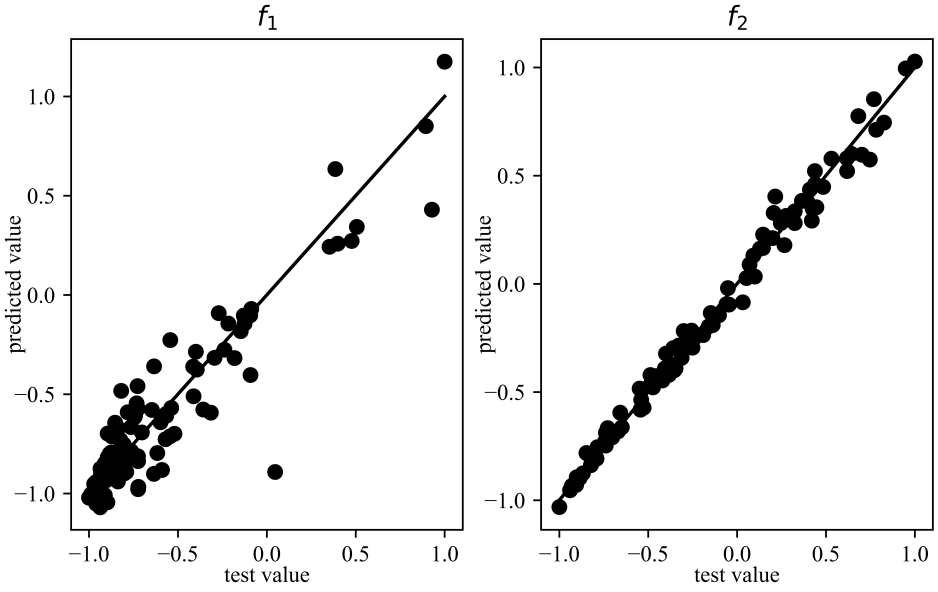

Figure 4.11: Ten-fold cross validation of the surrogate model, used in the multi-objective optimisation, for the order (3,1,1) - corresponding to (u_{in}, c_{in}, u_{mean}).

volume and finite element methods for this problem. There are also some limitations to the accuracy of the surrogate model, but the monitoring of MSE and R^2 between differently ordered models minimised potential inaccuracy, again the cross-validation used to confirm this is visible in Figure 4.11. The left figure shows the cross-validation for f_1, and the right figure f_2. This selection produced the lowest MSE, which was the criterion used for order selection. The scale on the charts is due to minimum-maximum normalisation performed on the dataset before modelling. The aim of this work was to highlight that such a complex problem can be modelled from the derivation of equations using simple assumptions on open-source software, which will become more commonplace to match with the open-source publication model. The probity of open-source allows for interrogation of all underlying components of the system itself, which further complemented the rigour of the academic review process.

4.4 Conclusion

This study looked at using a multiobjective optimisation routine to identify the most efficient way of operating a simple microreactor facilitating a second order reaction. The purpose of this work was to create a numerical model of a Y-junction micromixer, where the variables of the simulation were proportional to the fraction of reagent inflow as total solution flow (u_{in}), the mean flow speed of the solution (u_{mean}) and the concentration of the analyte in the sample (c_{in}). It was found that maximum yield was obtained where $0.05 \leq u_{in} \leq 0.075$, meaning that the sensitivity of the instrument is at its maximum at this range. Not only was sensitivity increased, but also the quantity of reagent being used was in the lower range of values run as part of the optimisation, meaning reduced reagent consumption over the standard operating procedure outlined in Chapter 3. There was no distinct correlation between sample concentration c_{in} and unusued reagent f_2. There is also benefit in reducing the flow rate at which this is operated at, as a slower flow facilitates a longer time for reaction and colour development to occur. An infinitesimal u_{mean} is the optimum value obtained from the optimisation, in that decreasing the flow speed in the channel increases residence time within the mi-

cromixer, to allow for more reaction to occur. Other factors outside of the microreactor, such as mechanical limitation of pumps and operator-based decisions, may determine a minimum rate at which the flow speed can be selected in practice. The results from this study are also of interest more generally in pharmaceuticals [104], prebiotic chemistry [105], nanoparticle production [106], biomedical science and lab-on-a-chip platforms, such as organs-on-chip [14, 107] and micro-total analysis systems [108, 11, 109, 110].

Chapter 5

Wet chemistry

The aim of this chapter is to establish the methods used to prepare reagents and standards used for the Griess and pH indicator reactions. This was required as nitrite standards at low concentrations are unstable, hence fresh standards were frequently produced as required in such concentration ranges. Additionally, behaviour of the sensor in response to turbidity was examined as well as the long-term behaviour of the reaction. Turbidity in environmental water samples results in pseudo-absorbance readings by the photo-detector at all wavelengths. The transient behaviour of the reaction was examined to determine an interval beyond which a sampling frequency is best established. Furthermore, heavy metals can interfere with such reactions. Absorbance spectra were obtained of nitrite standards doped with heavy metals to assess their impact on the absorbance data collected.

Firstly, the reagent and standard preparation methodologies for the Griess reagent and pH indicator were established. Secondly, a mixed 1:1 sample-to-reagent solution was analysed in a UV-Vis spectrometer and the transient absorbance data for both colorimetric methods were collected. Thirdly, turbidity standards were created using primary opalescent solution (measured in FTUs) to determine instrument sensitivity to turbidity. Lastly, 10 ppm standards of iron, copper, zinc and nickel solutions were prepared and the absorbance spectra of each were obtained to assess their impact on data collection.

5.1 Griess test materials preparation

5.1.1 Stock solution

Nitrite standards were required to be produced routinely, as the stability of lower concentrations of nitrite (< 100 ppm) meant that they did not have a long shelf life. This meant that lower concentration standards needed to be freshly prepared for daily use. A stock solution was prepared of 1000 ppm, from which standards were diluted as required. To further increase shelf life, the stock solution was separated into $100\,\mathrm{ml}$ containers and stored frozen. Sodium nitrite ($NaNO_2$) (ACS reagent, $\leq 97.0\%$) from Sigma Aldrich was used to create the nitrite standard. This was diluted with deionised water from T.E. Laboratories. As $NaNO_2$ has a molar mass of $69.00\,\mathrm{g\,mol^{-1}}$, and that of nitrite is $46.0055\,\mathrm{g\,mol^{-1}}$, the amount of $NaNO_2$ required to produce a $1\,\mathrm{L}$ 1000 ppm solution was $1.4998\,\mathrm{g}$. This was measured using an analytical balance to ensure sub-milligram accuracy.

The measured quantity of $NaNO_2$ was then carefully placed from a weighing boat into a $1\,\mathrm{L}$ volumetric flask. Deionised water was then added until the meniscus of the liquid reached the $1\,\mathrm{L}$ marker. The flask was manually mixed through repeated upending to ensure that all of the $NaNO_2$ was fully dissolved. Dilutions were then made from this using a micropipette (Sartorius, Germany) to ensure accuracy in the dilution. To make a 1 ppm solution, $1\,\mathrm{ml}$ of stock solution was diluted to $1\,\mathrm{L}$.

5.1.2 Reagent

The reagent was prepared using naphtylethylenediamine (NEDD), sulfanilamide, and hydrochloric acid (HCl). Measured using an analytical balance, $5\,\mathrm{g}$ of NEDD and $0.5\,\mathrm{g}$ of sulfanilamide were added to a volumetric flask, as well as $5\,\mathrm{ml}$ of 37% HCl and $100\,\mathrm{ml}$ of DI water. This was mixed in the same manner as in Section 5.1.1 before further diluting with DI water to $500\,\mathrm{ml}$.

Table 5.1: Formulation of optimised reagent. Components include phenol red (PR), chlorophenol red (CPR) and bromophenol blue (BPB).

Component	Molar mass (g/mol)	Mole fraction	mg per $1\,\mathrm{L}$
PR	354.38	0.46	3.3
CPR	423.27	0.25	2.1
BPB	669.97	0.29	3.9

5.2 pH indicator materials preparation

The pH indicator was prepared using an optimised formulation [111] of phenol red (PR), chlorophenol red (CPR) and bromophenol blue (BPB). Each component has a narrow pH range, however their combination can result in a wide pH range being covered, which has absorption peaks at $430\,\mathrm{nm}$ and $575\,\mathrm{nm}$, graphically represented in Figure 5.1. The second mode is of interest for this research as this is close to the $525\,\mathrm{nm}$ wavelength the Griess test was conducted at. The optimisation has previously been conducted by Raghuraman et al. [111], and shown that for a total dye solution, provided as a concentration of $2 \times 10^{-5}\,\mathrm{mol\,kg^{-1}}$ in pure water, that the proportion of each component in the total solution for (PR,CPR,BPB) is (0.46,0.25,0.29). The full range of properties is presented in Table 5.1.

To produce a reagent which contained a total dye concentration of $2 \times 10^{-5}\,\mathrm{mol\,kg^{-1}}$, for $1\,\mathrm{kg}$ water, the masses of PR, CPR and BPB which needed to be added are in Table 5.1. As before, the powders were measured using an analytical balance. The indicators were added to a $1\,\mathrm{L}$ volumetric flask, then $100\,\mathrm{ml}$ of water was added to dilute the solution. The flask was manually mixed to ensure even mixing, then fully diluted to $1\,\mathrm{L}$.

5.2.1 Calibration curve

The calibration curve was constructed using each of the pH buffers available – ranging from pH 4-10 inclusive, all produced by T.E. Laboratories. The solutions were left to stand for 10 minutes to allow for complete colour development. The absorbance was obtained from each sample at $525\,\mathrm{nm}$ and $570\,\mathrm{nm}$. The obtained calibration curve (or surface) is shown in Figure 5.2. These were obtained from a UV-Vis spectrometer at

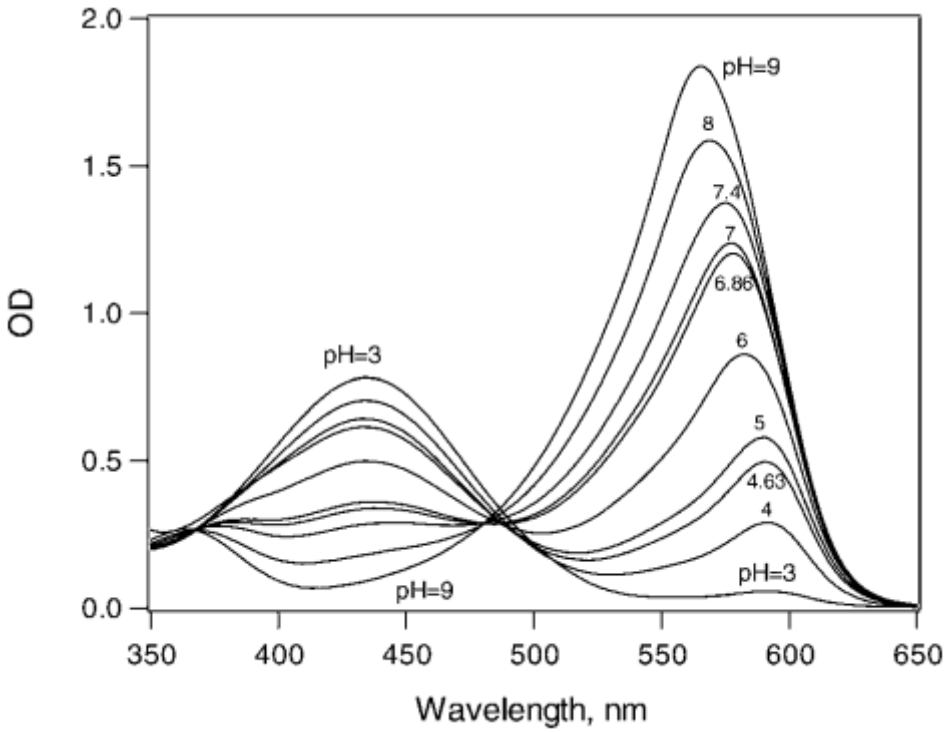

Figure 5.1: Absorption response across the visible range from pH 4-10. The peaks are at $430\,\mathrm{nm}$ and $575\,\mathrm{nm}$. Image reproduced from [111].

$550\,\mathrm{nm}$. The standard error is derived from the resolution of the spectrometer.

5.3 Steady-state study

The steady-state study was important as it was there to provide a two-dimensional calibration curve, which was used to assess if for the Griess reaction that different amounts of reagent and standard had an effect on the colour development that took place. This builds upon the computational modelling detailed in Chapter 4 as the long-term behaviour of the reaction will incorporate more random elements with increased time. It was anticipated that there may have been excess reagent used in the 1:1 ratio, so this work was done to see if there was any significant effect in the yield when the reagent quantity used was reduced.

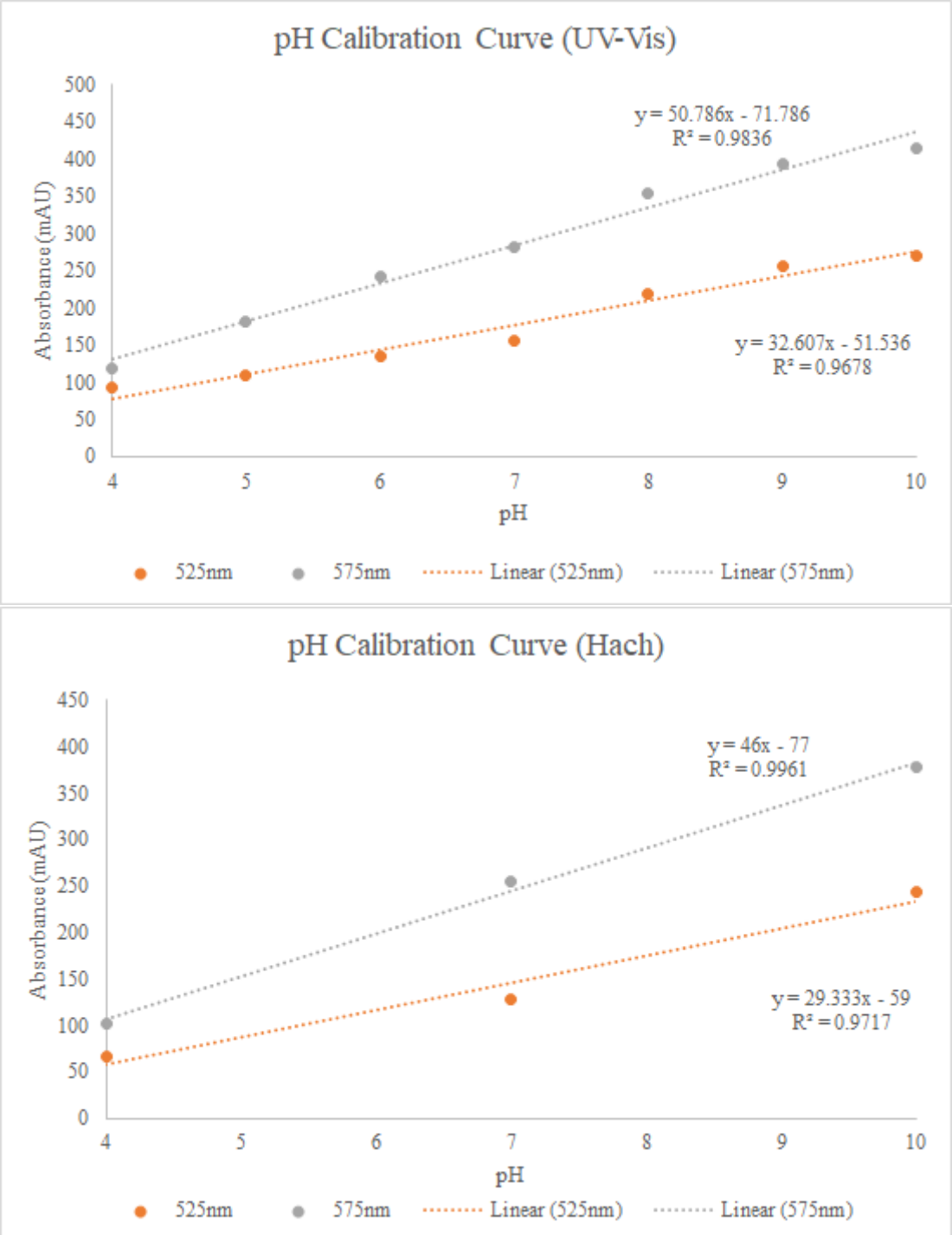

Figure 5.2: Calibration curve for a range of pH buffers.

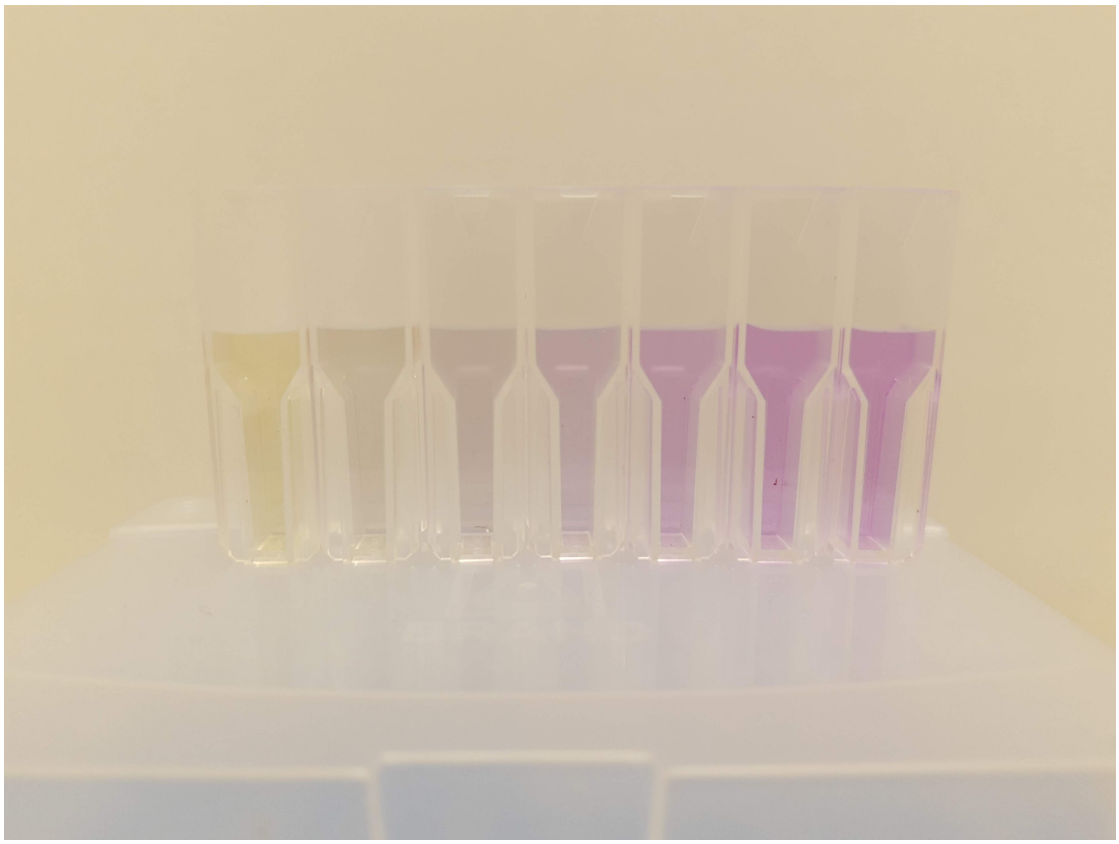

Figure 5.3: Image of the solutions with full colour development, from pH 4-10, left to right.

5.3.1 Nitrite

Method

The concentrations of nitrite standards used were the following: $0.01\,\mathrm{mg\,L^{-1}}$, $0.025\,\mathrm{mg\,L^{-1}}$, $0.05\,\mathrm{mg\,L^{-1}}$, $0.075\,\mathrm{mg\,L^{-1}}$, $0.1\,\mathrm{mg\,L^{-1}}$, $0.2\,\mathrm{mg\,L^{-1}}$, $0.4\,\mathrm{mg\,L^{-1}}$, $0.6\,\mathrm{mg\,L^{-1}}$, $0.8\,\mathrm{mg\,L^{-1}}$ and $1.0\,\mathrm{mg\,L^{-1}}$. The proportion of reagent used varied from 0.1 (10% reagent in total solution) to 0.5. A stock solution of 1 ppm was prepared. From this, the above nitrite concentration standards were made through dilution in $1500\,\mu\mathrm{l}$ containers. Following this, the remainder of the $1500\,\mu\mathrm{l}$ solution was made up of the reagent in each cuvette. The cuvettes were left to rest for one hour. A UV-VIS spectrometer (Unicam) at $525\,\mathrm{nm}$ and $575\,\mathrm{nm}$ was used afterwards to record the absorbance and hence the yield of the colorimetric complex.

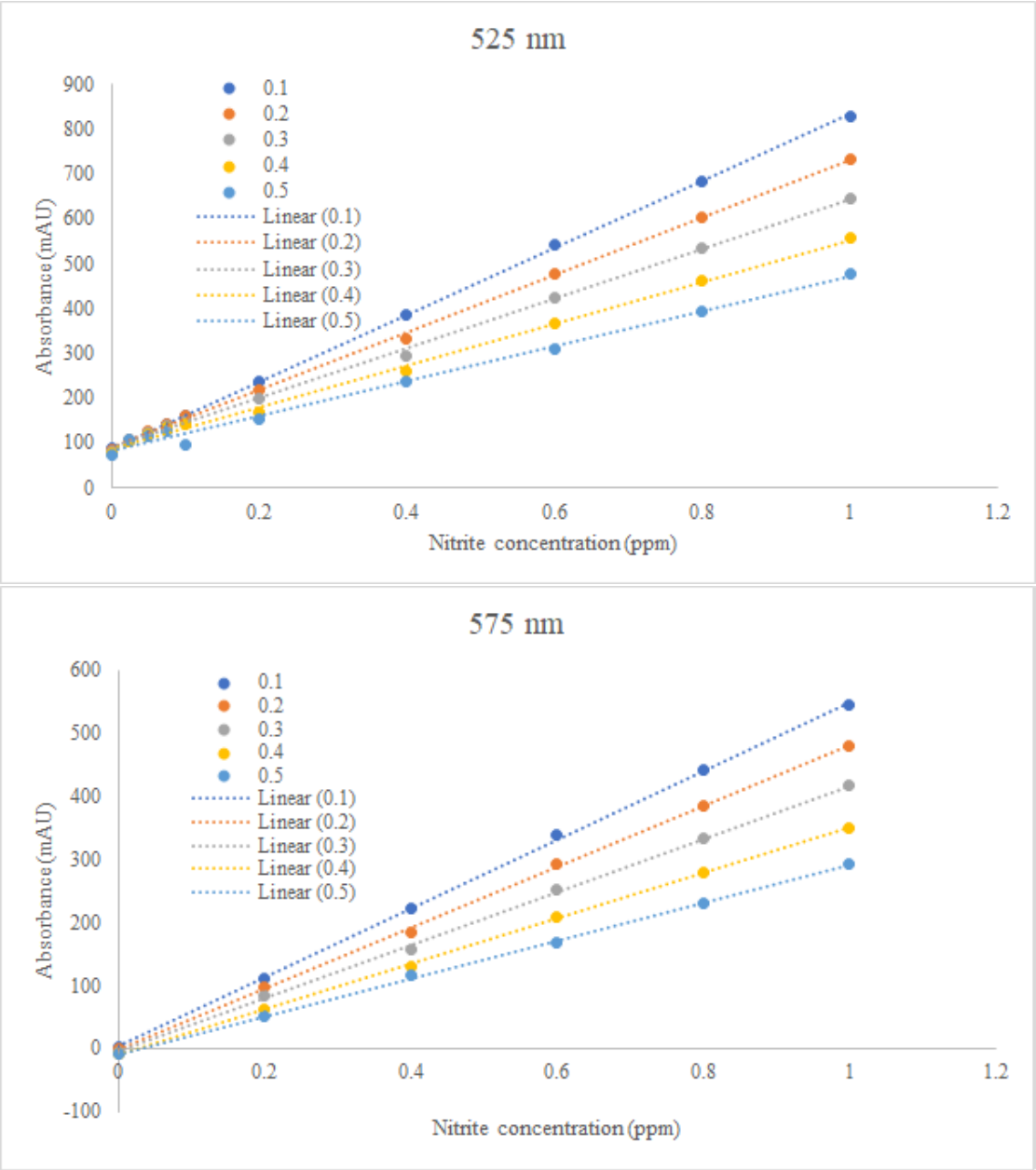

Figure 5.4: Calibration curves of the absorbance readings for nitrite for each u_{in} value at $525\,\mathrm{nm}$ and $575\,\mathrm{nm}$.

Result

It was found that more colorimetric complex was developed when the ratio of reagent to sample is more skewed towards the reagent. The reason why this is thought to occur is because for more balanced ratios, there is a saturation of reagent, meaning that there is less reactant present for the colorimetric complex to be formed. The one hour standing time eliminated lack of mixing or colour development as a reason for the differences.

Long term transient study

To show that the Griess reaction occurs over a long period of time and to exclude some noisy effects that were witnessed in the sensor chromatograms, a standard of $0.25\,\mathrm{mg\,L^{-1}}$ nitrite at the same sample-to-reagent ratio (2:1), was placed in a micro-cuvette and in a UV-Vis spectrometer. The colour was allowed to develop for 30 minutes. The result of this is visible in Figure 5.5. It can be seen that beyond the 5 minutes typically used to allow colour to develop, there is still colour development up to 117 mAU. A noise pattern is visible in the chart. Beyond this, a couple of hours later, the absorbance was recorded at 0.202 AU. Noise is present, although the effect is not as visible in as the sensor chromatograms, as the path length is reduced ($1\,\mathrm{cm}$ vs. $2\,\mathrm{cm}$). In many analytical approaches set times are used to determine the concentration as it can be seen that in the near term, and using more distant times, that the same sample can produce multiple readings. Therefore, it was important to model the most basic underlying chemistry happening to ignore and mitigate the other effects. Some standards were also run. The chromatograms are overlaid in Figure 6.13. The concentrations used were $0.25\,\mathrm{mg\,L^{-1}}$, $0.5\,\mathrm{mg\,L^{-1}}$ and $0.75\,\mathrm{mg\,L^{-1}}$. This corresponds to absorbances of 0.9658(0.0394), 1.2878(0.036) and 1.4830(0.0381).

5.3.2 pH indicator

This test was also performed with the pH indicator test. The colour change for this pH range is shown in Figure 5.3. The leftmost cuvette contains a pH buffer solution of 4, increasing up until 10 in the rightmost cuvette. When using rate mode on the UV-Vis

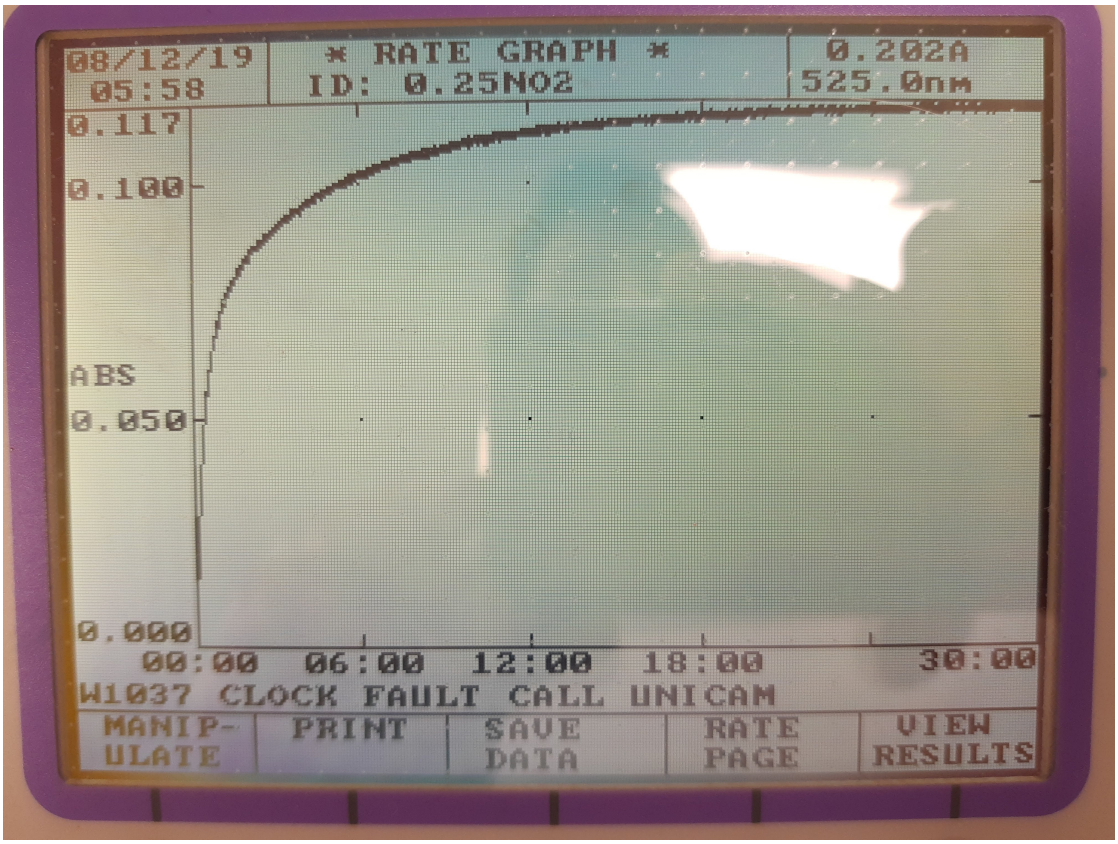

Figure 5.5: Absorbance vs time plot for the Griess test, where $0.25\,\mathrm{mg\,L^{-1}}$ nitrite was tested, at a sample-to-reagent ratio of 2:1.

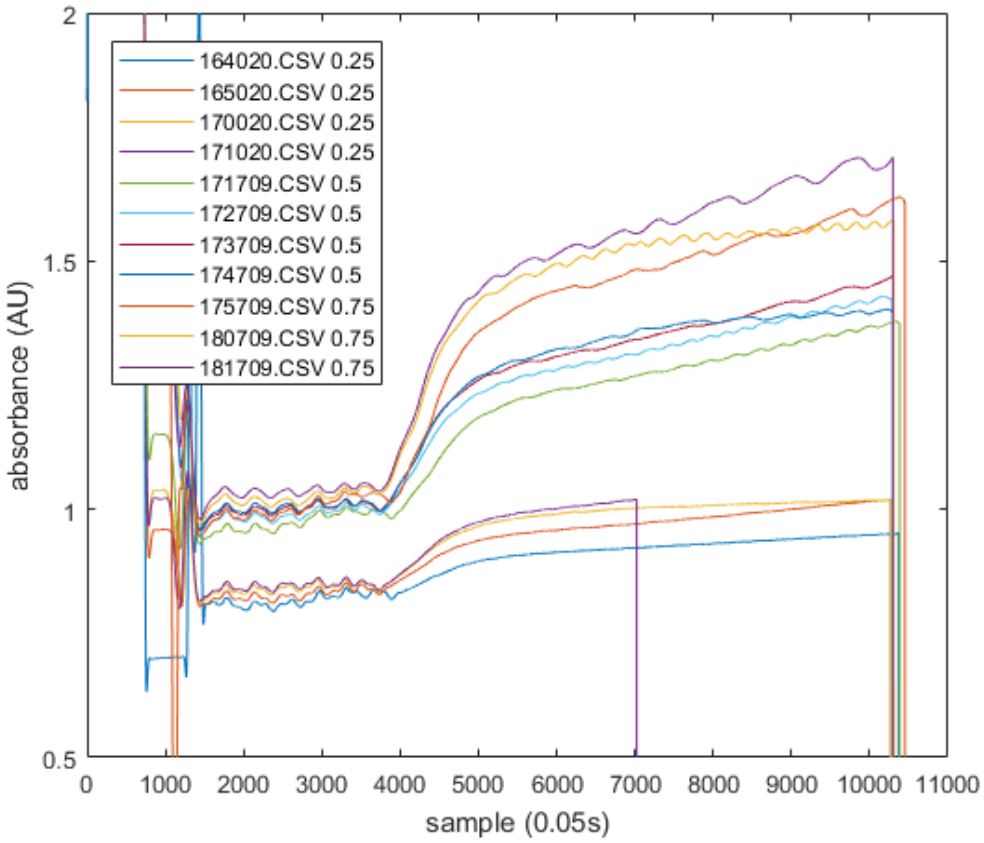

Figure 5.6: Nitrite standards sequentially run, as marked in the legend.

spectrometer, the reaction was too fast to be captured by the device, as absorbance did not change from the initial recorded absorbance value. The reaction was sufficiently fast such that it could be assumed to be instantaneous.

5.4 Turbidity study

It was initially intended to use environmental water to test for turbidity. As turbidity varies on the composition of soluble particles and their size, it was decided that, for consistency, turbidity would be simulated using a primary opalescent solution, composed of methenamine and hydrazinium sulfate (Reagecon Diagnostics, Ireland). Its white cloudy appearance is due to Mie scattering, meaning that absorbance was the same for all wavelengths. For the purposes of this research, turbidity was measured using absorbance techniques similar to above in formazin turbidity units (FTU). A $50\,\mathrm{ml}$ sample of 1000 FTU was collected and diluted to vary turbidity e.g. a 20 FTU solution was created with a 49:1 dilution.

5.4.1 Calibration curve

The calibration curve in Figure 5.7 was obtained using the Unicam UV-Vis spectrometer, as well as the on-chip calibration in Figure 5.8. From the 3 calibrations curves produced, the sensitivity of the instrument is shown to be approximately 2.4 mAU/FTU. The absorbance for low turbidity values was negligible, only changing to 10^2 mAU where turbidity ≥ 100 FTU. It is only near 50 FTU where there is an appreciable 100 mAU which would be detectable outside of any noise.

5.5 Interference study

To confirm that the effect of the metals was due to inference with the reaction as opposed to an absorbance effect due to their own presence, the absorbance spectra of water samples doped with 10 ppm of each metal were obtained. A sample of each of

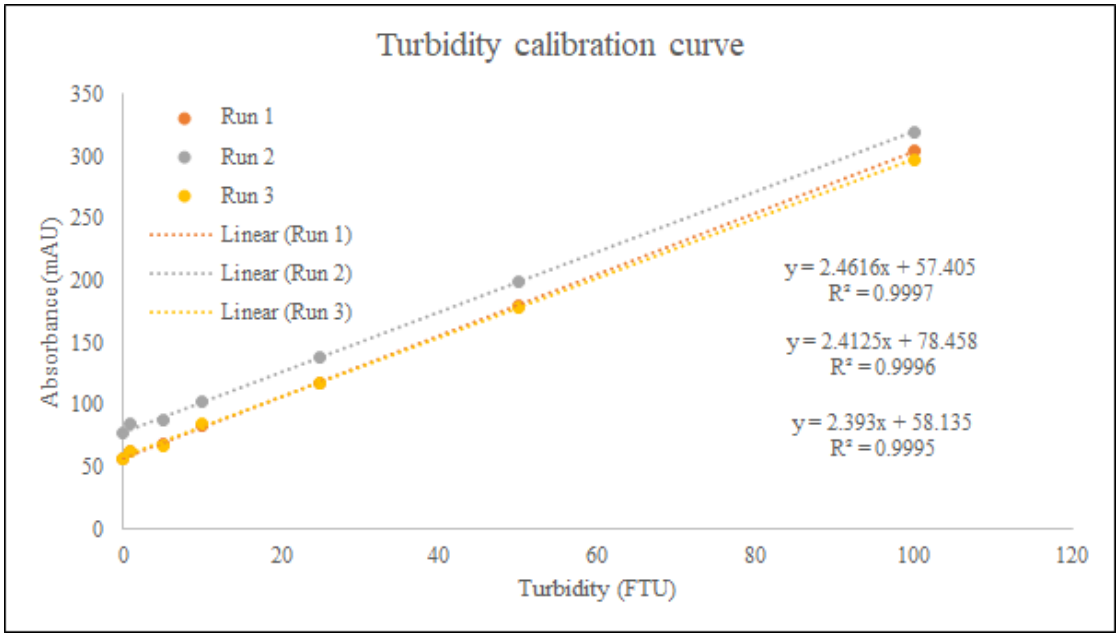

Figure 5.7: Turbidity calibration curve obtained using Unicam UV-Vis spectrometer.

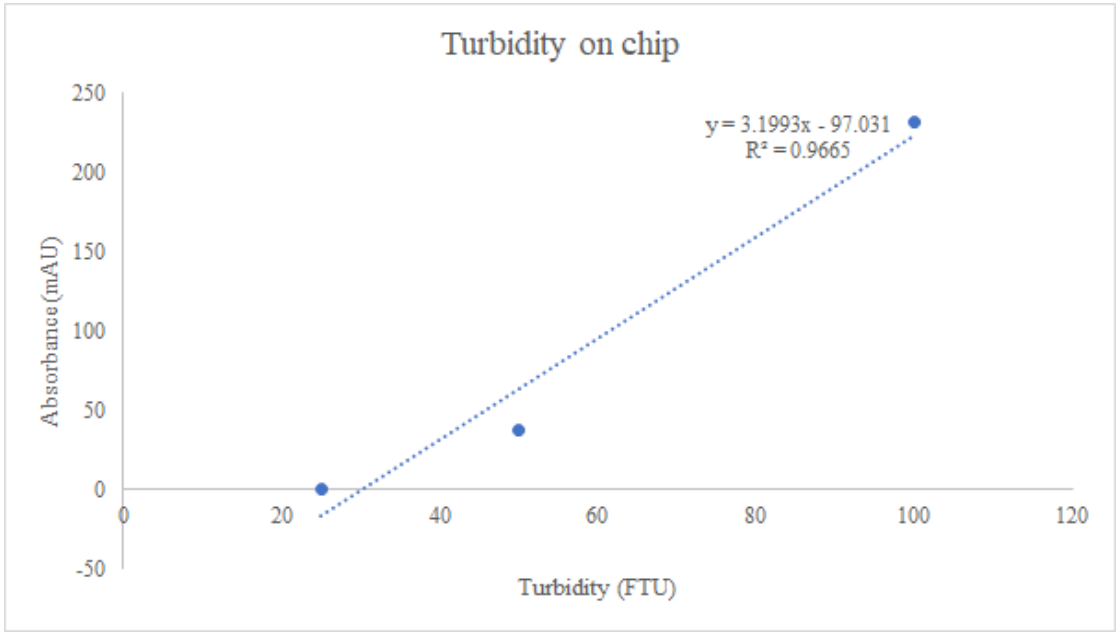

Figure 5.8: Turbidity calibration curve obtained using the colorimetric Aquamonitrix.

the interferants in the absence of reagent and nitrite were placed into micro-cuvettes and analysed using UV-Vis spectroscopy in the range between $400\,\mathrm{nm}$ and $600\,\mathrm{nm}$. A visual inspection of the curves was performed to identify prominent variations.

The results of this show that there are negligible differences upon visual inspection between a blank sample and samples doped with iron, copper, zinc and nickel. (Figure 5.9). In concentrations on a similar scale to those in environmental waters, there is no discernible difference between these spectra. Therefore, further numerical analysis was not conducted. It can be concluded from this that any effect of metals in the Griess reaction was due to their interfering with the reaction as opposed to having their own absorbance at that wavelength superimposed on the spectrum.

5.6 Conclusion

A robust methodology for standard and reagent preparation was established. The UV-Vis spectrometer did not record absorbance for turbidity standards below 50 FTU. Sensitivity to turbidity was much lower than to the Griess reaction. Hence, turbidity was a negligible factor in absorbance readings. The transient behaviour of the Griess reaction showed that the rate of reaction slowed greatly after 15 minutes. The pH indicator was an instanteous reaction, therefore there was no transient behaviour. The interference study showed a negligible effect of heavy metals on the absorbance spectra of nitrite standards, indicating that any altered absorbance due to heavy metal effect on the reaction rather than themselves absorbing light.

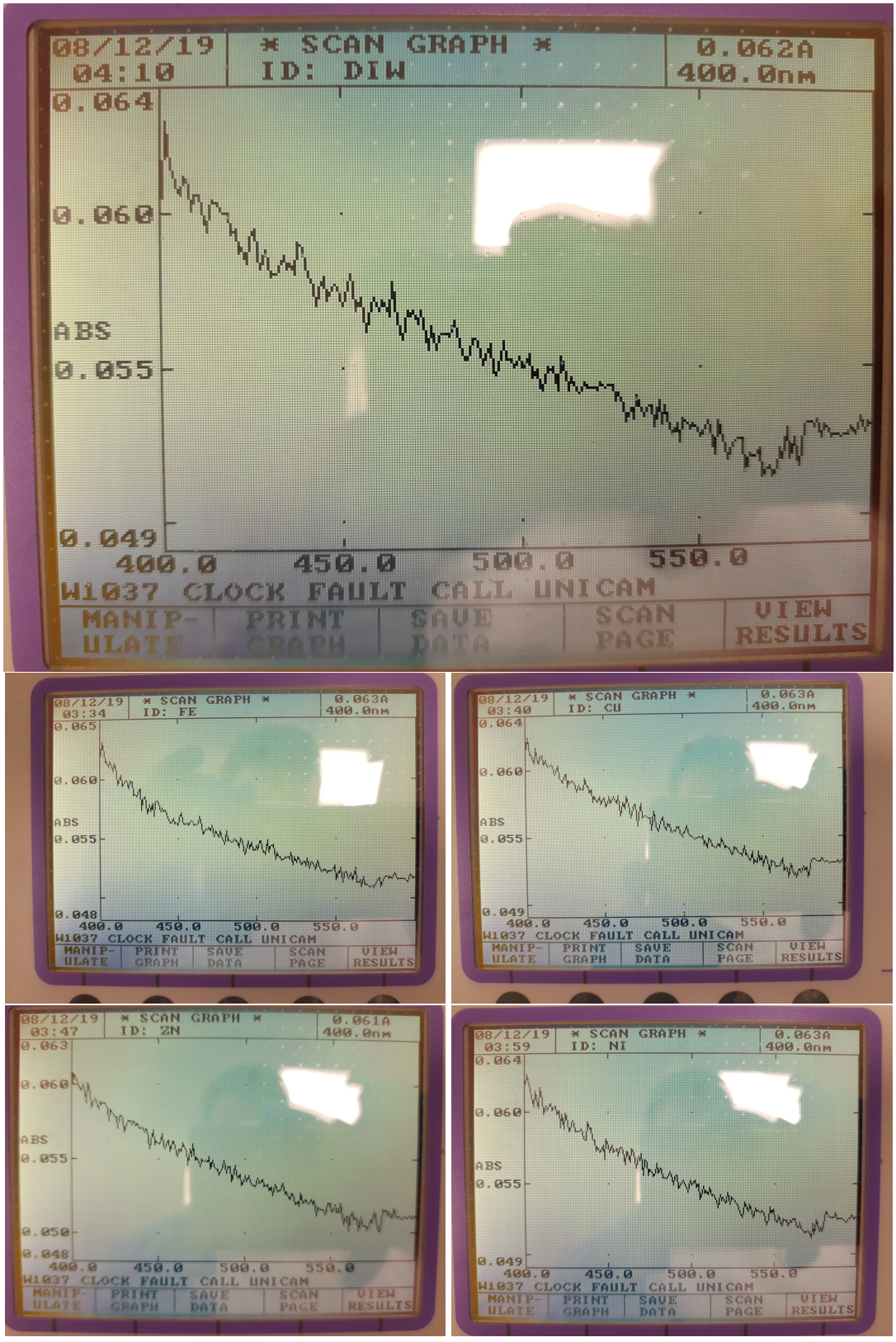

Figure 5.9: Absorbance spectrum of the 10 ppm standards for each of (clockwise from the top left) iron, copper, nickel and zinc, with the DI water used to make each standard on top.

Chapter 6

DBM modelling

The aim of this chapter is to identify mechanistic models of the colorimetric reactor response of the sensor. There are two stages of interest. These are the flow data, where data is collected while the syringes are operating, and the stopped flow data, where the syringes have fully emptied. Due to the limitations of the photodetector channel, only numerical data is used for the analysis of flow data. Firstly, a derivation of intuitive mechanical models is completed. Secondly, system identification of the numerical data is performed, and parameterisation of the coefficients from the data-based models are performed to reduce dimensionality. Thirdly, the experimental data are preprocessed and a model structure that can be used for multiple concentrations and flow ratios is identified.

6.1 Introduction

Data-based mechanistic (DBM) modeling is a data-driven modelling approach where the model structure and coefficients are first estimated from existing input and output data, before applying mechanistic principles to the identified system. The derivation of a meaningful model from data is completed by first identifying a model structure and coefficients using an instrumental variable method. Then, applying mechanistic principles to the estimated model, otherwise unobservable modes can be identified, which can be used to simplify the model while retaining system behaviour. There are many

methods which permit model estimation of a system, including recursive instrumental variable (RIV) and simplified recursive instrumental variable (SRIV) methods.

6.2 Mechanistic modelling

6.2.1 Convection model

A transfer function is required to have real zeroes and poles for it to have a meaningful real-world intepretation. The physics governing convection and diffusive flows are extensively described in Chapters 2 and 4. For a simple one-dimensional microreactor, with a large Pe, a mechanistic model can be derived as below, using Equation (6.1).

$$c = \frac{\frac{u_{mean}}{dz}}{s + \frac{u_{mean}}{dz}} u\left(t - \tau\right) \tag{6.1}$$

where $u(t-\tau)$ is the input concentration at the inlet with time delay τ. To extend this to a first order reacting convection mechanistic model, assuming evenly distributed reactant concentration c_1 and non-consumed reagent throughout the mixture, the model derived to calculate product concentration c_2 combining both Equations (6.2) and (6.3):

$$c_1 = \frac{\frac{u_{mean}}{dz}}{s + \frac{u_{mean}}{dz} + k} u(t - \tau) \tag{6.2}$$

$$c_2 = \frac{k}{s + \frac{u_{mean}}{dz}} c_1 \tag{6.3}$$

provides the resulting model as per Equation (6.4):

$$c_2 = \frac{k\frac{u_{mean}}{dz}}{(s + \frac{u_{mean}}{dz} + k)(s + \frac{u_{mean}}{dz})} u(t - \tau) \tag{6.4}$$

The above form suggest 2 modes, one convective term and a second convective term modified by the reaction rate constant. The diffusion is neglected in this case, but this can be accounted for with either the inclusion of this term from Equation (6.1). Equation (6.4) be separated into 2 parallel transfer functions using partial fraction expansion

into:

$$c_2 = \left(\frac{\frac{u_{mean}}{dz}}{s + \frac{u_{mean}}{dz}} - \frac{\frac{u_{mean}}{dz}}{s + k + \frac{u_{mean}}{dz}} \right) u(t - \tau) \tag{6.5}$$

If rearranged such that the gains and poles are more visible, the below is obtained:

$$c_2 = \left(\frac{1}{\frac{1}{\frac{u_{mean}}{dz}} s + 1} - \frac{1 - \frac{k}{k + \frac{u_{mean}}{dz}}}{\frac{1}{k + \frac{u_{mean}}{dz}} s + 1} \right) u(t - \tau) \tag{6.6}$$

Discussion

The above model provided an initial expectation of the model to be expected following model estimation of expertimental data. The gain should be real-valued between 0 and 1 (less product than reactant), and the poles real-valued also, which is present in Equation (6.6). The first component acts as a purely convective component for the reactant, as if there is no reaction taking place. The second term accounts for the reactive flow, and a faster reaction rate k intuitively decreasing the gain and natural mode. As this is subtracted from the first component, this results in more yield. If $k >> \frac{u_{mean}}{dz}$, then reaction fully occurs. Conversely, if $k << \frac{u_{mean}}{dz}$, then there is no yield.However, one issue with the pole is that the residence time, based on the convection time constant, is not fully applicable to the product, for which it would vary along the channel width, due a parabolic flow profile which is not accounted for in this simplified model. Additionally, it was possible that there were some oscillatory components which cropped up as a result of the STF modelling. Using partial fraction expansion, it was found that for one of the data sets, there was one real root and two pairs of complex conjugate roots, which do not have an immediate mechanistic interpretation. By reducing the conjugate pair complex transfer functions to a second order transfer function with real-valued coefficients, and leaving the real-rooted components as was, the outputs of each part were plotted. On occasion, there was an imaginary component to the output, however this was negligible (10^{-13}) on multiple orders of magnitude, so this was neglected. The imaginary component originated for roots to account for the curved ramp-up of the curve, which then tapers to a maximum slope, before receding into a slowing of the curve, which

overall represents a ramp-up to a steady-state output.

6.2.2 Semi-discrete advection model

The previous model described is a simple two-point model, rather than a chain of discrete channel lengths. To improve on the accuracy of that model, the step was then taken to construct a model based on the same governing equations applied to a series of n transfer functions. This model was based on the semi-discrete advection dead-zone used by Young [112] in modelling water transport through wetlands. This model, in contrast to the river system, is an enclosed microfluidic system in which the flow is dominated with characteristics associated with low Reynolds number and high Peclet number. The flow was approximated to having a large Pe, meaning negligible axial diffusion, thus mixing can only be attributed to perpendicular diffusive flows in the absense of passive mixers. The presence of backflow was neglected, as this is attributed to phenomena such as tidal effects, which is not the case in the syringe pump setup under consideration in this research, as per Chapter 3. Therefore this factor was set to $G_d = 0$.

If the diffusive effects in the lateral position are ignored, and channel length is discretised, Equation (2.1) becomes:

$$\frac{\partial c}{\partial t} = -\frac{u_{mean}}{dz}(c_i - c_{i-1}) \tag{6.7}$$

where c_i is the concentration at node i of n nodes, and c_{i-1} is an upsteam node. Upon a Laplace transform:

$$(s + \frac{u_{mean}}{dz})c = \frac{u_{mean}}{dz}(c_{i-1}) \tag{6.8}$$

If the term $U/dz = 1/T$ are aggregated, then this can be reduced to, in a similar fashion to:

$$c = \frac{1}{1 + Ts}c_{i-1} \tag{6.9}$$

To generalise with a conservative effect, then the above equation can be expressed

with a gain term G, in which any value below or above one represents an increase or decrease respectively. The transfer function can be multiplied by a gain coefficient G, generalising the above to:

$$c = \frac{G}{1 + Ts} c_{i-1} \tag{6.10}$$

To change the representation from transfer functions to state space, Equation (6.7) can be revised to include the G and $1/T$ terms to obtain:

$$\frac{\partial c}{\partial t} = \frac{G}{T} c_{i-1} - \frac{G}{T} \tag{6.11}$$

For a state-space representation of any node i:

$$\begin{pmatrix} \frac{\partial c}{\partial t}_{i-1} \\ \frac{\partial c}{\partial t}_{i} \end{pmatrix} = \begin{pmatrix} -\frac{G}{T} & 0 \\ \frac{G}{T} & -\frac{G}{T} \end{pmatrix} \begin{pmatrix} c_i \\ c_{i-1} \end{pmatrix} \tag{6.12}$$

The state space matrices can be extended to include all n nodes, producing an $n \times n$ state matrix. The input into the model is $u(t - \tau) = c_0$, where τ is a pure convective time lag. The state space equation takes the form:

$$\begin{pmatrix} \frac{\partial c}{\partial t}_{1} \\ \frac{\partial c}{\partial t}_{2} \\ \vdots \\ \frac{\partial c}{\partial t}_{n-1} \\ \frac{\partial c}{\partial t}_{n} \end{pmatrix} = \begin{pmatrix} -\frac{G}{T} & & & & \\ \frac{G}{T} & \ddots & & & \\ & \ddots & \ddots & & \\ & & \ddots & \ddots & \\ & & & \frac{G}{T} & -\frac{G}{T} \end{pmatrix} \begin{pmatrix} c_1 \\ c_2 \\ \vdots \\ c_{n-1} \\ c_n \end{pmatrix} + \begin{pmatrix} \frac{G}{T} \\ \\ \\ \\ \end{pmatrix} u(t - \tau) \tag{6.13}$$

Where the output $y = c_n$, denoted an output matrix of $(0 \ldots 1)$ with no feedthrough.

If the chosen length of the system is chosen to be Z = $30\,\mathrm{cm}$ (the length of flow between the sensor syringes and the photodetector channel), u_{mean} = $92.59\,\mathrm{mm\,s^{-1}}$ (based on a cross sectional area of $0.09\,\mathrm{mm^2}$ and flow rate of $8.33\,\mathrm{mm^3\,s^{-1}}$). This is characterised by a $Re = 27.78$.

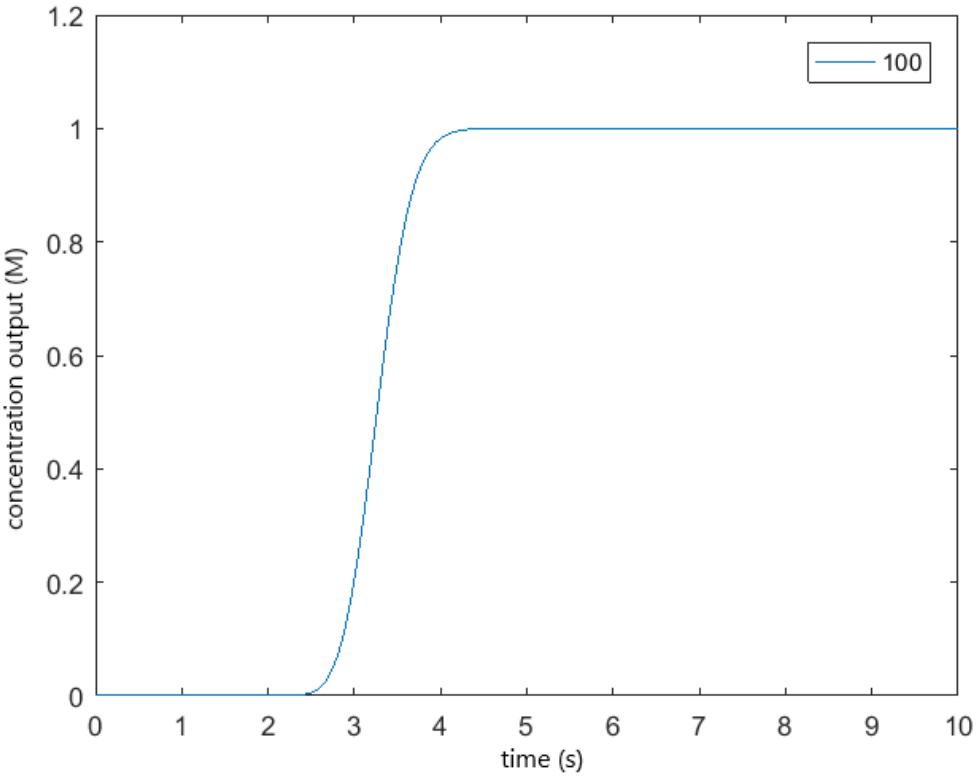

Figure 6.1: Step response for the model outlined in Section 6.2.2.

An example output of Equation (6.13) is shown in Figure 6.1, in which and $n = 100$, and $G = 1$. It can be seen that the lag time is roughly $\tau \approx 2.5\,\mathrm{s}$.

6.2.3 Reactive flow

The reactive flow model included 2 species in the reactor: the reactant $c_{1,i}$ at node i and product $c_{2,i}$ at node i. It was assumed that the initial model has instantaneous mixing upon entering the microreactor. The reaction was a first order irreversible reaction, with reaction rate k. If the equation is taken from above, we can add the reactive term $kc_{1,i}$:

$$\frac{\partial c_{1,i}}{\partial t} = \frac{u_{mean}}{dz}(c_{1,i-1} - c_{1,i}) - kc_{1,i} \tag{6.14}$$

This can be put into the form $c_{1,i} = \frac{G}{1+Ts}c_{1,i-1}$, where the gain G is now

$$G = \frac{\frac{u_{mean}}{dz}}{\frac{u_{mean}}{dz} + k} \tag{6.15}$$

And the new time constant $T = (\frac{u_{mean}}{dz} + k)^{-1}$, where:

$$\frac{\partial c_{1,i}}{\partial t} = -\frac{1}{T}c_{1,i} + \frac{G}{T}c_{1,i-1} \tag{6.16}$$

The equation for the product is similar but includes the reactant in its term.

$$\frac{\partial c_{2,i}}{\partial t} = \frac{u_{mean}}{dz}c_{2,i-1} - c_{2,i} + kc_{1,i} \tag{6.17}$$

$$\frac{\partial c_{2,i}}{\partial t} = \frac{u_{mean}}{dz}c_{2,i-1} - \frac{u_{mean}}{dz}c_{2,i} + kc_{1,i} \tag{6.18}$$

Equations (6.16) and (6.18) can be put into the state space form:

$$\begin{pmatrix} \frac{\partial c_{i-1}^1}{\partial t} \\ \frac{\partial c_i^1}{\partial t} \\ \frac{\partial c_{i-1}^2}{\partial t} \\ \frac{\partial c_i^2}{\partial t} \end{pmatrix} = \left(\begin{array}{cc|cc} -\frac{1}{T} & 0 & 0 & 0 \\ \frac{G}{T} & -\frac{1}{T} & 0 & 0 \\ \hline k & 0 & -\frac{u_{mean}}{dz} & 0 \\ 0 & k & \frac{u_{mean}}{dz} & -\frac{u_{mean}}{dz} \end{array}\right) \begin{pmatrix} c_{i-1}^1 \\ c_i^1 \\ c_{i-1}^2 \\ c_i^2 \end{pmatrix} + \left(\begin{array}{c} \frac{G}{T} \\ 0 \\ \hline 0 \\ 0 \end{array}\right) u(t-\tau) \tag{6.19}$$

Model response

The system was extended to n components to incorpotare all nodes, with separation dz as before. A test was run intially for a fixed velocity and reaction rate to determine when there were enoguh nodes in the model. The state space from Equation (6.19) was extended to the same n elements. It was found that there was a maximum of $n = 50$ in the reactive case suitable for modelling before there were divergence issues.

The time lag is intuitive to identify visually from this chart, which is approximately Z/u_{mean}, which was used as a rough estimate for τ in system identification as a time delay. The model reduction was then performed for $(55\tau; 1515\tau)$. The best Young Information Criterion (YIC) and R_t^2 values are shown in Table 6.1.

Table 6.1: Results of system identification `rivbjid` using data generated from the semi-discrete model.

n	m	δ	YIC	R_t^2	BIC	AIC
9	10	647	-33.5126	1	-54746.5184	-29.8706
10	11	647	-31.8869	1	-57439.8676	-31.2222
5	6	647	-28.485	1	-44678.8115	-24.8169
7	8	647	-27.6155	1	-45851.9851	-25.4143
8	9	647	-27.3705	1	-49115.329	-27.0508
6	7	647	-17.9287	1	-44737.5296	-24.8518
9	9	647	-16.7722	0.999572	-18801.2094	-11.9041
7	7	647	-15.4584	0.999572	-18831.4895	-11.9081
11	11	647	-14.3046	0.999572	-18770.7892	-11.9001
7	6	647	-6.4494	0.998213	-15981.2886	-10.4809
15	11	647	-5.9135	0.999222	-17545.657	-11.2991
9	8	647	-5.7319	0.999201	-17561.5754	-11.2818
5	5	647	-4.4995	0.750913	-6124.4153	-5.5465
13	8	647	-0.5428	0.998376	-16111.3971	-10.5683
11	8	647	-0.4366	0.999149	-17418.8134	-11.2161
13	9	647	-0.4351	0.998099	-15788.6845	-10.4098
13	11	647	1.1918	0.999469	-18325.1219	-11.683
11	6	647	1.8213	0.999276	-17757.2526	-11.3796
7	5	647	2.7357	0.654464	-5454.297	-5.2172

6.3 System identification using CFD data

A data set was generated using the CFD simulation methods from Chapter 4. This data set was then analysed to see what type of real transfer function model could be identifed and produced to reasonably characterise the output of the microreactor to be simulated, and, by extension, the real response of the sensor. The output of the sensor

when operating in flow mode (from zero initial conditions) was a ramp-up (during the flushing of the residue fluid) which reached a steady state after full flushing. This reflects that once the flow has stabilised and full dispersion within the reactor has taken place, the rate of production is countered by the volume of flushing. The below was used to identify a model structure for this behaviour.

6.3.1 Data sample for system identification

The data set (Figure 6.2) was made of 100 simulation outputs, recording the input values chosen by Latin hypercube sampling used to generate these. The flow data is to the left, and the stopped flow data to the right. It is noted that they are of different scales due to $\tau_c < \tau_r$ Although there were also stopped flow data that could be generated, the flow data were of more interest as sensor was not sensitive enough to review experimentally.

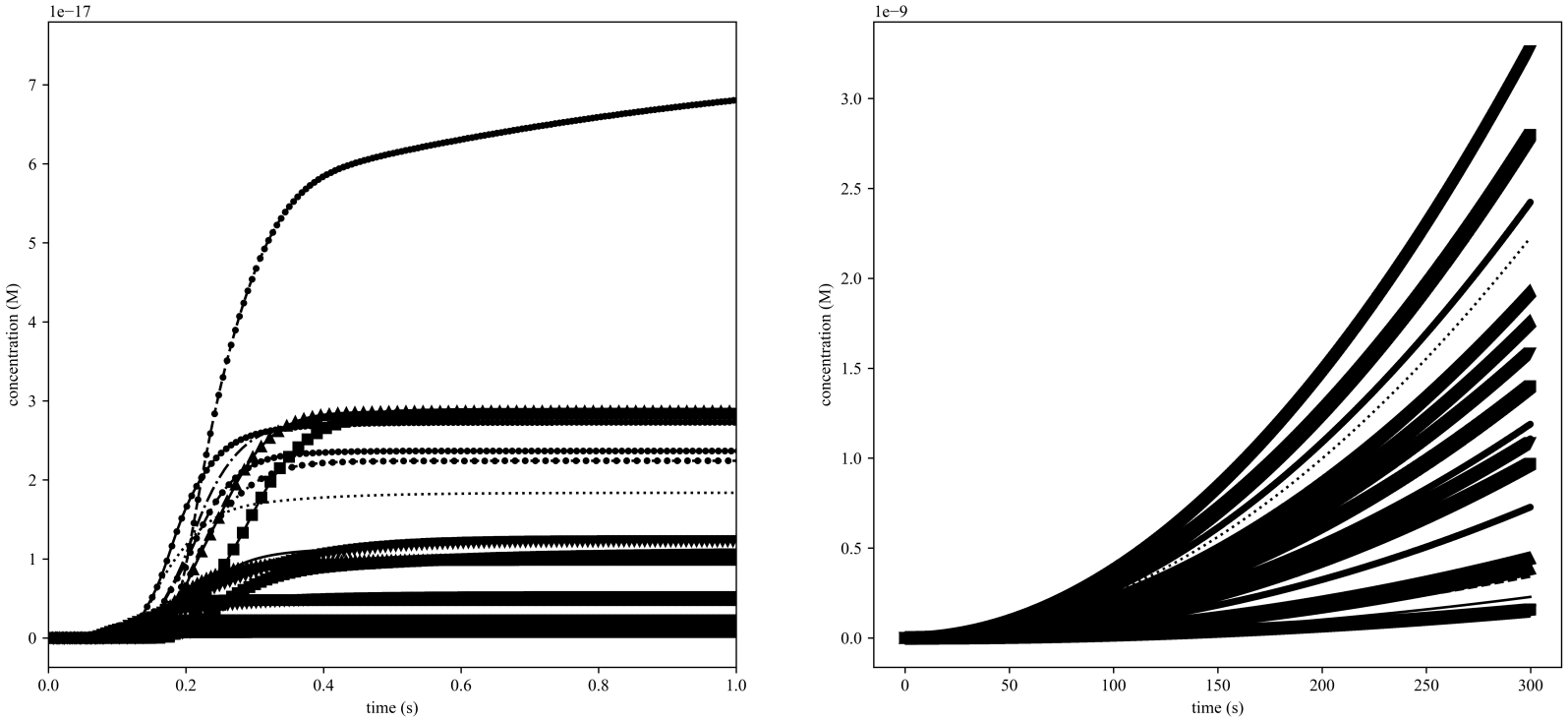

Figure 6.2: Flow data from 100 samples of the CFD output data.

6.3.2 Model structure and coefficient estimation

Firstly, the data were scaled using minimum-maximum (min-max) normalisation. This was done to facilitate better performance of optimisation algorithms, as differing scales can cause performance issues and skew the associated statistical properties used to evaluate the model. The `rivcbjid` (recursive instrumental variable continuous Box-Jenkins identification) algorithm from CAPTAIN toolbox was used to perform system estimation. A step function was included as the input, as the input concentration did not change during a cycle of the sensor, nor was there variation in any of the inputs.

Latin hypercube sampling was used to generate samples from the input parameter space which included the following: Re, c_{in}, u_{in}, dz. Throughout each simulation, the time-varying average concentration along the width of the outlet was collected. The input and output data were passed to the `rivbjid` (recursive instrumental variable Box-Jenkins identification) algorithm for discrete model system identification. The notation $[n\, m\, \delta\, p\, q]$ is used to refer to the parameters for the algorithm to search within, where n is the number of poles, m is the number of zeroes, including the constant b_0 for $m-1$ zeroes. δ is the number of time delays in the input, such that the total time delay is $\delta \cdot \Delta t$ The notation $[n_{min}\, m_{min}\, \delta_{min}\, p_{min}\, q_{min};\ n_{max}\, m_{max}\, \delta_{max}\, p_{max}\, q_{max}]$ defines a minimum and maximum value range for within which permutations of values are run for model estimation. It is assumed that the minimum values are always $[1\,1\,0\,0\,0]$ unless the ranges above are given. As there was no noise in this data, $p = 0$ and $q = 0$.This was restricted to the range $[1\,1\,0\,0\,0;\ 3\,3\,\delta_{max}\,0\,0]$. The time delay range was reduced when the approximate time delay was visible from the CFD output, typically the approximate time delay $\delta \approx (T_d/\Delta t) \pm 20\%$.

To check for the most advantageous coefficient values, a sweep was done for the range $[1\,1\,1\,0\,0;\ 3\,3\,2\,0\,0\,0]$ for each set of data. The numerator and denominator were limited to third order, as due to the curvature at the start and end of the ramp-up stage, the algorithm selected high n and m values to replicate the curve at the start of the ramp-up for the output. As the simulations were run with different time steps for efficient computation, the time steps were inconsistent between different discrete models. The

time step difference was accounted for by converting all of the discrete transfer functions to continuous transfer functions, using the zero order hold method, using the time step that was used for each simulation. The coefficients from the continuous TFs were later reduced using principal component analysis to identify possible model order reduction and parameterisation.

6.3.3 Mechanistic intepretation

$[3\,2\,8\,0\,0]$ was the model structure most frequently identified as the model with the lowest YIC, even though for some sets some of the values may have varied e.g. $[3\,3\,8\,0\,0]$, $[3\,2\,9\,0\,0]$. In this case, it was identified as the most frequent structure to successfully identify coefficients (if applied) to any new incoming data set. When these were converted to continuous TFs, they increased in order due to the zero order hold method. The numerators and denominators of these continuous TFs are shown in Figures 6.8 and 6.9. For Figure 6.8, the first 20 values result in a curve in 3D space, along which each transfer function can be mapped back to. The correlations between α_1 and α_2 are 0.9288, α_2 and α_3 0.9450, and α_1 and α_3 0.7886. For Figure 6.9, a scatter plot of the first three numerator values in each of the transfer functions from the CFD data. The first 20 values result in a curve in 3D space, along which each transfer function can be mapped back to. The correlations between β_1 and β_2 are 0.8782, β_2 and β_3 -0.3936, and β_1 and β_3 -0.6085. All correlations are defined using the Pearson correlation coefficient. It was possible to split the high order TFs into 3 parallel TFs, of which 1 & 2 were conjugate pairs. The results of the parameterisation of the TF coefficients are found in Table 6.2. The gains, time constants, and the expected lag time are all included. The two conjugate first order TFs have been compressed into a real second order TF. There were some outliers which did not form a valid transfer function, these are also numbered and included. The coefficients correspond to the form:

$$H(s) = \frac{G_1 G_2}{T_1 T_2 s^2 + (T_1 + T_2)s + 1} + \frac{G_3}{T_3 s + 1} \tag{6.20}$$

Table 6.2: Continuous TFs broken down into 2 parallel models, a second and first order model.

no.	G_1G_2	G_3	T_1T_2	T_1+T_2	T_3	Z/u_{mean}
1	4.01E-36	6.56E-18	0.00089543	0.032696	0.052384	0.025
2	1.34E-37	1.23E-18	0.0002649	0.019071	0.030074	0.028
3	1.23E-34	7.51E-17	0.0096141	0.055821	0.38939	0.05122
4	8.68E-37	1.03E-17	0.0014178	0.024507	0.21389	0.046667
5	9.69E-40	1.02E-19	0.00021295	0.017079	0.026081	0.025301
6	1.17E-35	1.13E-17	0.0012243	0.037662	0.06172	0.028378
7	3.32E-36	5.67E-18	0.00094061	0.037411	0.050876	0.034426
8	2.03E-36	7.46E-18	0.0041866	0.060822	0.35348	0.044681
9	6.27E-35	2.98E-17	0.0028517	0.054093	0.11165	0.036207
10	7.18E-37	3.51E-18	0.0002488	0.023465	0.044869	0.023333
11	6.84E-38	8.60E-19	0.00016448	0.014807	0.023002	0.022105
12	8.05E-36	9.33E-18	0.00077943	0.032932	0.050186	0.048837
13	1.55E-34	8.51E-17	0.0088397	0.052958	0.37285	0.04375
14	5.74E-37	2.34E-18	0.0015351	0.050757	0.52967	0.025
15	1.68E-34	6.30E-17	0.0049587	0.058784	0.20235	0.044681
16	2.47E-35	1.60E-17	0.0015867	0.043009	0.067995	0.034426
17	1.57E-37	1.32E-18	0.0010692	0.035129	0.058672	0.02561
18	5.66E-37	2.54E-18	0.00029803	0.020438	0.032141	0.029577
19	1.95E-36	5.07E-18	0.00045991	0.027532	0.044277	0.036842
20	2.82E-34	6.12E-17	0.0040145	0.064205	0.12698	0.04375
21	5.70E-35	2.43E-17	0.0011932	0.039161	0.060543	0.063636
22	6.69E-35	5.72E-17	0.0054181	0.038342	0.28936	0.031818
23	4.51E-35	2.11E-17	0.0020588	0.049799	0.075245	0.042
24	1.27E-36	3.63E-18	0.00042458	0.02475	0.035833	0.022826
25	7.46E-37	2.84E-18	0.00027681	0.018924	0.02991	0.029167
26	6.98E-38	8.27E-19	0.0009001	0.035314	0.049891	0.030882

27	1.25E-36	3.72E-18	0.0003735	0.023335	0.035046	0.023077
28	4.06E-35	2.09E-17	0.0010662	0.040265	0.05883	0.055263
29	5.94E-34	1.01E-16	0.0052705	0.068994	0.17308	0.047727
30	5.75E-36	7.71E-18	0.00058806	0.027328	0.041578	0.022581
31	7.83E-37	1.97E-18	0.001243	0.04466	0.3434	0.02234
32	1.45E-37	1.66E-18	0.00015628	0.020473	0.045322	0.021875
33	5.02E-35	2.44E-17	0.0013145	0.038382	0.067469	0.026582
34	2.55E-35	1.61E-17	0.0011599	0.037812	0.057418	0.030882
35	8.46E-34	1.92E-16	0.0095795	0.058501	0.37923	0.058333
36	1.09E-34	3.63E-17	0.0012816	0.047063	0.070002	0.06
37	4.62E-36	7.04E-18	0.0036714	0.0623	0.10537	0.048837
38	2.80E-35	1.71E-17	0.0010385	0.039926	0.05594	0.038889
39	9.34E-36	1.06E-17	0.00063897	0.032846	0.049602	0.040385
40	6.06E-36	8.87E-18	0.00054145	0.031387	0.048638	0.035593
41	2.31E-36	4.92E-18	0.00033015	0.020282	0.032043	0.032308
42	1.83E-34	9.62E-17	0.0075087	0.045784	0.35295	0.046667
43	1.32E-36	3.79E-18	0.00036027	0.021674	0.034264	0.033333
44	1.02E-34	3.33E-17	0.001271	0.045384	0.064542	0.058333
45	1.75E-36	4.40E-18	0.00029834	0.019971	0.031532	0.03
46	4.20E-35	2.18E-17	0.00094432	0.03304	0.055582	0.023864
47	1.14E-34	5.42E-17	0.0028215	0.041108	0.15941	0.031343
48	1.34E-36	3.58E-18	0.011464	0.16594	0.16671	0.02625
49	1.15E-35	1.07E-17	0.00076332	0.032289	0.046307	0.028
50	5.84E-36	1.18E-17	0.00030548	0.025594	0.063133	0.026923
51	2.82E-33	2.15E-16	0.0073255	0.082079	0.19775	0.056757
52	1.75E-37	6.19E-18	0.0004507	0.012653	0.15572	0.022105
53	9.40E-36	2.45E-17	0.00064101	0.026571	0.13279	0.038889
54	4.19E-36	7.95E-18	0.00029268	0.024567	0.042005	0.02561
55	7.81E-35	2.71E-17	0.0014157	0.045783	0.061074	0.042

56	1.58E-34	4.54E-17	0.0012674	0.04923	0.075431	0.0525
57	2.52E-35	1.58E-17	0.00085639	0.035942	0.049328	0.033871
58	1.71E-35	1.42E-17	0.00063338	0.032138	0.048439	0.040385
59	5.45E-34	7.11E-17	0.051958	0.35339	0.36441	0.042857
60	2.26E-33	1.65E-16	0.0051044	0.07234	0.13441	0.05122
61	1.07E-34	3.28E-17	0.001734	0.045717	0.06955	0.0375
62	1.29E-36	4.23E-18	0.00023883	0.021543	0.034754	0.023333
63	6.64E-33	3.08E-16	0.0084361	0.090186	0.19397	0.061765
64	6.73E-36	8.60E-18	0.00039904	0.023396	0.036156	0.035
65	7.54E-37	3.02E-18	0.00024972	0.019621	0.03079	0.025926
66	2.43E-36	5.51E-18	0.00035435	0.023485	0.037248	0.032308
67	6.33E-35	4.75E-17	0.002154	0.028072	0.16111	0.023077
68	1.65E-36	4.15E-18	0.00024064	0.017542	0.027229	0.027273
69	4.36E-36	6.79E-18	0.00031934	0.020026	0.031675	0.031818
70	-1.60E-36	2.38E-17	0.0002603	0.054819	0.080609	0.032812
71	4.54E-35	4.28E-17	0.017084	0.087551	0.50106	0.053846
72	6.90E-35	2.68E-17	0.0007684	0.031521	0.048714	0.05
73	-1.86E-36	4.90E-18	0.00016816	0.0277	0.059543	0.024419
74	6.68E-34	1.32E-16	0.0043916	0.052572	0.20012	0.041176
75	1.32E-35	1.62E-17	0.00033406	0.026993	0.05801	0.027632
76	1.07E-33	1.04E-16	0.0032458	0.06855	0.095462	0.065625
77	9.45E-37	3.15E-18	0.00019102	0.015778	0.024349	0.024138
78	7.39E-34	1.90E-16	0.0066514	0.043836	0.32792	0.045652
79	3.12E-36	6.02E-18	0.00028896	0.020412	0.032044	0.028767
80	2.08E-34	9.86E-17	0.0048103	0.037487	0.26795	0.025926
81	3.26E-35	3.64E-17	0.00065021	0.031633	0.11159	0.039623
82	5.79E-37	2.58E-18	0.00089638	0.036875	0.055647	0.0375
83	2.00E-34	4.93E-17	0.0014145	0.039617	0.071125	0.027273
84	4.25E-35	4.51E-17	0.0016853	0.031372	0.15457	0.053846

85	8.04E-35	2.97E-17	0.0008549	0.031735	0.051953	0.023596
86	2.11E-35	1.85E-17	0.00040231	0.028999	0.052325	0.03
87	1.65E-34	5.06E-17	0.0019348	0.043908	0.097857	0.028378
88	2.00E-36	5.56E-18	0.00028735	0.019121	0.038129	0.022581
89	4.62E-38	7.75E-19	0.00034703	0.02479	0.038788	0.029167
90	1.62E-36	4.97E-18	0.0014711	0.03856	0.084677	0.024419
91	5.53E-38	1.16E-18	0.00036795	0.018758	0.05513	0.027273
92	8.40E-37	2.97E-18	0.00079356	0.03117	0.048672	0.024706
93	1.15E-35	1.05E-17	0.0024365	0.059903	0.080592	0.055263
94	4.94E-36	1.54E-17	0.0040297	0.033041	0.24925	0.033333
95	3.12E-37	1.78E-18	0.00054464	0.028328	0.040144	0.026582
96	6.12E-36	1.76E-17	0.0042722	0.03272	0.26	0.030435
97	2.11E-36	4.49E-18	0.00124	0.041787	0.057652	0.036842
98	9.78E-36	1.01E-17	0.0010999	0.037376	0.058246	0.061765
99	3.71E-38	1.23E-18	0.00028676	0.012729	0.061522	0.023864
100	NaN	NaN	Inf	#NAME?	#NAME?	0.041176
101	NaN	NaN	Inf	#NAME?	#NAME?	0.023333
102	NaN	NaN	Inf	#NAME?	#NAME?	0.053846
103	NaN	NaN	Inf	#NAME?	#NAME?	0.032812
104	NaN	NaN	Inf	#NAME?	#NAME?	0.027273

Table 6.3: Regression coefficients from Figure 6.3.

	c_{in}	u_{in}	u_{mean}	const.
G_3	1.20E-12	-1.83E-16	-1.27E-15	1.34E-16
T_3	-910.66	-0.39432	-1.5774	0.34591

The list of parameters from Table 6.2 take the form of Equation (6.20). The gain G_1G_2 was orders of magnitude smaller than the first order TF. Therefore, it can be

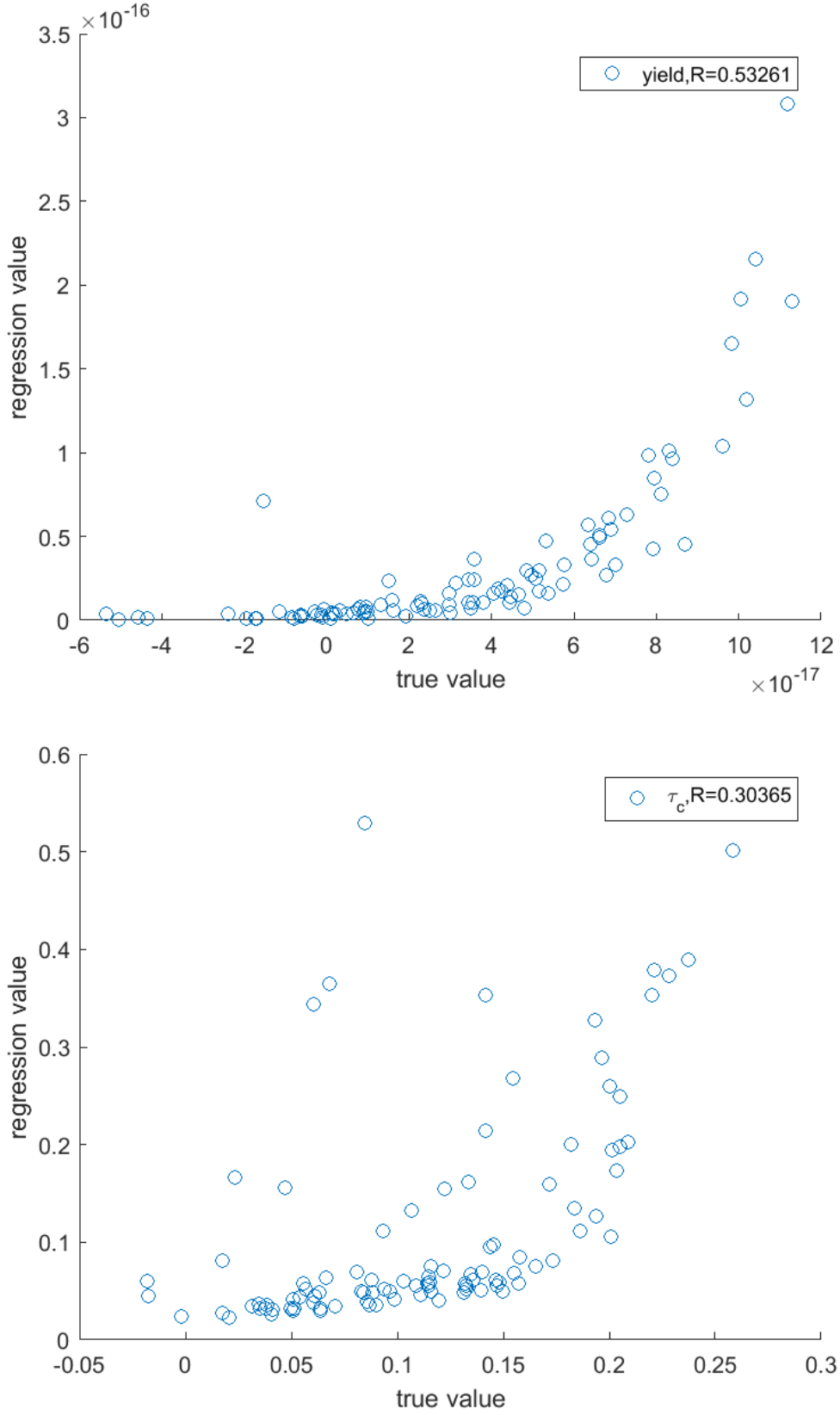

Figure 6.3: Yield and τ_c regression using the input variables c_{in}, u_{in}, u_{mean} and output variables G_3, T_3.

assumed that the parallel first order TF is dominant in describing the system, and that T_3 can be taken to be τ_c. The step responses of transfer function of row 50 of Table 6.2 can be seen in Figure 6.4. The upper figure represents the second order TF, and the lower figure the first order TF. The response magnitudes between each are of the order 10^{19}. The time scales also differ by an order of magnitude. To identify a link between the input parameters and G_3 and T_3, a multilinear regression analysis was performed with the input parameters. The results of this are in Figure 6.3, which does not infer a strong correlation. It is evident from the R^2 values obtained that there is a non-linear relationship between the input variables and the gain (G_3) and τ_c (T_3). The equations for each are in Table 6.3. The regression coefficients are also included in Table 6.3.

6.3.4 Model reduction

The next step was to parameterise the coefficients of the poles and zeros to attempt to reduce the degrees of the freedom. To do this, the coefficients from the above section were included as part of a principal component analysis (PCA) which included the coefficients from each continuous transfer function. The MATLAB algorithm `pca` was used to perform the PCA. When plotting the parameters in the same space, it was found that in the plane of the numerators, there was a line in the denominator space along which these lay. In the denominator space, those points formed a surfacee. The explained output from PCA was used to show how much each principal component (PC) accounted for the makeup of the end score. In the example that was used here, it was shown that 95% of the model was accounted for in the first 3 PCs. The first PC accounts for 52%, the second 38%, and the third 5%. This was then mapped back using the coefficients to see how much of a difference there was between the original models that resulted form the CFD model versus the reduced models.

It was shown that there was for many of the components only an order of magnitude difference, as can be seen in Figure 6.7, where the blue labels show the scores with the maximum number of PCs (6) versus the difference in the inverse scores that were obtained using only 3 PCs. Figure 6.7 shows how representative using the first 3 PCs,

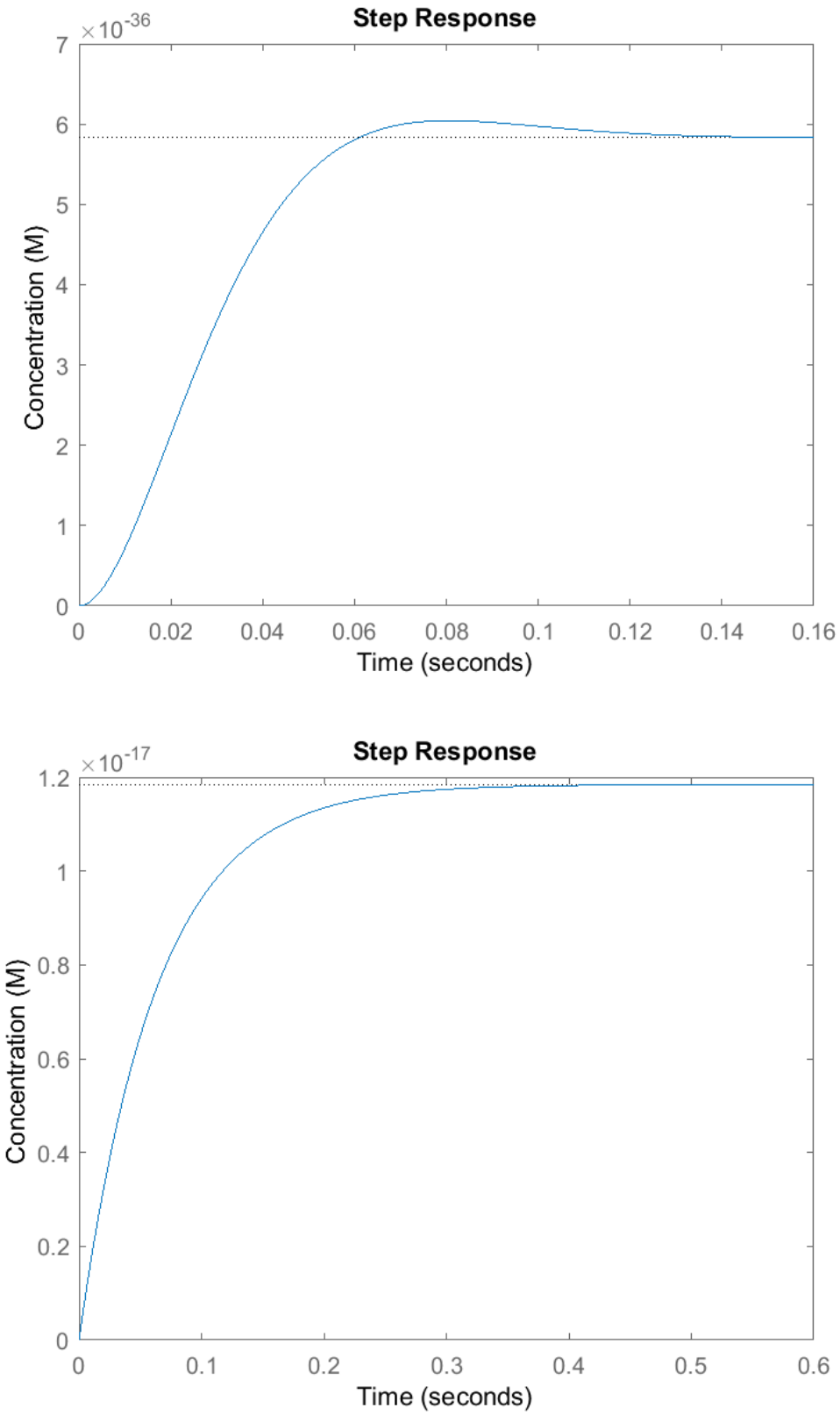

Figure 6.4: Step response of transfer functions from line no. 50 in Table 6.2.

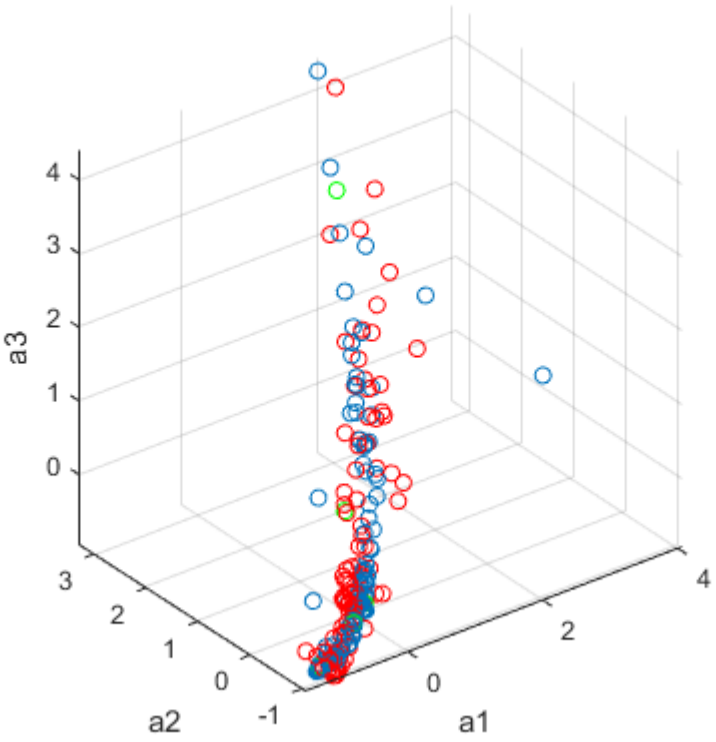

Figure 6.5: The coefficients of the denominators plotted against the first 3 PCs.

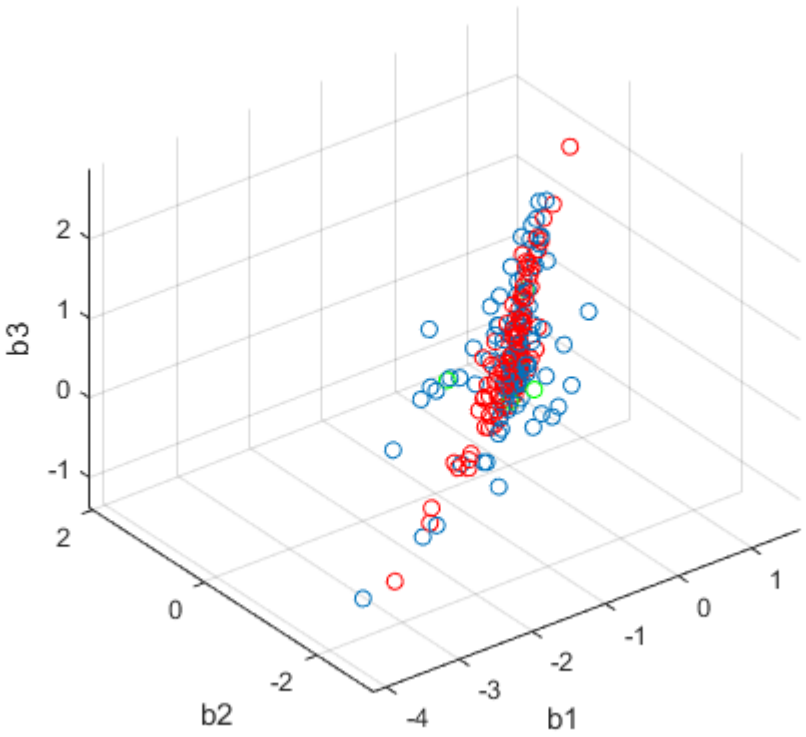

Figure 6.6: The coefficients of the numerator plotted against the first 3 PCs.

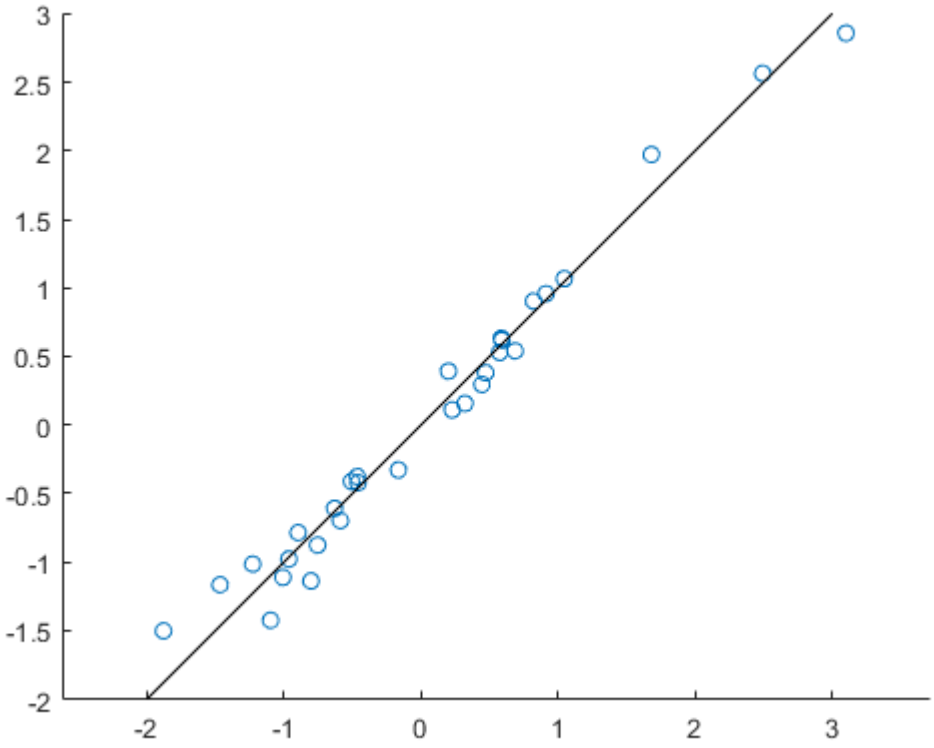

Figure 6.7: Scaled PCA scores (x axis) plotted against the reconstituted parameters using the first 3 principal components (PCs) of the original 6 PCs. Scores closer to the line are a closer match.

rather than all 6 PCs, are for using the parameterisation obtained to get the numerator coefficients.

6.3.5 Hold-out data for validation

The hold-out test data were included in the optimisation by scaling them according to the sample data that was generated above and then plotted into the above. It can be seen that the points line up relatively near the curve that was generated within the same data. This shows that the model generation is holding for new parameter sets which were not included in the original optimisation. The differences measurement was also used, this showed good improvement.

6.3.6 Joining of steady state and stopped flow data

The two models from the CFD were difficult to incorporate together. One reason for this was the difference in scale between the flow data and stopped flow data. The flow data collected were on a scale of $1\,\mathrm{ms}$ and $10\,\mathrm{ms}$ and for stopped flow data this was 15 times larger for one run (1.6×10^{-5}, 0.095, 0.051). Additionally, the scale of the output data was significantly different for both shapes. In one of the runs (1.6×10^{-5}, 0.095, 0.051) (where the format of the values inside is (c_{in}, u_{in}, u_{mean})), the difference in the steady state maximum value 4.19×10^{-17} and the last value achieved from the stopped flow data – which had not finished before the simulation – 3.07×10^{-12}, were vastly different and not conducive to forming a unified transfer function model on the CFD data.

6.3.7 Rationale for CFD TF model generation

One of the reasons that the CFD model was used to assess yield while the system was flowing was because there was difficulty in monitoring how the yield would be produced. Firstly, it is difficult to track the concentrations of the reactants in the detector channel, as some are not visible or below detectable quantities. Secondly, the system

is optical and operates in a dark environment, inside an opaque black Pelicase. Inherently, using an optical measurement to examine for any trace amount would interfere with the yield measurement that is placed by the PEDD. Therefore, it was not feasible to collect this data experimentally, and the sensitivity of the device, upon collection of experimental data verified that the minute quantity of colorimetric complex was not detectable.

Modelling continuous flow data as separate TF

The plotting of the coeffficients of the continuous TFs show a possible parameterisation as the denominator coefficients lie along a line. The parameterisation is a bit more complex for the numerator as this lies as a surface in 2D space, but still the correlation is greater than 0.8 for these, as can be seen in Figure 6.6. These are demonstrated in Figures 6.5 and 6.6. For Figure 6.5, the blue data are plotted using all of the PCs, the red data against only the first 3 PCs, while the green data is inserted from a held-back data set to assess the characterisation. The curve shape is where most of the data lies in the system. For Figure 6.6, the blue data are plotted using all of the PCs, the red data against only the first 3 PCs, while the green data is inserted from a held-back data set to assess the characterisation. A possible method for the calibration would be to see if there is a fit that is made to the data, if the new parameters are very far away from the reference parameters, then there is a method to establish if the coeffients for an identified system are similar to other previously identified models.

6.4 System identification using experimental data

6.4.1 Cleansing of experimental data

Artefacts of deleterious effects

The main deleterious effects, as mentioned above, were the background sinusoidal pattern, white noise and significant optical interference. The sinusoid noise can come from plugging in the flow channel due to imperfect mixing. This is associated with the imper-

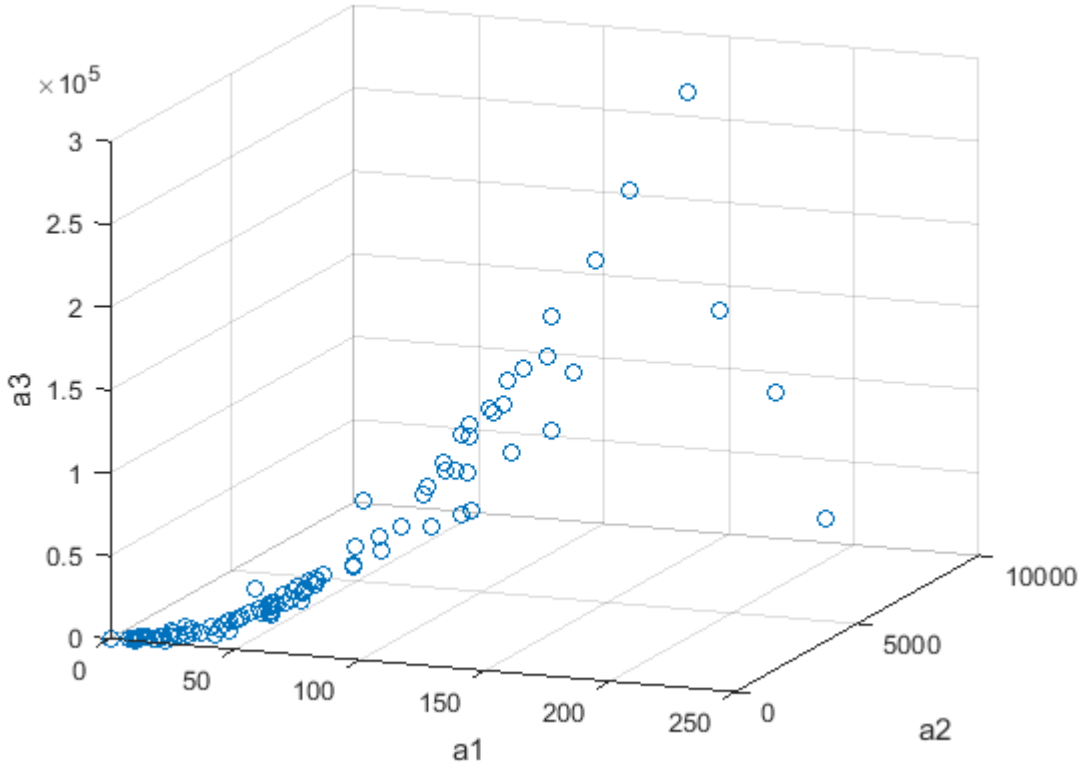

Figure 6.8: A scatter plot of the first three denominator values in each of the transfer functions from the CFD data.

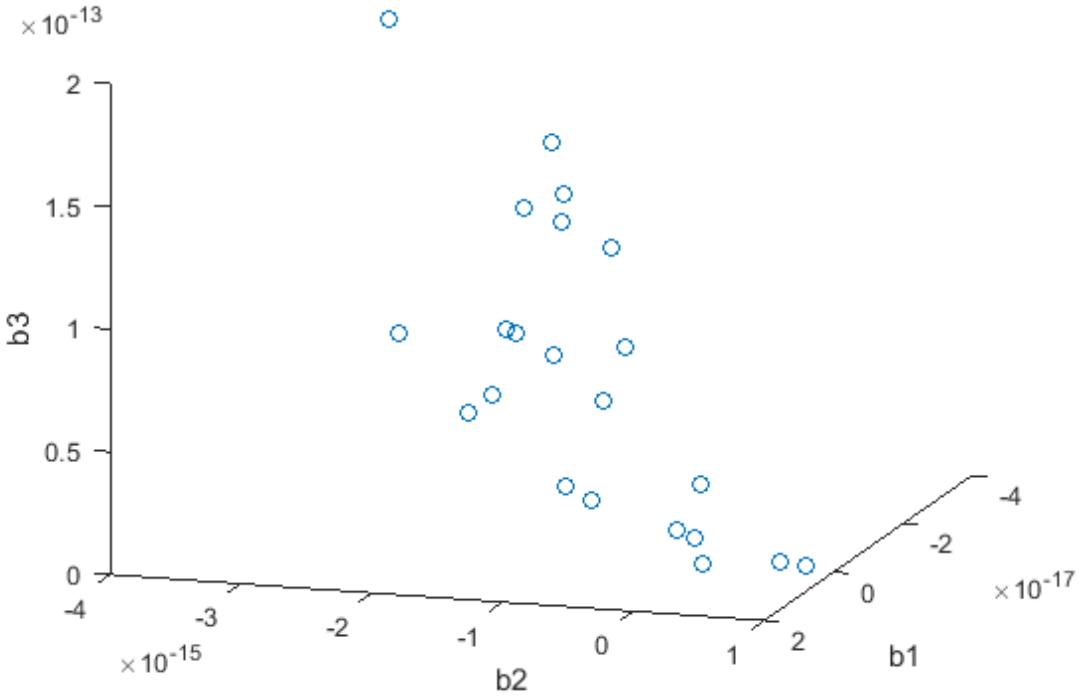

Figure 6.9: A scatter plot of the first three numerator values in each of the transfer functions from the CFD data.

timestamp	k	y	u_1	u_2	u_3	u_4
20180708_213000	0	0	0	0	-31	0.75
20180708_213000	1	0	0	0	-31	0.75

Table 6.4: Example segment of the sensor output data. The file is structured that the sample number for the run is followed by the voltage reading (output) and included inputs. The final input (standard concentration) is added in data postprocessing.

fect control of the brush controls used in the syringe pumps. The white noise is inherent due to the electronic nature of the system. The optical interference comes namely from 2 sources, that being the opening of the enclosing opaque case and bubble obstruction in the detector channel. Bubbles strongly interfere with the optical properties of the detector channel and have the effect of diverting light away from the sensor, which is detected by the sensor output as a sharp peak and indecipherable data.

Preparation of data for model estimation

File concatenation The data collected needed to be cleansed in Matlab. This required that the imported data was first appended together. The concatenated run data file consisted of 10 csv files which covered 5 runs of one standard and 5 runs of another, allowing for the inclusion of several inputs, including reagent ratios and standard concentration. The formation of the csv data is included in Table 6.4. The time between cycles was fixed, therefore knowing this, the appropriate number of zero rows was added to ensure that there were no missing samples. The inputs for sample number, and the previous reagent ratio and concentration were used as the reaction mixture was still present in the detector while not operating.

Standardisation The input and output data all varied on different scales, from 10^4 for the voltage encoder reading, to 10^{-1} for the reagent flow ratio. To allow for better modelling, all these parameters were required to be on the same scale. This was completed by transforming all data by subtracting the population means for each parameter and dividing by the population standard deviation for each parameter. This resulted in each parameter (input and output) being of zero mean and unit variance. This allowed

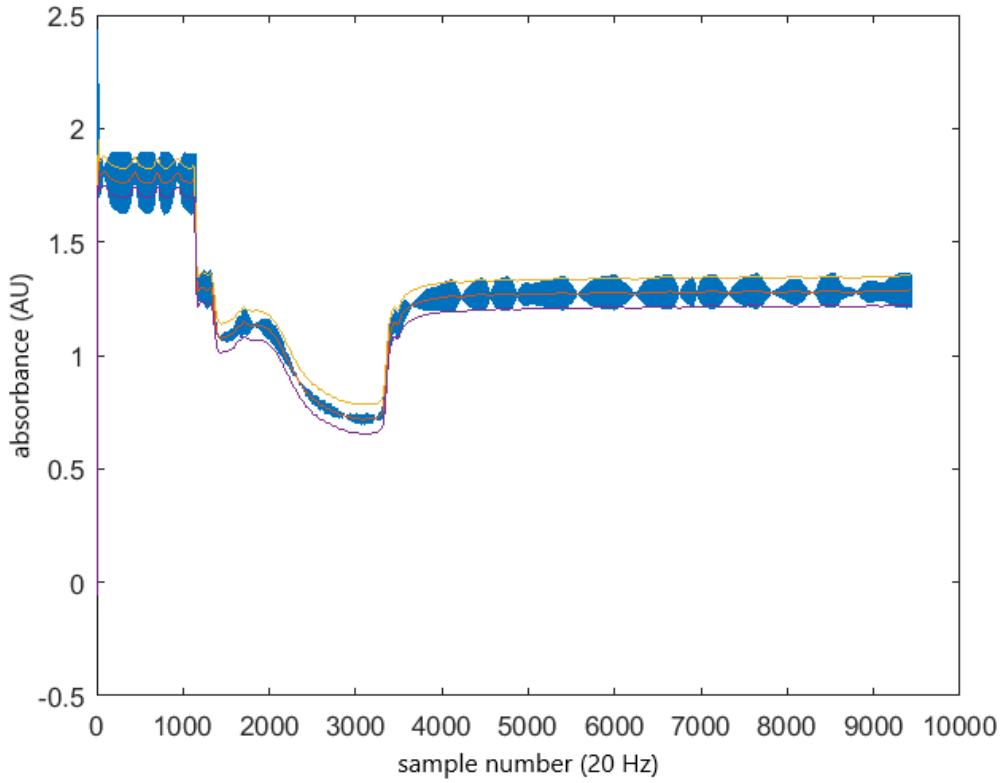

Figure 6.10: Noisy data with IRW smoothed data overlaid. The uncertainty is also shown, which encloses the noisy pulses throughout the data run.

for better and more successful modelling, and for each parameter to have an equal scale in the eyes of the modelling algorithm, providing them with equal importance. With a model created from the standardised data, it is possible to standardise any new input data, and to destandardise any output data.

Smoothing The data collected from the colorimetric sensor were inherently noisy. This was an issue in particular for lower voltage values – caused by high concentrations – within the detector channel. The extent of the noise is demonstrated in Figure 6.10, where these were quite noisy, and had an underlying sinusoidal pattern. Firstly, it was important to attenuate the sinusoidal pattern. The noise affecting the system was asssumed to be random walk noise. The integrated random walk (IRW) smoothing optimisation (`irwsmopt`) algorithm from CAPTAIN toolbox was used to generate the hyper-parameter for the noise variance ratio (NVR). This was then used to perform IRW smoothing. The result of the smoothing is plotted in Figure 6.10.

6.4.2 Data smoothing

The data were required to be preprocessed prior to fitting. There was significant noise within the signal, which made it difficult to use as a basis for modelling. Below were some of the approaches considered to reduce the noise.

Moving average

A moving average filter was applied first to the data. The window used was a 20 point moving average. With the sampling frequency being $20\,\mathrm{Hz}$, this meant that the signal was averaged over a second. To apply this filter, with n being the length of the averaging, the recursive filter was applied.

$$y(k) = \left(1 - \frac{1}{n}\right) y(k-1) + \frac{1}{n} u(k) \tag{6.21}$$

The moving average filter did not sufficiently remove the sinusoidal signal, such that system identification could not be performed. The noise was still significant when a filter using $n = 20$ points was applied to the data. For larger windows, this was reduced, but there was an effect of over-filtering the data, which meant that some of the signal characteristics were being averaged out, which was an undesirable effect. Therefore, the moving average was not used to smooth the data.

Savitzky-Golay filter

As mentioned previously, this filter achieves smoothing by interpolating an n^{th} order polynomial filter, with a window width w where $w = 3, 5, ...$ This method was developed by Savitzky and Golay [86], and requires the use of historical (to $n - w - 1$) and future data points (to $n + w - 1$). It is used typically in colorimetry to smooth data while retaining information formed at the peaks. This worked well to solve the issue with noise, however a large window was required, and there was also still the artefact of the sinusoid which was present in the curve, this is notable in Figure 6.10. In terms of using on a live system, the use of future data precluded this filter from being used in

such a manner.

Integrated random walk (IRW)

Integrated random walk smoothing attenuated much of the sinusoidal signal in the data. As can be seen in Figure 6.10, much of the background noise is sinusoidal nature. Upon first smoothing using a moving average, the sinusoids become more prevalent. IRW allowed for this background sinusoid to be removed. To note, there are some thoughts to the nature of this behaviour. Regarding a Y-junction micromixer, there is potential for some axial plugging. This would affect the recorded absorbance in the sensor as the speed and ratio of flow between the inlets were adjusted. An example of the change in sinusoid at the flow stage can be seen in Figure 6.13.

Absorbance

The absorbance calculation is based on the difference between the zero voltage reading (V_0) and the voltage reading in the presence of CC. Absorbance is calculated using V_0 as mentioned previously, but again for reference:

$$A = -\log \frac{V}{V_0} \tag{6.22}$$

where V is the output voltage of the photodetector.

6.4.3 Model identification using SRIV

The sampling frequency used to collect the data was $20\,\mathrm{Hz}$, and initially used with the SRIV algorithm from CAPTAIN toolbox. As each data set lasted on a period of 8 to 10 minutes, this meant that each data set had up to $12\,000$ data points. To reduce the overall quantity of data while still providing enough data for system identifiction, one approach used was to subsample the data, such that the effective sampling frequency was reduced to $0.2\,\mathrm{Hz}$, a reduction of 100 fold. Another approach that was used was to smooth the data using the Savitzky-Golay filter [86]. This was done using a second

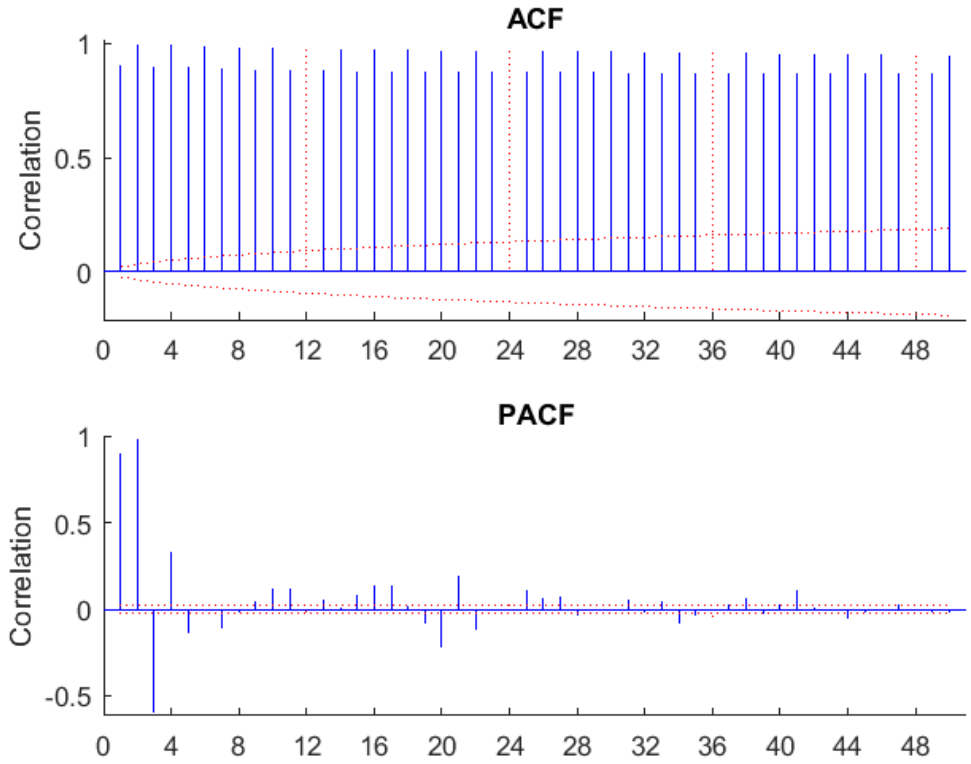

Figure 6.11: Autocorrelation and partial autocorrelation functions run on the same data as Figure 6.10.

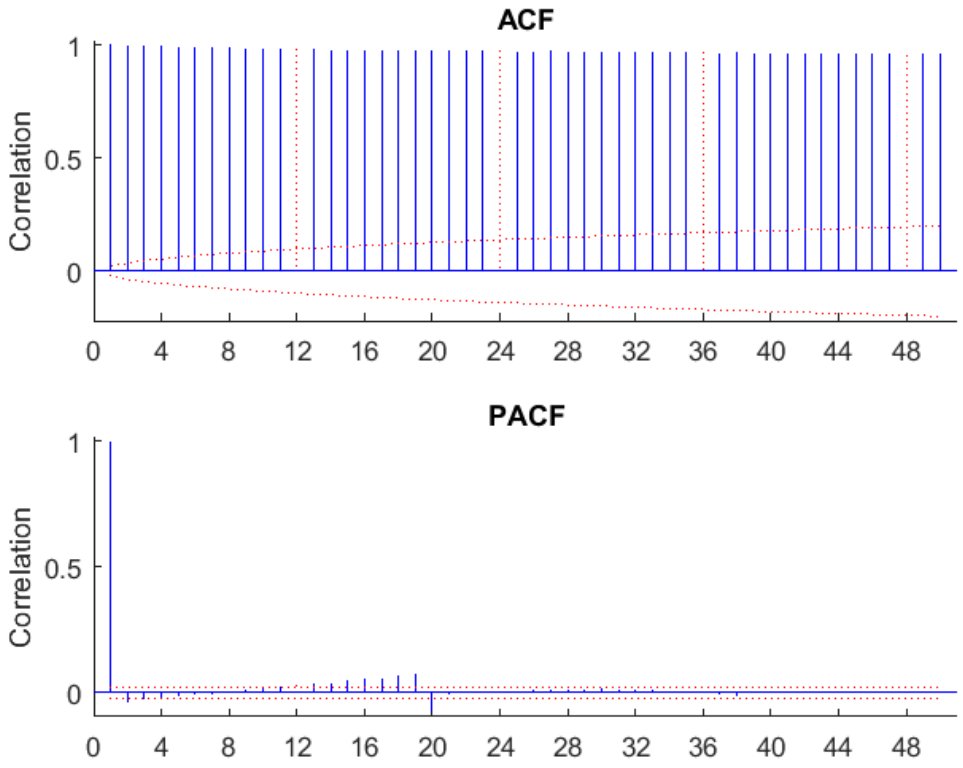

Figure 6.12: Autocorrelation and partial autocorrelation functions run on the filtered data from Figure 6.10. The information from the PACF analysis suggested that a 20^{th} order model would be suitable for modelling.

order polynomial fitting, with a window size of 3, to mitigate over-smoothing the data. This was done to allow a smoothed data set to perform the optimisation, and to ensure that the fitting algorithms for the system identification could operate well enough.

The SRIV identification was implemented by creating two inputs: one was a step response for the system in the flowing state, while another was a switch that flicked instantaneously. This was used for a flowing data set in which there was initially a concentration which was obtained from a previous run.

There were some issues when the data were extended and repeated, to create new data, in which an input of switching on and off would be matched to the repeated output in which the step function input was 1 for the system running, and zero for when this was not the case. When the input data were changed, to result in a change of value, although there was an adjustment in the flowing state of the data, there were issues with the stopped state. This went into a negative state which is not representative of a real system. Additionally, there was no accounting for the initial state (assumed to be at a non-zero value) and there is data which is residual from the previous run.

Fast flow

One issue which was encountered in collecting data from the sensor was the use of a high flow speed. In repeated runs for this setup at the same flow speed, 1:1 ratio and reactant concentration, the stopped flow curves varied greatly between subsequent runs. Figure 6.13 shows the difference between subsequent runs for different standards, which are labelled in the diagram.

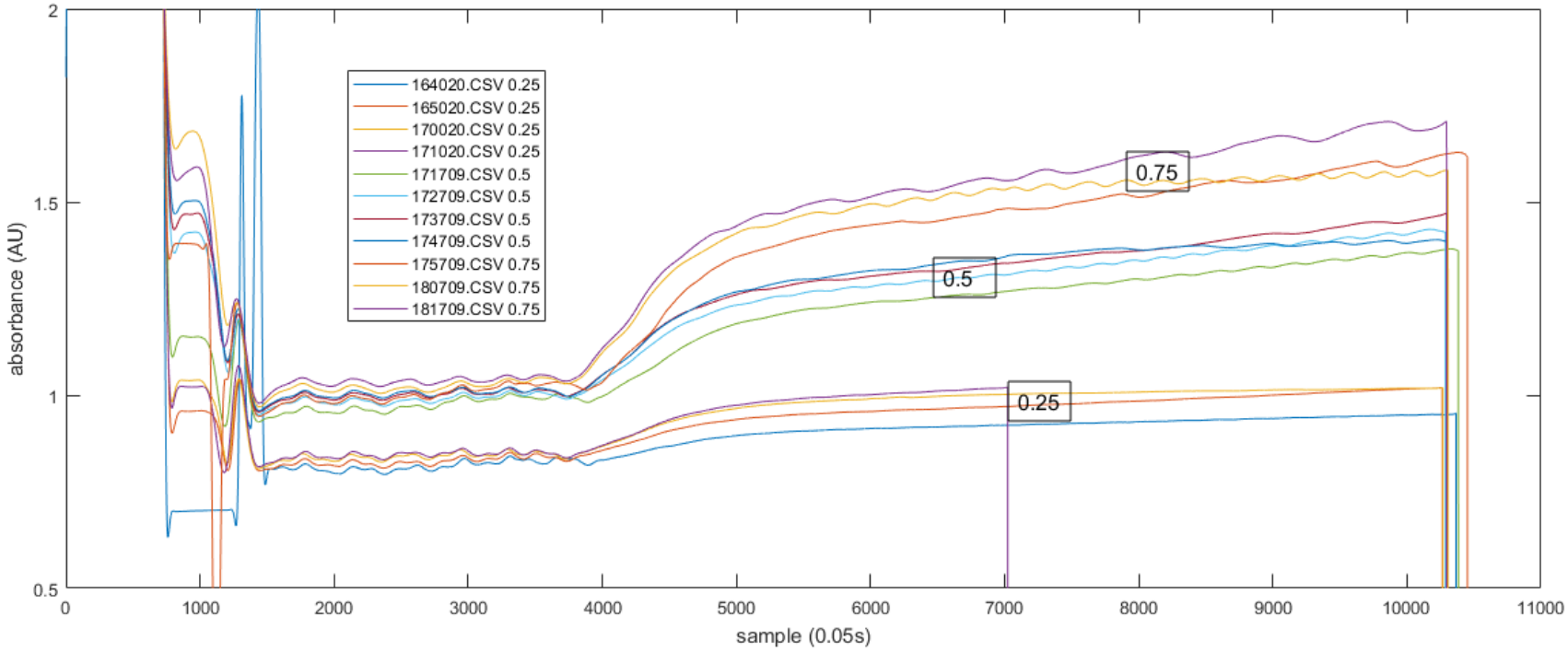

Figure 6.13: Standards sequentially run, as marked in the legend. The concentrations used were $0.25\,\mathrm{mg\,L^{-1}}$, $0.5\,\mathrm{mg\,L^{-1}}$ and $0.75\,\mathrm{mg\,L^{-1}}$. This corresponds to absorbances of 0.9658(0.0394), 1.2878(0.036) and 1.4830(0.0381).

In addition, there was also noise which was present in the flowing segment of the cycle, with a period of 80 samples ($4\,\mathrm{s}$). The instability was reduced when the flow speed was reduced to 10. In addition to this, the period of the noise in the flowing part of the cycle increased to 250 ($8.33\,\mathrm{s}$), which is proportional to the change in the flow speed. It follows that at the higher flow speeds that there may have been issues with plugging in the flow, as plugs of differing widths would sit in the detector channel, causing the initial instability. In addition to that, the lengthening of the period would suggest a non-electrical change, i.e., the change is coming from the solution in the detector channel instead.

6.4.4 Stop flow model estimation

Multiple runs were obtained for each of the flow ratios to used for system identification of the stopped flow data collected from the photodetector. The ratios ran were 1:1, 2:1, 3:1 and 4:1. It was expected that the higher ratios, following from the computational runs, would result in more reaction. The data is charted in Table 6.5.

Results

Table 6.5: Parameters estimated using the `rivcbj` algorithm with input experimental data. Data varied by sample-to-reagent ratio and input concentration.

data file	u_{in}	c_{in}	u_{flow}	G_1	G_2	T_1	T_2
095343.CSV	0.5	2	10	0.22483	0.093701	21.566	165.83
100343.CSV	0.5	2	10	0.25899	0.10315	18.183	154.2
101343.CSV	0.5	2	10	0.26826	0.10451	18.476	164.72
102819.CSV	0.5	2	10	0.25067	0.099262	17.598	154.47
113908.CSV	0.5	2	10	0.26951	0.11776	18.208	194.36
114908.CSV	0.5	2	10	0.27086	0.1109	18.149	161.1
115908.CSV	0.5	2	10	0.26627	0.11181	17.776	158.38
120908.CSV	0.5	2	10	0.2689	0.11215	17.693	160.89
133247.CSV	0.33	2	10	0.23975	0.085711	21.406	124.49
134247.CSV	0.33	2	10	0.23668	0.090989	20.671	112.1
135247.CSV	0.33	2	10	0.23109	0.087242	20.95	123.56
140247.CSV	0.33	2	10	0.24284	0.086456	21.282	129.07
141247.CSV	0.33	2	10	0.22789	0.088232	20.731	119.56
142247.CSV	0.33	2	10	0.2324	0.08588	21.069	133
143247.CSV	0.33	2	10	0.2129	0.087488	19.815	114.44
144247.CSV	0.33	2	10	0.18249	0.1053	16.73	83.102
145247.CSV	0.33	2	10	0.23629	0.086085	21.192	133.91
152552.CSV	0.25	2	10	0.0053663	-0.089471	12.938	460.29
153552.CSV	0.25	2	10	0.23783	0.098301	20.546	99.432
154552.CSV	0.25	2	10	0.4375	0.080919	25.589	182.77
155552.CSV	0.25	2	10	0.3993	0.091425	23.839	138.68
160532.CSV	0.25	2	10	0.40835	0.09208	23.99	130.58
161532.CSV	0.25	2	10	0.010175	-0.12037	20.285	492.93
162532.CSV	0.25	2	10	0.44449	0.081049	25.579	179.7
165011.CSV	0.2	2	10	0.024465	0.085408	23.159	174.65
170011.CSV	0.2	2	10	0.00066215	0.046233	0.7198	7526
171011.CSV	0.2	2	10	0.0010408	0.21692	0.48127	42914
172018.CSV	0.2	2	10	0.00010697	0.0036913	2.6043	781.66
174718.CSV	0.2	2	10	0.00058955	0.0021316	0.24261	316.17
181914.CSV	0.25	1	10	0.33958	0.13011	27.944	176.98
182914.CSV	0.25	1	10	0.30357	0.13828	28.874	195.84
184025.CSV	0.25	1	10	0.29054	0.14027	29.634	207.14
184953.CSV	0.25	1	10	0.30722	0.1426	32.021	328.9

Table 6.6: Summary of results from Table 6.5 where the means and standard deviations are grouped by sample-to-reagent ratio and concentration.

ratio	concentration (ppm)	G_1	G_2	T_1	T_2
1:1	2	0.2578(0.0147)	0.1067(0.0074)	18.4561(1.2085)	164.2438(12.0502)
2:1	2	0.2269(0.0177)	0.0893(0.0059)	20.4273(1.3806)	119.2480(14.6343)
3:1	1	0.3102(0.0180)	0.1378(0.0047)	29.6183(1.5108)	227.2150(59.6883)
3:1	2	0.2776(0.1969)	0.0334(0.0951)	21.8237(4.4719)	240.6260(164.0161)
4:1	2	0.0054(0.0096)	0.0709(0.0792)	5.4413(8.8982)	10342.5(16517.6)

The data collected from this run was stable and repeatable, as demonstrated in Figure 6.14. The higher-skewed ratios show a breakdown in coefficients as the data collected became instable, as can be seen in Table 6.5. This was due to mechanical limitations in the brush motors used to power the syringe pump. To maintain a constant mean flow rate in the chip between different runs, the reagent syringe draws a lower volume and injects as a slower rate, and the inverse is true for the sample syringe. A minimum voltage is required to be applied to ensure that the motor is powered. However, there were also some rounding errors which result in one syringe finishing before the other, meaning the colorimetric complex is flushed from the detector channel before absorbance is measured.

6.4.5 Identified models

The data from Table 6.5 shows the results from modelling the stopped flow data as a second order model, split into 2 parallel first order models. The most interesting point to note are that the first order models can be interpreted to represent a two stage reaction, similar to the Griess reaction itself. The time constants that are extracted from these are different on an order of magnitude. This is important where the solution is left to stand in the photodetector channel for over 5 minutes at a time. The data collected suggests that $60\,\mathrm{s}$ ($\approx 3T_1$) is sufficient for most of the colour development to occur in the reaction, and that any further colour development is from the second reaction step identified in the above process. It is also important that varing the ratio and concentration did not greatly affect the modes, except for 4:1. This was due to an inability of the syringe pumps to operate at a slow enough speed to permit such a ratio to flow steadily without axial plugging developing.

6.5 Conclusion

This chapter examined the underlying mechanistic models that can be derived from the reacting flow system, as well as data-based models which have identified zeros,

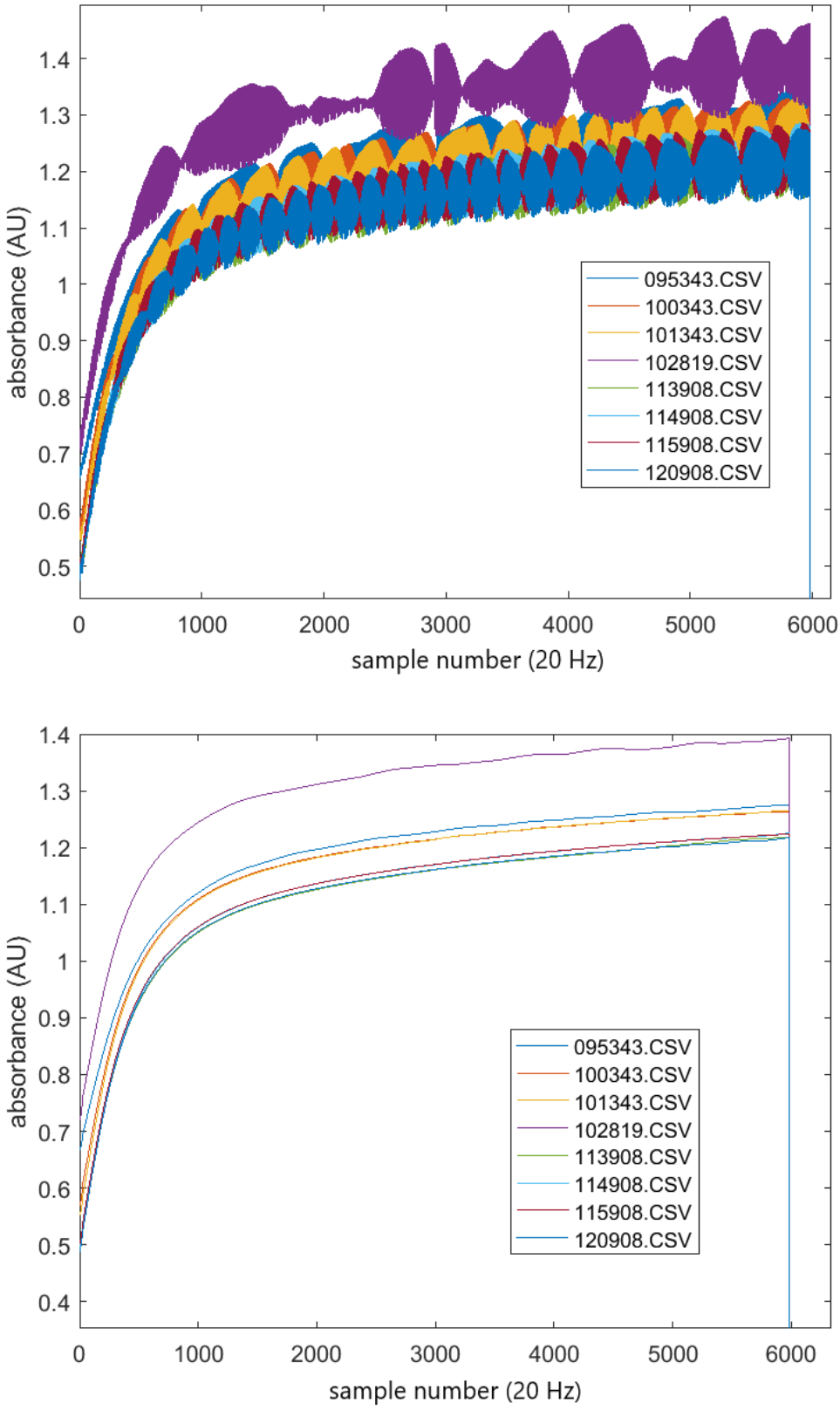

Figure 6.14: Repeated runs of 1:1 stopped flow data, both raw absorbance and filtered data. The legend shows the label from the time run. All data were collected on the same day.

poles and coefficients. The flow data collected from the numerical simulations was restricted to system identification via data-based modelling, which identified a $[3\,2\,8\,0\,0]$ model as a best fit. The coefficients for both the zeroes and poles could be separately parameterised using principal component analysis, with a possible parameterisation of the coefficient reduced to only three degrees of freedom. For the stopped flow data collected experimentally, it was possible to remove the sinusoidal signal which overlaid the data using IRW smoothing. A second order data-based model was identified as a best fit. The identified model could be expanded into two parallel first order models. This has a mechanistic interpretion as a two-step reaction of differing time scales, which is reflective of the Griess reaction.

Chapter 7

Further characterisation of sensor

7.1 Aims and objectives

The aim of the research described in this chapter was to develop operating procedures to mitigate how the structure of the sensor and electrical components interfered with data collected from the detected channel. Due to inevitable carryover between tests from the continuous-flow method employed within the sensor, investigations were conducted into determining how data collected between readings could be effectively used to correct calculations from previous runs. Staining was also suspected to be a factor in longer-term deployment, the effect of which is reduced sensitivity, and consequentially, a reduced service interval.

Firstly, the detector channel was saturated with a pre-mixed solution of 20 ppm nitrite and Griess reagent. Then, the system was repeatedly flushed with a 1:1 mixture of deionised water and reagent until a zero reading was recorded by the detector channel. Secondly, the photodiode was left on throughout the cycle between different standard and ratio inputs. This data from between cycles was analysed to devise a method to extract a corrective algorithm which could be used to improve sensor accuracy. Thirdly, the microfluidic chip was filled wih a 20 ppm pre-mixed solution of nitrite and Griess reagent. The solution was then left within the chip for over 24 hours, for subsequent visual inspection of aggressive staining.

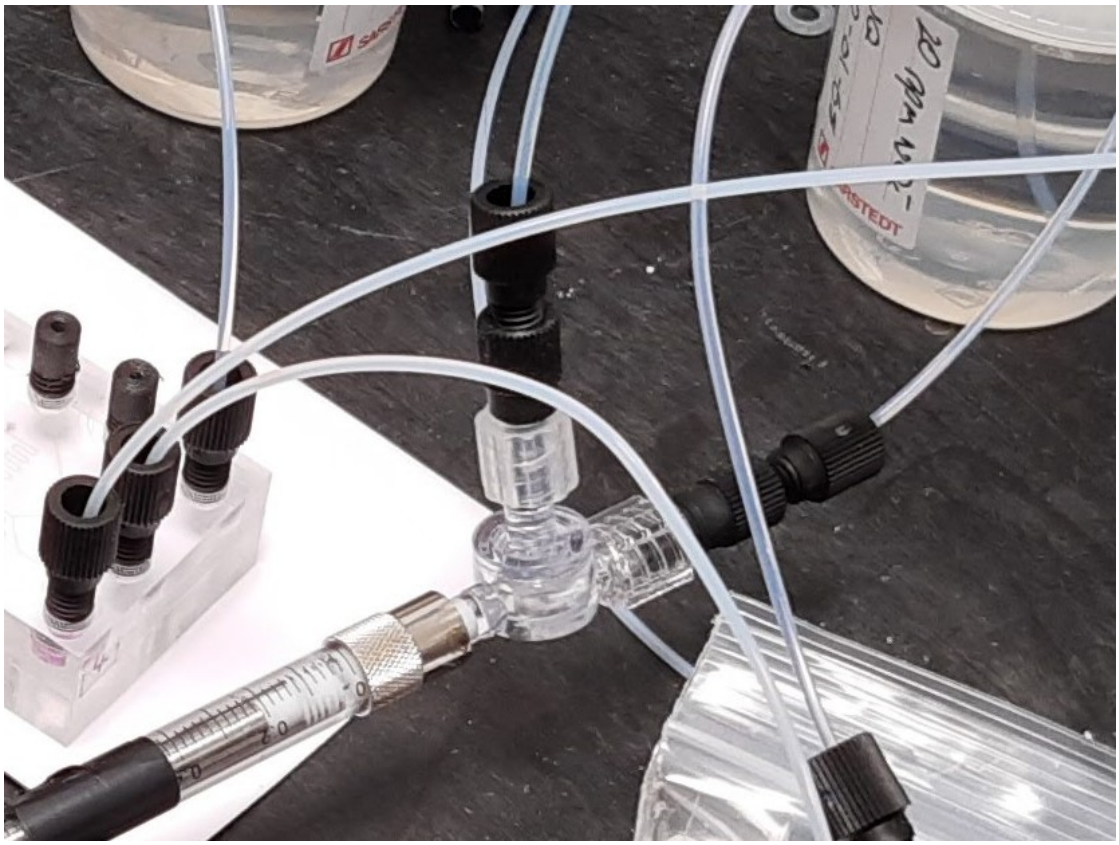

Figure 7.1: The three way connector which separates flow from the reservoir to the syringe, and from the stringe to the sensor.

7.2 Hysteresis

The hysteresis effect is suspected as when the system flushes, not all of the sample would be removed, resulting in carryover between readings. Some of the sources of this include along the walls of the microchannels. The main source was suspected to be in some of the tubing and connector pieces.

7.2.1 Three way connector

In Figure 7.1, the three-way valve can be seen which connects the reservoir to the syringe pump and the microchannel. The reservoir links to either the reagent, sample from the onboard reservoir or an onboard standard. The syringe draws liquid from the reservoir into the syringe, then the valve permits ejection. There is some dead volume associated with the valve, and this is a potential cause of concern for storing fluid between runs. The fluid enters through the reservoir, and then drawn into the syringe. After, the

fluid is ejected through the connector to the chip, where the colorimetric analysis takes place. This was suspected as a potential source for contamination between runs. To test this, a concentrated premixed solution was placed within the microfluidic chip, and left to rest for some time.

7.2.2 System run

The data collected within the run contains all of the necessary information to complete the time staggered concentration estimate. The run consists of many stages. Firstly, when the system is filling, the LED is left off while the pumps work to fill the syringes with sample and reagent. One reason for this is to estimate the degree of white noise that is within the system. While this may be averaged out or not always be of concern, at high concentrations or regions of near saturation, it becomes important as the proportional amount of the noise is calculated, so that values below the LOD and saturation are ignored. Another reason for this is to check if there are any other sources of light entering the system that are outside of this. This can come from a variety of sources, but namely if the system has been opened. This could be due to an act of vandalism or if the system has become impacted and otherwise damaged.

Secondly, to simulate a new sample coming in, the sample reservoir was replaced with DI water, and the sensor was then run, using a 1:1 reagent-to-sample ratio until the sensor returned a completely blank reading. The solution was deemed flushed when the absorbance value was less than 2 mAU. To perform a confirmatory test for the suspected hysteresis that this was due to the fluid in the interconnecting pieces, a separate syringe pump containing DI water was connected to the system. This was then injected solely on its own to remove any dye from the system. The absorbance data point that was collected was the last value that was obtained in the stopped flow section for each data run.

Thirdly, any solution from the previous run had been flushed out, meaning that fresh solution was arriving at the PEDD from the current run. With the exception of high concentrations, this was almost always a flat line. If there is some reading present here,

there will be a turning point near the start of this section where there will be slope, from which some hysteresis can be considered. A high range value can be averaged out, and is not time dependent as the flowing system reaches a steady state at such an early stage. This section is known as AF_n, and is pertinent to the higher concentration ranges that are present in the system.

After the system reaches a steady state or no colour change is detected, the syringes stop flowing and the stopped flow regime begins. This is similar to a rate measurement which is taken with a UV-vis spectrometer. While the end value is of most importance to get a certain reading, there is information within the slope of the curve, and this will be measured, along with the value change. Hence the rate of change of reaction and the absorbance of the product itself will be measured (AA_n and dAA_n/dt). The system then switches off for a user determined time range before repeating again.

7.2.3 Input parameter effects

There are three components which are altered in the running of each of the regimes: u_{in}, c_{in} and u_{mean}.

7.2.4 Calibration

While there are multiple absorbance readings that were taken, they are all linked to the Beer-Lambert law. The equation used was:

$$A = \epsilon bc \tag{7.1}$$

Where ϵ is the molar attenuation coefficient, b is the path length through the absorption medium, and c is the concentration of the colorimetric complex, also the proxy concentration of the analyte. While this is the traditional form of the Beer-Lambert law, there is added complexity which may be inferred from the input parameters. The parameters ϵ and b are already known. A regression model can be produced, varying u_{in} and c_{in} as these have most influence on the developed colour, and u_{mean} has little impact on

this for a steady state flow. Equation (7.1) can then be redefined as:

$$A = \alpha_1 u_{in} + \alpha_2 c_{in} \tag{7.2}$$

The calibration is performed beforehand with known standards, before deployment where this is then run with unknown sample concentrations.

7.2.5 Equation

The estimation of the true absorbance value (and with using Equation (7.2)) is then determined with a multiple range of values. These are AA_{n-1}, AF_n, dAF_n/dt, $\hat{AA}_{n,end}$, dAA_n/dt, c_{in}, u_{in}, u_{mean}.

Sensor output & description

fault If the value is high, then there is an issue with the box itself, indicative of mechanical breakdown, leaking, third party damage etc.

$\mathbf{\bar{AA}_{n-1}}$ The fully developed colour from the previous run, corrective factor can be applied to previous run

$\mathbf{dAF_n/dt}$ The slope from when the previous run fluid has been fully emptied and can measure a hysteresis effect if any

$\mathbf{\bar{AF}_n}$ The steady state flow absorbance reading from flowing system, detect high pollutant concentration estimations

$\mathbf{dAA_n/dt}$ rate of colour development from the reaction for no flow, important for lower concentrations

$\mathbf{\hat{AA}_n}$ at end of run, best guess for true

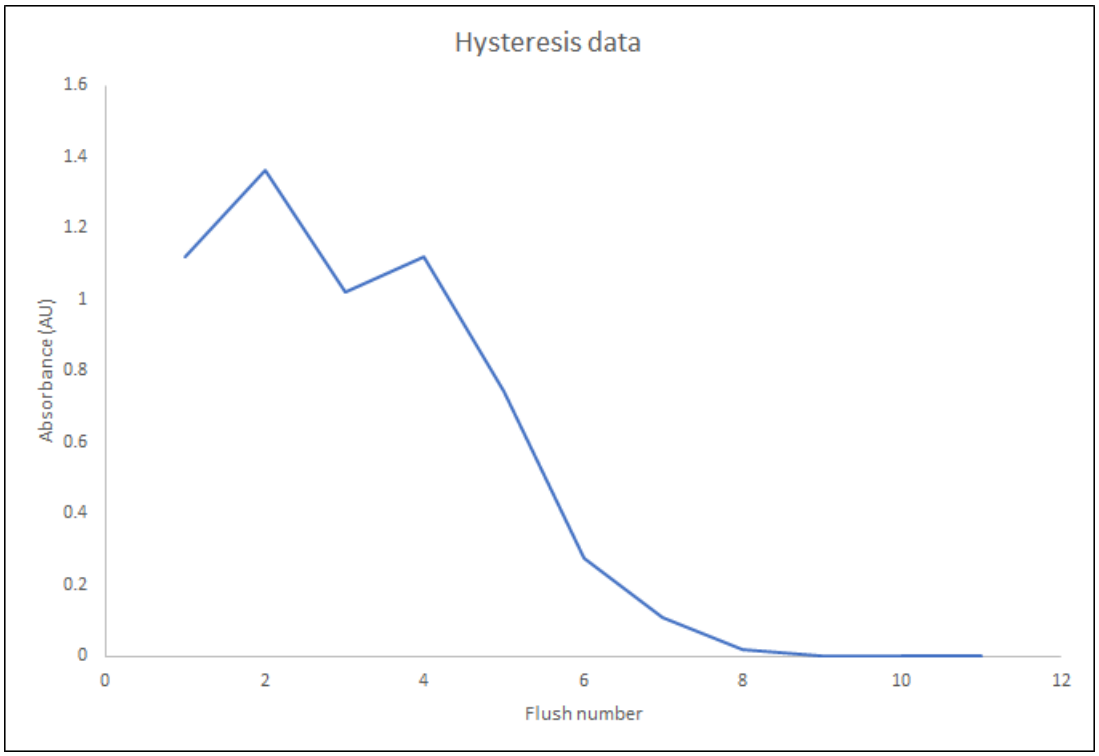

Figure 7.2: Results from the repeated flushing of a premixed solution using 1:1 DI water to reagent.

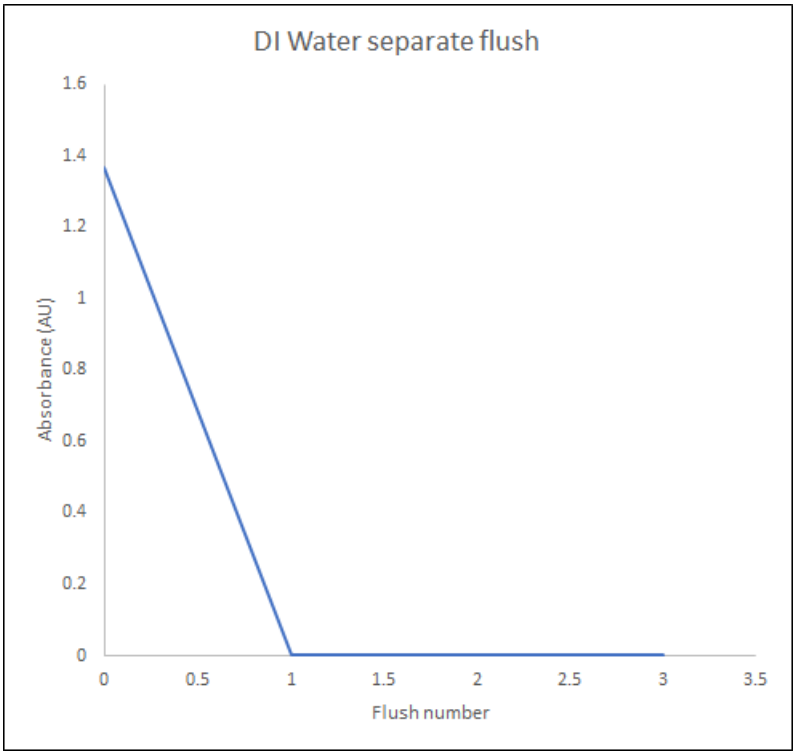

Figure 7.3: Change in absorbance after subsequent DI water flushes.

7.2.6 Results

The data in Figure 7.2 show that for the hysteresis effect, it took 9 flushes of a combination of DI water and reagent until there was a zero reading taken from the sensor. There was some noise present in initial runs. It was shown that it took a total of 9 runs until the solution was returning a blank reading. The immediate flushing of the system using DI water only in Figure 7.3 is in comparison to the gradual removal of the effect in Figure 7.2. This has implications for readings as an early warning detection system where an immediate change in the concentration to beyond regulated levels is important to be picked up. Also, pollution events may be missed as they may not be as pronounced on the sensor.

7.2.7 Altering run

The values of these also determine how the parameter values should be tuned to maximise sensitivity, to take advantage of fine-tuning to account for the aforementioned issues.

7.2.8 Increasing sensitivity

The sensitivity of the reactor can be changed by adjusting the input parameters u_{in} and u_{mean}. Decreasing u_{in} was found in the CFD simulations and the steady state experimental run to increase sensitivity for the PEDD. Hence these can be adjusted accordingly to account. Firstly, if possible it is better to reduce u_{in} first to conserve the amount of reagent that is being used. Secondly, when this cannot be reduced any more, then it is better to reduce u_{mean} to increase sensitivity. Te converse is true if one wants to reduce sensitivity, as may be the case when there is a pollution event recorded and detected.

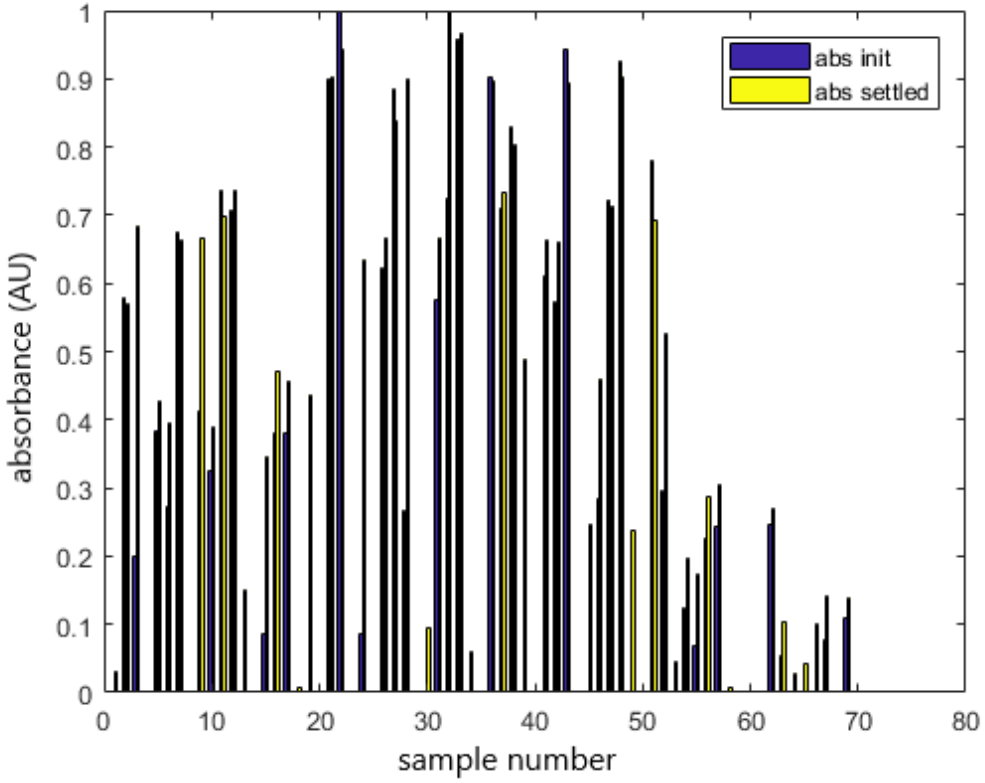

Figure 7.4: Bar chart showing the absorbance calculations from the stopped flow, accompanied by the finalised stopped flow obtained from the start of the next run.

7.2.9 Absorbance estimation

In between runs, there is more time for the colour to fully develop. This allows for a method in which the previous absorbance value, from the stopped flow, can be augmented to provide an update on the data collected. The data near the end of the run (the last 5 seconds) are averaged to produce the absorbance estimate value. The absorbance true value is derived from the start of the run, just after the LED is switched on, and just as the pumps start to inject the liquids into the system. This is taken as the median of the first 5 readings, as the first value can jump due to the system initialising.

It can be seen that for many of the runs that the values are similar. There is a good disparity between these then the absorbance estimate is near zero valued and the next estimate shows a reported absorbance. Such information can be seen in Figure 7.4. This is not a perfect approach, as due to the long time scale, there could be a number of factors which cause a change in the readings between runs. In the aforementioned data,

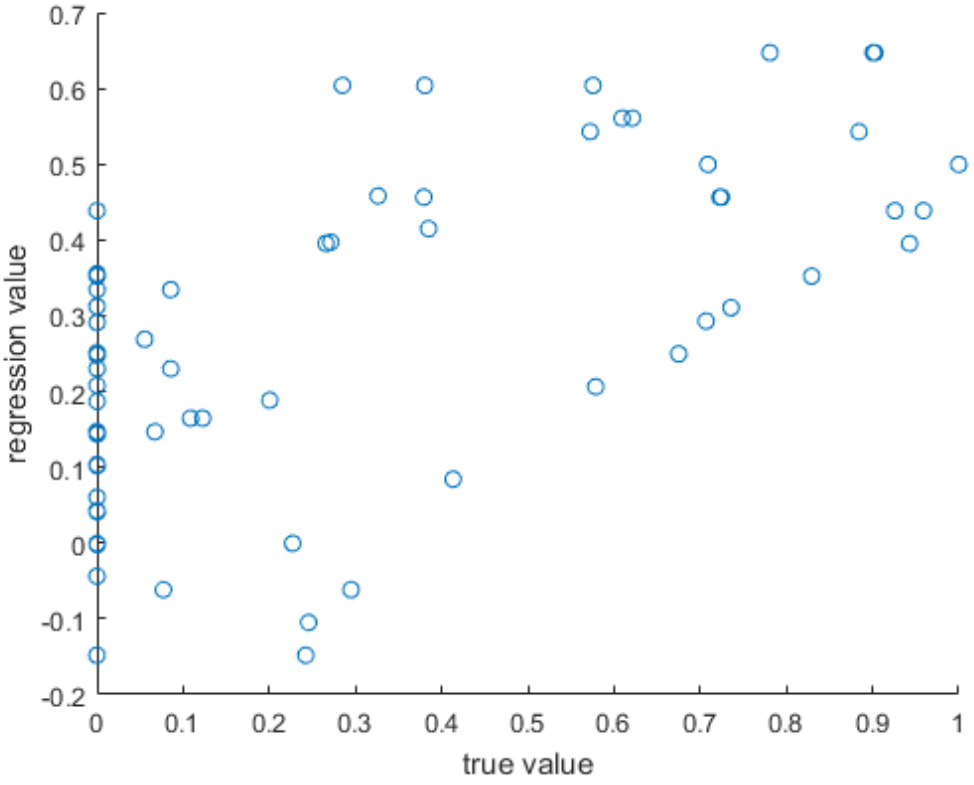

Figure 7.5: Simple regression using the $(c_{in}, u_{in}, u_{mean})$ values as parameters. The regression was poorly defined, and not suited to predicting the absorbance.

this sampling cycle is 40 minutes. Therefore, it is believed that this is better done when there is a negligible detection, and an initial reading just before the next run. Also, if the inputs were used as a simple parameterisation of the absorbance readings, these did not show enough consistency to be used as a predictive model for absorbance, as in Figure 7.5.

7.3 Staining

As there is some roughness on the PMMA surface, there is a risk of staining on the chip, which could affect some of the absorbance readings that are taken. Any effects of staining can be removed by using a mild organic solvent, such as NaOH, however there is a risk that repeated rinsing of the inner channels would damage the bonding between PMMA layers, irreversibly damaging the contained channels. A preferable approach is to account for this staining over time and see if there are any counteractions that may be taken (if any) which would minimise the impact of this effect.

7.3.1 Historical data

Historical data show that on longer term deployments there is an effect on the calibration standards. In a previous deployment, a colorimetric system was left to monitor nitrite levels at a freshwater site. The deployment took place over a period of 2 weeks. Included with the setup was calibration standards of 0 ppm and 3 ppm of each standard respectively. A sample was also taken to measure pollution levels in the water. To determine the interpolatable range which includes the blank and the 3 ppm standard as a range, then the equation becomes:

$$A_{range} = log_{10}V_{blank} - log_{10}V_{high} \tag{7.3}$$

Figure 7.6 shows the change in the sensitivity of the sensor over the deployment time. Absorbance range is plotted against time in hours, where 3 hours is the time taken for a full cycle to run, including high, blank and low standards. The absorbance range

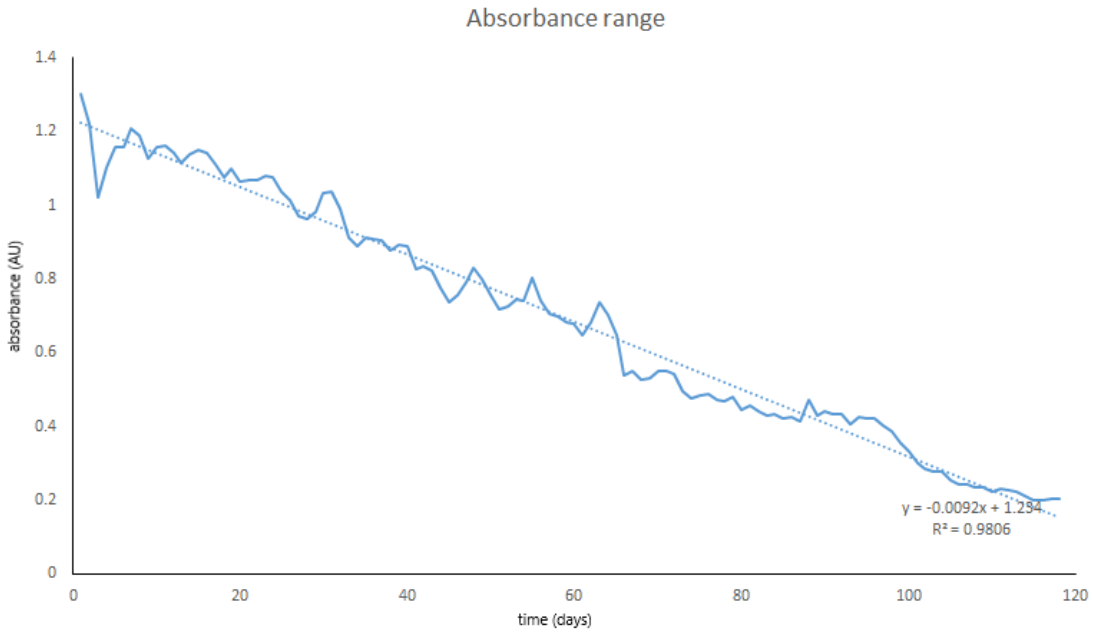

Figure 7.6: Decrease in the absorbance range for the sensor over an historical extended deployment period.

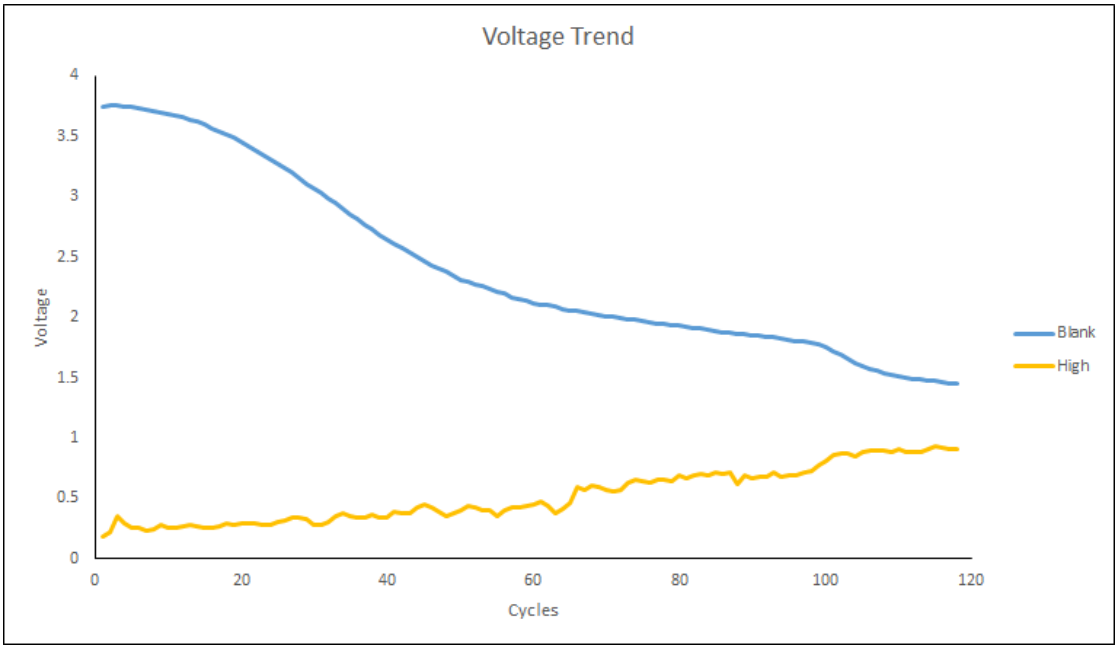

Figure 7.7: Voltage reading for each of the standards for each plot.

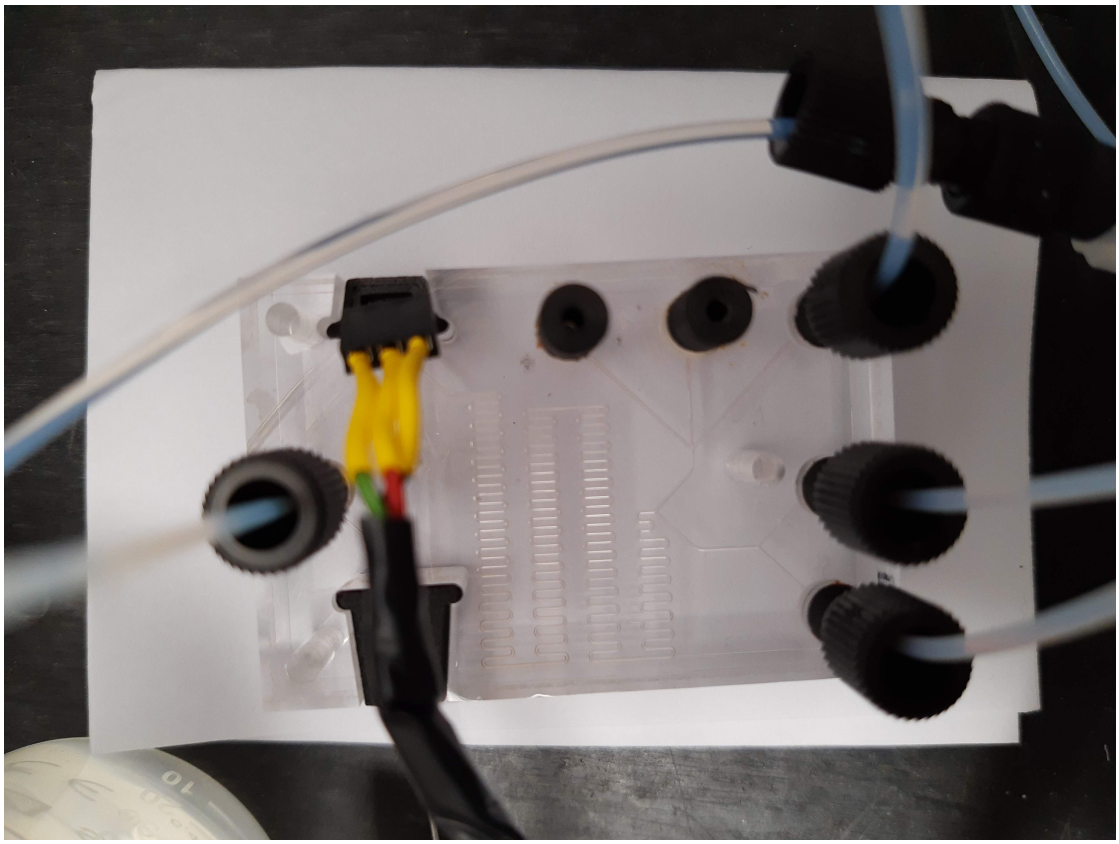

Figure 7.8: The microfluidic chip prior to staining.

was calculated using Equation (7.3). The separate voltage readings for the blank and high are in Figure 7.7. It can be seen that the blank reading deteriorates at a much higher rate than the standard, although the upwards high standard drift is more attributable to sensor drift rather than staining, as staining would make the high standard have a higher reading. The low voltage reading has been attributed to staining. For an initial maximum range (according to interpolation) of 1.234, the loss of range per cycle is roughly 0.92 mAU. Each cycle takes 3 runs of a blank, high and sample. Extrapolation to the x-axis suggests complete loss of sensitivity at 138 cycles, or 414 runs of the sensor. Therefore, it is important to monitor and correct for this to improve accuracy in the data collected.

7.3.2 Method

The Griess reaction solution, due to its vivid colour, was used to test for any staining effect.

A 20 ppm nitrite solution (beyond the linear range of the sensor) was introduced

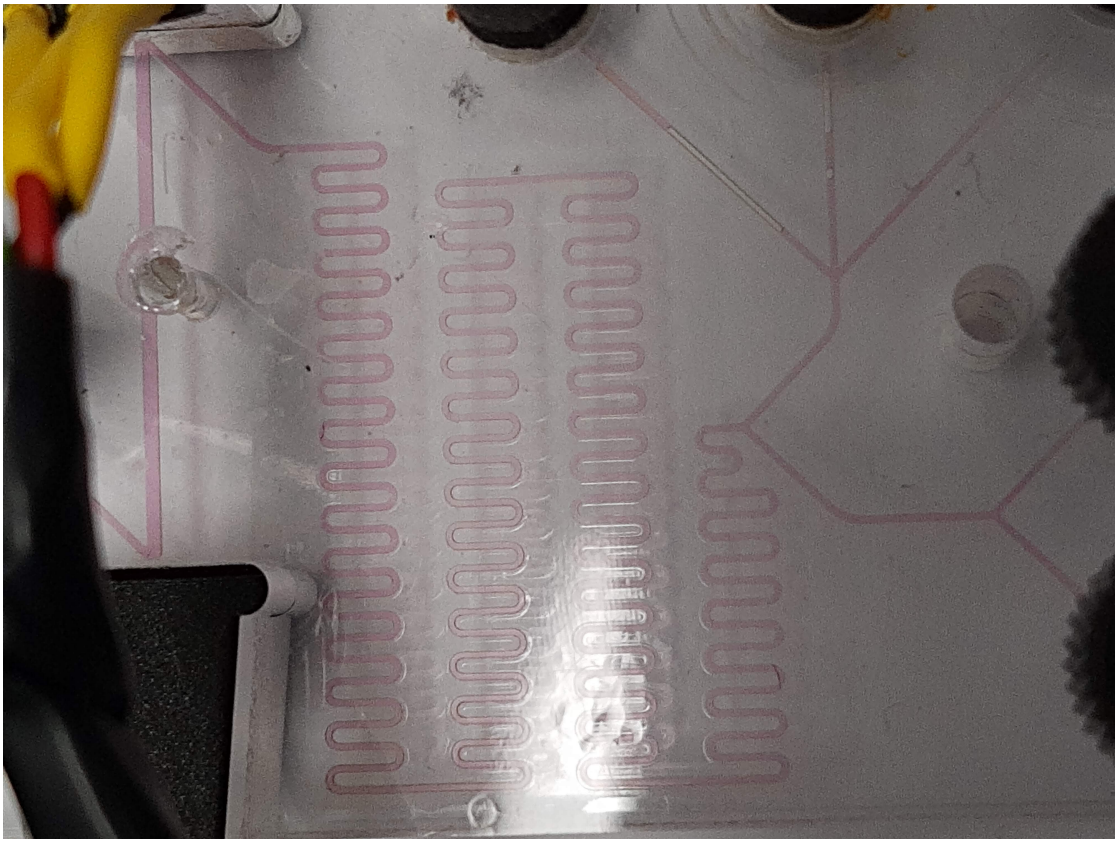

Figure 7.9: The microfluidic chip, with the 20 ppm solution suspended within the channels. This was left for a period of over 24 hours, far longer than would occur under normal operating procedures.

to the system (Figure 7.8) with an even mix of Griess reagent. $0.5\,\mathrm{mL}$ of each was entered into the system, as per Figure 7.9, and left for 24 hours. Aside from a subjective measure of whether or not there was residual colour within the channels, ImageJ was used to check for the pink-purple residue of the azo dye. This could be objectively measured using the imaging software though a histogram of the region of interest. The green and blue channels (in the presence of some purple colour) had a secondary peak shifted to the left. The right more peak was from the white/grey background, which has roughly an equal amplitude in all channels.

7.3.3 Results

The results of this showed no appreciable difference between the data collected before and after the staining attempt. Therefore there was no further collection of this data, as during deployment, any concentration CC produced in the channel would not reside in the detector channel any longer than the flushing cycle.

7.4 Conclusion

The sensor could be impacted by data collected from up to 8 previous cycles, meaning that hysteresis was a notable effect in concentration calculations during sensor operation. A methodology for using data collected between cycles could not be established as there was a poor correlation between input parameters and the absorbance from the start of a cycle and the end of a previous cycle. The attempted staining of the chip did not result in a notable change of colour after suspension for over 24 hours. As such a concentration would not be left in the chip during normal operation, it was determined that staining of the detector channel walls due to the colorimetric complex, and its interference, was negligible compared to hysteresis.

Chapter 8

Summary

8.1 Concluding remarks

The purpose of this research was to extend the lifetime of, improve the sensitivity and efficiency of, and to create a model of a colorimetric-based in-situ environmental sensor. The focus of the work completed was on the Griess reaction, a classical colorimetric assay, where there is a linear relationship between the concentration of nitrite and the light that the colorimetric complex absorbed.

Chapter 1 examined the state-of-the-art of microfluidic mixers, fabrication methods used for the production of microfluidic chips, as well as environmental sensors in use. It was found that there was a gap in the literature relating to the efficient use of passive mixers, employed as part of a low-cost sensor, which was the subject of the Nutrient Sensor Challenge. Examples of high efficient micromixers, namely the staggered herringbone mixer, are good at inducing turbulence in otherwise laminar flows, however the facilities required to manufacture these, as well as the cost, make them a prohibitive option at present for adoption in low-cost sensors. There is ample literature on active mixers and the use of complex micromixers, however there is little pertaining to optimising continuous flow sensors, which are the closest type of sensor at present which can be batch-produced. The operation of the Aquamontrix colorimetric sensor is discussed in Chapter 3

Chapter 2 is where an analytical approach was used, using first principles, to ob-

tain an equation that would account for a reacting convection-diffusion flow. It was determined that this was not possible due to the incorporation of reactions term into either Laplace domains or separated by variables equations. This meant that numerical solution was the most practical method to model the sensor.

The numerical modelling and simulation was outlined in Chapter 4, and the resulting data was used as the basis for a surrogate model for a multi-objective optimisation where the yield of the reaction (concentration of colorimetric complex) was maximised, where the quantity of unusued reagent was minimised. The results of the optimisation showed that where the inflow of reagent into the mixture comprises 5% - 7.5% of the total mixture solution, then the yield is maximised. Additionally, the reagent is minimised. This means that, operating the sensor using these paramater values as opposed to what is stated in Chapter 3 reduces reagent consumption by fivefold, while increasing sensitivity. A steady state study conducted in Chapter 5 confirms that this ratio of reagent increases colour development. It also showed that turbidity was not of great concern as an interferent, as the sensitivity of the sensor to this was much lower than the colorimetric complex. This was also true for the case of the presence of heavy metals in the test solution.

Chapter 6 set out to identify a model where the parameters of the simulation in Chapter 4 and output data from both simulated data (in the case of continuous flow data), as well as experimental data. Firstly, mechanistic models were identified using the convection-diffusion equations. Secondly, data-based models were identified for the continuous-flow data. This was shown to be a third-order model, where this could be reduced to a second-order model (of conjugate poles) and first-order model in parallel. A parameterisation of the coefficients of the models, using the input parameters, was also undertaken. It was found that using 3 principal components could account for the coefficients from the models. Thirdly, the stopped flow data – collected experimentally – underwent similar system identification. It was found that a second order model (reduced to 2 parallel first order models) was found as the best data-based model structure (using YIC as an indicator of this). This model is in keeping with the two-step structure

of the Griess reaction. This has allowed for the time best suited for recording a value as the absorbance value, selected as 20 minutes in Chapter 3.

Chapter 7 was the final chapter which looked at methods, using collected but previously unused data, to improve the accuracy of collected data. It was found that there was hysteresis due to carryover between runs of the sensor. The study in that chapter showed that at least 8 flushes was required to return the sensor to a zero-read for a blank solution. Staining was not found to be a significant factor for skewing readings compared to carryover.

For this reason there was time taken to create a custom code which focused solely on the laminar flow properties of the chip. The work completed in Chapter 4 was done using open source software created in Python. The consequences of creating a model entirely in Python allowed for extensive use of other packages which are freely available in Python to incorporate into the overall simulation, such as use of scikit-learn, which would not be immediately available in commercial CFD packages. It was also a concern as for small to medium enterprise which make up a large proportion of companies producing in-situ sensors, it would be prohibitive to have this software locked away in, for example, an expensive CFD package, which requires a high degree of training which would not be otherwise readily available.

The novelty of this research is that an extensive examination of a continuous flow colorimetric in-situ sensor has been conducted, improving its performance as a result. This has permitted the characterisation of the sensor, facilitating the identification of operating parameters which has extended the maximum deployment time while also increasing sensitivity. The output of the sensor for both the continuous and stopped flow phases has also been characterisied, identifying a third order and second order model respectively. Additionally, the known deleterious effects have been evaulated and, as opposed to staining or turbidity, that carryover was a significant factor in the reading calculated by the sensor.

8.1.1 Limitations

There were some limitations with the sensor, most notably the side effects of some of the inexpensive components included in the box, for example the brush motors, which limit how slow the flow can operate which was identified as a key factor in improving sensor sensitivity. A slower flow and a smaller sample to reagent ratio were key to preserving reagent and extending lifetime. The flow data captured from the experimental data were difficult to infer information from regarding the concentration due to the poor sensitivity, and that noise far exceeded any tangible information on the underlying trend if present. The simulated data was the only approach that could be used for this, although it was identified that there was a dominant first order TF which fitted the data, although it was not trivial to show exactly how the inputs could be attributed to the output of the model. It was difficult to visually inspect the inner workings of the chip due to the enclosed, sealed nature of the microfluidic chip. Making the chip opaque or semi-opaque renders visual inspection of the chip difficult. One of the sacrifices which had to be made during this research, was to use of fully transparent chips which allowed for ease of manufacturing and examination of the internal workings of the chip, and also to monitor development of staining within the chip, which was believed at stages to have an adverse effect on the sensitivity in the detector channel overtime. However, it was found that there was not a significant accumulation in the laboratory-tested chip, although no environmental waters were used, which is suspected of causing the staining issue, rather than colorimetric complex. In other studies mentioned in Chapter 1, there is use of either fully opaque or semi-opaque media. This allows for the mitigation of stray lights which greatly improves the sensitivity readings which are taken from the detector channel.

8.2 Future work

Future aspects of this work would include incorporating other reactions which are used, for example, the arsenic methods which is more prevalent in South Asia. The reaction

times and sensor flow rates can be identified to find the underlying reaction, and again an examination of the known interferants provides a basis for calibration. There is also potential to incorporate an in-built dilution system, allowing for on-demand standards fabricated from an on-board stock solution and DI water. This has the advantage of increased standard stability, as the stock solution has a longer lifetime than standards of similar levels to environmental waters. The implications of this research are not only found in the in-situ water sensor fields, but also in areas such as green chemistry, where the objective is a reduction of harmful waste or the use of hazardous reagents in the reaction. Additionally, in other fields such as production of nanoparticles, there is great interest in precise use of such reagents, where there is not a large financial burden on the large amount of storage for such products, but some nanoparticle reagents are quite scarce, hence it is of great interest as this would preserve limited resources.

Appendix A

INO file for microcontroller

```
#include <avr/io.h>
#include <avr/interrupt.h>
#include "PumpControl.h"
#include "SampleSequence.h"
#include "DataHandling.h"
#include "RTCTime.h"
#include "GSMControl.h"
#include "IOPins.h"
#include <Snooze.h>

////////////////////////////////////////////////////////////////////
////////////////////// Teensy sleep mode setup ////////////////////////////
////////////////////////////////////////////////////////////////////

SnoozeDigital digital;
SnoozeBlock config1(digital);

////////////////////////////////////////////////////////////////////
//////////////////////////// Variables ////////////////////////////////
////////////////////////////////////////////////////////////////////
```

```
// used in loop function
int runOnce = 0; // runOnce ensures the sequence programmed in SampleSequence.cpp only
    ↪ runs once when the system wakes up.
const unsigned int intval = 40*60; // sampling time interval (s)
int runs = 320; // start with lowest speed & ratio setting
const int flowTestBins = 5;
const int speedTestBins = 3;
int wake1;
int sampleFlowReagent, flowCase, flowRate, speedCase, speedRate;
float flowRatio;

////////////////////////////////////////////////////////////////////
////////////////////// Setup Function //////////////////////////////
////////////////////////////////////////////////////////////////////

void setup()
{
  digital.pinMode(RTC_ALM, INPUT_PULLUP, FALLING); //Set up RTC Pin sleep interrupt
  digital.pinMode(PUSH_BTN, INPUT_PULLUP, FALLING); ////Set up Push Button Pin
      ↪ sleep interrupt

  // LED Setup
  pinMode(LED_PWM, OUTPUT); // Detector LED PWM pin set as output
  analogWrite(LED_PWM, LOW); // LED PWM set to low (LED off)

  // Sample Pump Setup
  pinMode(SMPL_PMP, OUTPUT); // Sample Pump relay pin set as output
  digitalWrite(SMPL_PMP, LOW); // Sample Pump pin set to low (Relay off)

  // Motor Controller Setup
  pinMode(MC1_STBY, OUTPUT); // Motor Controller 1 standby pin set as output
```

```
pinMode(MC2_STBY, OUTPUT);
pinMode(MC3_STBY, OUTPUT);
digitalWrite(MC1_STBY, LOW); // Motor Controller 1 standby pin set to low (Motor
    ↪ Controller 1 off)
digitalWrite(MC2_STBY, LOW);
digitalWrite(MC3_STBY, LOW);

//Setup interrupts for each motor encoder
pinMode(ENCDR_1 , INPUT); // Encoder 1 pin set as input
pinMode(ENCDR_2 , INPUT);
pinMode(ENCDR_3 , INPUT);
pinMode(ENCDR_4 , INPUT);

attachInterrupt(digitalPinToInterrupt(ENCDR_1), readEncoder1, RISING); // Set up
    ↪ interrupt on rising edge on encoder 1 pin (counter for PID loop)
attachInterrupt(digitalPinToInterrupt(ENCDR_2), readEncoder2, RISING);
attachInterrupt(digitalPinToInterrupt(ENCDR_3), readEncoder3, RISING);
attachInterrupt(digitalPinToInterrupt(ENCDR_4), readEncoder4, RISING);

Serial.begin(9600); // Begin serial communications

delay(10000); // 10 Second delay allows Teensy 3.6 to be reprogrammed before going to
    ↪ sleep

// Syringe Pump setup
pump1Setup(); // Sets the required pins for Syringe Pump 1
pump2Setup();
pump3Setup();
pump4Setup();

gsmSetup(); // Set up mosfet pin to turn GSM modem on/off
```

```
  rtcSetup(); // Sets interrupt pin for RTC and starts clock
  dataHandlingSetup(); // Setup ADC & SD card

  //rtcAlarm(3600);
  //runSequence();
}

////////////////////////////////////////////////////////////////////
//////////////////////////// Main Loop ////////////////////////////////
////////////////////////////////////////////////////////////////////

void loop()
{
  //int wake1; // Variable used in sleep function
  wake1 = Snooze.hibernate(config1); // This line puts the system to sleep

  /*if(wake1 == PUSH_BTN) // If the push button is pressed, wake the system
  {
    runSequence(); // Run the sequence programmed in SampleSequence.cpp when the push
        ↪ button is pressed
  }*/

  flowCase = runs % flowTestBins;
  flowCase = flowCase + 1; // changes range from 1:flowTestBins
  //flowRate = 30; // this is based on encoder value
  flowRatio = flowCase * (0.5 / flowTestBins); // phrased to eliminate casting

  speedCase = runs % speedTestBins;
  speedCase = speedCase+1;
  flowRate = speedCase * (31 / speedTestBins);
```

```
  if(wake1 == PUSH_BTN) // If the push button is pressed, wake the system
  {
    if (runOnce == 0)
    {
      runOnce = 1;
      rtcAlarm(intval);
      runSequence(flowRatio, flowRate); // Run the sequence programmed in
          ↪ SampleSequence.cpp when the push button is pressed
      runs--;
    }
  }

  if (wake1 == RTC_ALM) // If RTC alarm goes off, wake the system
  {
    if (runs > 0)
    {
      rtcAlarm(intval); // Set the RTC alarm to wake system for next sample
      runSequence(flowRatio, flowRate); // Run the sampling sequence
      runs--;
    }
  }
}

////////////////////////////////////////////////////////////////////////
////////////////////////////////////////////////////////////////////////
////////////////////////////////////////////////////////////////////////
```

List of references

[1] G. Kallis and D. Butler. The EU water framework directive: measures and implications. *Water policy*, 3(2):125–142, 2001.

[2] D. Cogan, J. Cleary, C. Fay, A. Rickard, K. Jankowski, T. Phelan, M. Bowkett, and D. Diamond. The development of an autonomous sensing platform for the monitoring of ammonia in water using a simplified berthelot method. *Analytical Methods*, 6(19):7606–7614, 2014.

[3] D. Cogan, C. Fay, D. Boyle, C. Osborne, N. Kent, J. Cleary, and D. Diamond. Development of a low cost microfluidic sensor for the direct determination of nitrate using chromotropic acid in natural waters. *Analytical Methods*, 7(13): 5396–5405, 2015. ISSN 1759-9660. doi: 10.1039/C5AY01357G.

[4] M. McCaul, J. Barland, J. Cleary, C. Cahalane, T. McCarthy, and D. Diamond. Combining Remote Temperature Sensing with in-Situ Sensing to Track Marine/-Freshwater Mixing Dynamics. *Sensors*, 16(9):1402, 2016.

[5] L. Chatzidiakou, A. Krause, O. A. M. Popoola, A. Di Antonio, M. Kellaway, Y. Q. Han, F. A. Squires, T. Wang, H. B. Zhang, Q. Wang, Y. F. Fan, S. Y. Chen, M. Hu, J. K. Quint, B. Barratt, F. J. Kelly, T. Zhu, and R. L. Jones. Characterising low-cost sensors in highly portable platforms to quantify personal exposure in diverse environments. *Atmospheric Measurement Techniques*, 12(8):4643–4657, 2019. ISSN 1867-1381. doi: 10.5194/amt-12-4643-2019.

[6] T. Atkins and M. Escudier. multiphase flow, 2013.

[7] G. M. Whitesides. The origins and the future of microfluidics. *Nature*, 442 (7101):368, 2006.

[8] J. Berthier. *Micro-drops and digital microfluidics*. William Andrew, 2012.

[9] J. Atencia and D. J. Beebe. Controlled microfluidic interfaces. *Nature*, 437 (7059):648–655, 2005.

[10] M. Koch. Microfluidic devices II: Particles and chemistry. In A. Evans and A. Brunnschweiler, editors, *Microfluidic technology and applications*. Research Studies Press, 2000.

[11] W. Jung, J. Han, J.-W. Choi, and C. H. Ahn. Point-of-care testing (poct) diagnostic systems using microfluidic lab-on-a-chip technologies. *Microelectronic Engineering*, 132:46–57, 2015.

[12] P. N. Nge, C. I. Rogers, and A. T. Woolley. Advances in microfluidic materials, functions, integration, and applications. *Chemical reviews*, 113(4):2550–2583, 2013.

[13] W. E. Eric, B. Anthony, and H. Dongeun. Organs-on- chips at the frontiers of drug discovery. *Nature Reviews Drug Discovery*, 14(4):248, 2015. ISSN 1474-1776. doi: 10.1038/nrd4539.

[14] S. N. Bhatia and D. E. Ingber. Microfluidic organs-on-chips. *Nature biotechnology*, 32(8):760, 2014.

[15] S. G. Kandlikar and W. J. Grande. Evolution of microchannel flow passages–thermohydraulic performance and fabrication technology. *Heat Transfer Engineering*, 24(1):3–17, 2003. ISSN 0145-7632. doi: 10.1080/01457630304040.

[16] C. S. Andreasen, A. R. Gersborg, and O. Sigmund. Topology optimization of microfluidic mixers. *International Journal for Numerical Methods in Fluids*, 61 (5):498–513, 2009.

[17] D. Bothe, C. Stemich, and H. J. Warnecke. Fluid mixing in a T-shaped micromixer. *Chemical Engineering Science*, 61(9):2950–2958, 2006. doi: 10.1016/j.ces.2005.10.060.

[18] C.-Y. Lee, C.-L. Chang, Y.-N. Wang, and L.-M. Fu. Microfluidic mixing: a review. *International Journal of Molecular Sciences*, 12(5):3263–3287, 2011.

[19] X. Niu and Y.-K. Lee. Efficient spatial-temporal chaotic mixing in microchannels. *Journal of Micromechanics and Microengineering*, 13(3):454, 2003.

[20] L. H. Olesen, F. Okkels, and H. Bruus. A high-level programming-language implementation of topology optimization applied to steady-state navier–stokes flow. *International Journal for Numerical Methods in Engineering*, 65(7):975–1001, 2006.

[21] X. Shi, Y. Xiang, L. X. Wen, and J. F. Chen. Cfd analysis of flow patterns and micromixing efficiency in a y-type microchannel reactor. *Industrial & Engineering Chemistry Research*, 51(43):13944–13952, 2012. ISSN 0888-5885. doi: 10.1021/ie300985q.

[22] N.-T. Nguyen and Z. Wu. Micromixers—a review. *Journal of Micromechanics and Microengineering*, 15(2):R1, 2004.

[23] T. J. Ober, D. Foresti, and J. A. Lewis. Active mixing of complex fluids at the microscale. *Proceedings of the National Academy of Sciences*, 112(40):12293–12298, 2015.

[24] A. S. Athulya and R. Miji Cherian. CFD Modelling of Multiphase Flow through T-Junction. *Procedia Technology*, 24:325–331, 2016. ISSN 2212-0173. doi: 10.1016/j.protcy.2016.05.043.

[25] C. A. Cortes-Quiroz, A. Azarbadegan, and M. Zangeneh. Effect of channel aspect ratio of 3-D T-mixer on flow patterns and convective mixing for a wide range of Reynolds number. *Sensors and Actuators B: Chemical*, 239:1153–1176, 2017. ISSN 0925-4005. doi: http://dx.doi.org/10.1016/j.snb.2016.08.116.

[26] M. Hoffmann, M. Schlüter, and N. Räbiger. Experimental investigation of liquid-liquid mixing in t-shaped micro-mixers using micro-lif and micro-piv. *Chemical Engineering Science*, 61(9):2968–2976, 2006. doi: 10.1016/j.ces.2005.11.029.

[27] A. V. Minakov, V. Y. Rudyak, A. A. Gavrilov, and A. A. Dekterev. Mixing in a t-shaped micromixer at moderate reynolds numbers. *Thermophysics and Aeromechanics*, 19(3):385–395, 2012. doi: 10.1134/S0869864312030043.

[28] S. H. Wong, M. C. L. Ward, and C. W. Wharton. Micro t-mixer as a rapid mixing micromixer. *Sensors and Actuators, B: Chemical*, 100(3):359–379, 2004. doi: 10.1016/j.snb.2004.02.008.

[29] B. Xu, T. N. Wong, N. T. Nguyen, Z. Che, and J. C. K. Chai. Thermal mixing of two miscible fluids in a t-shaped microchannel. *Biomicrofluidics*, 4(4), 2010. doi: 10.1063/1.3496359.

[30] D. Di Carlo. Inertial microfluidics. *Lab on a Chip*, 9(21):3038–3046, 2009.

[31] S. S. Das, S. D. Tilekar, S. S. Wangikar, and P. K. Patowari. Numerical and experimental study of passive fluids mixing in micro-channels of different configurations. *Microsystem Technologies*, 23(12):5977–5988, 2017.

[32] W. Raza, S. B. Ma, and K. Y. Kim. Multi-objective optimizations of a serpentine micromixer with crossing channels at low and high reynolds numbers. *Micromachines*, 9(3), 2018. ISSN 2072-666x. doi: ARTN11010.3390/mi9030110.

[33] D. S. Kim, S. H. Lee, T. H. Kwon, and C. H. Ahn. A serpentine laminating micromixer combining splitting/recombination and advection. *Lab on a Chip*, 5 (7):739–747, 2005. ISSN 1473-0197. doi: 10.1039/B418314B.

[34] H. M. Xia, S. Y. M. Wan, C. Shu, and Y. T. Chew. Chaotic micromixers using two-layer crossing channels to exhibit fast mixing at low reynolds numbers. *Lab on a Chip*, 5(7):748–755, 2005. ISSN 1473-0197. doi: 10.1039/B502031J.

[35] A. D. Stroock, S. K. W. Dertinger, A. Ajdari, I. Mezic, H. A. Stone, and G. M. Whitesides. Chaotic mixer for microchannels. *Science*, 295(5555):647–651, 2002. ISSN 0036-8075. doi: DOI10.1126/science.1066238.

[36] J. H. Kim, K. T. Lau, R. Shepherd, Y. Wu, G. Wallace, and D. Diamond. Performance characteristics of a polypyrrole modified polydimethylsiloxane (pdms) membrane based microfluidic pump. *Sensors and Actuators A: Physical*, 148 (1):239–244, 2008. ISSN 0924-4247. doi: https://doi.org/10.1016/j.sna.2008.07.029.

[37] H. Kido, J. Zoval, and M. J. Madou. Rapid prototyping of microfludic systems. *ECS Transactions*, 4(1):101–105, 2007.

[38] X. Ku, Z. Zhang, X. Liu, L. Chen, and G. Li. Low-cost rapid prototyping of glass microfluidic devices using a micromilling technique. *Microfluidics and Nanofluidics*, 22(8):82, 2018. ISSN 1613-4990. doi: 10.1007/s10404-018-2104-y.

[39] G. S. Clinton-Bailey, M. M. Grand, A. D. Beaton, A. M. Nightingale, D. R. Owsianka, G. J. Slavikt, D. P. Connelly, C. L. Cardwell, and M. C. Mowlem. A lab-on-chip analyzer for in situ measurement of soluble reactive phosphate: Improved phosphate blue assay and application to fluvial monitoring. *Environmental Science & Technology*, 51(17):9989–9995, 2017. ISSN 0013-936x. doi: 10.1021/acs.est7b01581.

[40] M. M. Grand, G. S. Clinton-Bailey, A. D. Beaton, A. M. Schaap, T. H. Johengen, M. N. Tamburri, D. P. Connelly, M. C. Mowlem, and E. P. Achterberg. A lab-on-chip phosphate analyzer for long-term in situ monitoring at fixed observatories: optimization and performance evaluation in estuarine and oligotrophic coastal waters. *Frontiers in Marine Science*, 4:255, 2017.

[41] M. N. Kashid, D. W. Agar, and S. Turek. Cfd modelling of mass transfer with and without chemical reaction in the liquid–liquid slug flow microreactor. *Chemical*

Engineering Science, 62(18):5102–5109, 2007. ISSN 0009-2509. doi: https://doi.org/10.1016/j.ces.2007.01.068.

[42] A. Paster, T. Aquino, and D. Bolster. Incomplete mixing and reactions in laminar shear flow. *Physical Review E*, 92(1), 2015. ISSN 1539-3755. doi: 10.1103/PhysRevE.92.012922.

[43] L. Zhang, Y. N. Guo, J. C. Yan, Q. Q. Wu, X. C. Wei, J. X. Wang, and J. M. Li. Deep ultraviolet light-emitting diodes with improved performance via nanoporous algan template. *Optics Express*, 27(4):4917–4926, 2019. ISSN 1094-4087. doi: 10.1364/Oe.27.004917.

[44] F. J. Wang, J. P. Huang, and J. H. Xu. Continuous-flow synthesis of the azo pigment yellow 14 using a three-stream micromixing process. *Organic Process Research and Development*, 23(12):2637–2646, 2019. ISSN 10836160 (ISSN). doi: 10.1021/acs.oprd.9b00286.

[45] F. J. Wang, Y. C. Ding, and J. H. Xu. Continuous-flow synthesis of pigment red 146 in a microreactor system. *Industrial and Engineering Chemistry Research*, 58(36):16338–16347, 2019. ISSN 08885885 (ISSN). doi: 10.1021/acs.iecr.9b03045.

[46] K. S. Johnson, C. M. Sakamoto-Arnold, and C. L. Beehler. Continuous determination of nitrate concentrations in situ. *Deep Sea Research Part A, Oceanographic Research Papers*, 36(9):1407–1413, 1989. ISSN 01980149 (ISSN). doi: 10.1016/0198-0149(89)90091-5.

[47] I. M. P. D. Sansalvador, C. D. Fay, J. Cleary, A. M. Nightingale, M. C. Mowlem, and D. Diamond. Autonomous reagent-based microfluidic ph sensor platform. *Sensors and Actuators B-Chemical*, 225:369–376, 2016. ISSN 0925-4005. doi: 10.1016/j.snb.2015.11.057.

[48] A. M. Nightingale, S. U. Hassan, B. M. Warren, K. Makris, G. W. H. Evans, E. Papadopoulou, S. Coleman, and X. Z. Niu. A droplet microfluidic-based

sensor for simultaneous in situ monitoring of nitrate and nitrite in natural waters. *Environmental Science & Technology*, 53(16):9677–9685, 2019. ISSN 0013-936x. doi: 10.1021/acs.est.9b01032.

[49] R. Pol, F. Céspedes, D. Gabriel, and M. Baeza. Microfluidic lab-on-a-chip platforms for environmental monitoring. *TrAC Trends in Analytical Chemistry*, 95: 62–68, 2017. ISSN 0165-9936. doi: https://doi.org/10.1016/j.trac.2017.08.001.

[50] H. Chengfang, X. Xiao, S. Dingtao, C. Bo, and W. Xiongfei. Study of water pollution early warning framework based on internet of things. *International Archives of the Photogrammetry, Remote Sensing and Spatial Information Sciences*, 8(5):335–338, 2016.

[51] A. Donohoe, G. Lacour, P. McCluskey, D. Diamond, and M. McCaul. Development of a cost-effective sensing platform for monitoring phosphate in natural waters. *Chemosensors*, 6(4), 2018. ISSN 22279040 (ISSN). doi: 10.3390/chemosensors6040057.

[52] A. Lace, D. Ryan, M. Bowkett, and J. Cleary. Arsenic detection in water using microfluidic detection systems based on the leucomalachite green method. *Analytical Methods*, 11(42):5431–5438, 2019. ISSN 1759-9660. doi: 10.1039/c9ay01580a.

[53] A. Milani, P. J. Statham, M. C. Mowlem, and D. P. Connelly. Development and application of a microfluidic in-situ analyzer for dissolved fe and mn in natural waters. *Talanta*, 136:15–22, 2015. ISSN 0039-9140. doi: https://doi.org/10.1016/j.talanta.2014.12.045.

[54] V. J. Sieben, C. F. Floquet, I. R. Ogilvie, M. C. Mowlem, and H. Morgan. Microfluidic colourimetric chemical analysis system: Application to nitrite detection. *Analytical Methods*, 2(5):484–491, 2010.

[55] E. Taylor, J. Bonner, R. Nelson, C. Fuller, W. Kirkey, and S. Cappelli. Develop-

ment of an in-situ total phosphorus analyzer. *Oceans 2015 - Mts/Ieee Washington*, 2015. ISSN 0197-7385.

[56] V. M. Rérolle, C. F. Floquet, A. J. Harris, M. C. Mowlem, R. R. Bellerby, and E. P. Achterberg. Development of a colorimetric microfluidic ph sensor for autonomous seawater measurements. *Analytica Chimica Acta*, 786:124 – 131, 2013. ISSN 0003-2670. doi: https://doi.org/10.1016/j.aca.2013.05.008.

[57] K. S. Johnson, H. W. Jannasch, L. J. Coletti, V. A. Elrod, T. R. Martz, Y. Takeshita, R. J. Carlson, and J. G. Connery. Deep-sea durafet: A pressure tolerant ph sensor designed for global sensor networks. *Analytical Chemistry*, 88(6):3249–3256, 2016. ISSN 00032700 (ISSN). doi: 10.1021/acs.analchem.5b04653.

[58] S. M. da Silva and L. H. Mazo. Differential pulse voltammetric determination of nitrite with gold ultramicroelectrode. *Electroanalysis*, 10(17):1200–1203, 1998. ISSN 1040-0397. doi: Doi10.1002/(Sici)1521-4109(199811)10:17⟨1200::Aid-Elan1200⟩3.0.Co;2-5.

[59] R. J. Davenport and D. C. Johnson. Voltammetric determination of nitrate and nitrite ions using a rotating cadmium disk electrode. *Analytical Chemistry*, 45 (11):1979–1980, 1973. ISSN 0003-2700. doi: DOI10.1021/ac60333a038.

[60] H. Hara and S. Kusu. Continuous-flow determination of phosphate using a lead ion-selective electrode. *Analytica Chimica Acta*, 261(1-2):411–417, 1992. ISSN 0003-2670. doi: Doi10.1016/0003-2670(92)80221-R.

[61] J. Jońca, V. León Fernández, D. Thouron, A. Paulmier, M. Graco, and V. Garçon. Phosphate determination in seawater: Toward an autonomous electrochemical method. *Talanta*, 87(1):161–167, 2011. ISSN 00399140 (ISSN). doi: 10.1016/j.talanta.2011.09.056.

[62] A. M. Nightingale, S.-u. Hassan, G. W. H. Evans, S. M. Coleman, and X. Z. Niu. Nitrate measurement in droplet flow: gas-mediated crosstalk and correction. *Lab on a Chip*, 18(13):1903–1913, 2018. ISSN 1473-0197. doi: 10.1039/c8lc00092a.

[63] M. Bowden and D. Diamond. The determination of phosphorus in a microfluidic manifold demonstrating long-term reagent lifetime and chemical stability utilising a colorimetric method. *Sensors & Actuators: B. Chemical*, 90(1):170–174, 2003. ISSN 0925-4005. doi: 10.1016/S0925-4005(03)00024-8.

[64] R. Dreyfus, P. Tabeling, and H. Willaime. Ordered and disordered patterns in two-phase flows in microchannels. *Physical review letters*, 90(14):144505, 2003.

[65] H. Song, D. L. Chen, and R. F. Ismagilov. Reactions in droplets in microfluidic channels. *Angewandte chemie international edition*, 45(44):7336–7356, 2006.

[66] H. Song, M. R. Bringer, J. D. Tice, C. J. Gerdts, and R. F. Ismagilov. Experimental test of scaling of mixing by chaotic advection in droplets moving through microfluidic channels. *Applied Physics Letters*, 83(22):4664–4666, 2003.

[67] A. R. Sastri, J. R. Christian, E. P. Achterberg, D. Atamanchuk, J. J. H. Buck, P. Bresnahan, P. J. Duke, W. Evans, S. F. Gonski, B. Johnson, S. K. Juniper, S. Mihaly, L. A. Miller, M. Morley, D. Murphy, S. I. Nakaoka, T. Ono, G. Parker, K. Simpson, and T. Tsunoda. Perspectives on in situ sensors for ocean acidification research. *Frontiers in Marine Science*, 6, 2019. ISSN 22967745 (ISSN). doi: 10.3389/fmars.2019.00653.

[68] P. L. Suryawanshi, S. P. Gumfekar, B. A. Bhanvase, S. H. Sonawane, and M. S. Pimplapure. A review on microreactors: Reactor fabrication, design, and cutting-edge applications. *Chemical Engineering Science*, 189:431–448, 2018. ISSN 0009-2509. doi: https://doi.org/10.1016/j.ces.2018.03.026.

[69] T. Glennon, C. O'Quigley, M. McCaul, G. Matzeu, S. Beirne, G. G. Wallace, F. Stroiescu, N. O'Mahoney, P. White, and D. Diamond. 'sweatch': A wearable platform for harvesting and analysing sweat sodium content. *Electroanalysis*, 28 (6):1283–1289, 2016. ISSN 1040-0397. doi: 10.1002/elan.201600106.

[70] V. C. Pinto, C. F. Araújo, P. J. Sousa, L. M. Gonçalves, and G. Minas. A low-cost lab-on-a-chip device for marine ph quantification by colorimetry. *Sensors*

and Actuators B: Chemical, 290:285–292, 2019. ISSN 0925-4005. doi: https://doi.org/10.1016/j.snb.2019.03.098.

[71] A. Kämpfer, R. La Spina, D. Gilliland, S. Valzacchi, D. Asturiol, V. Stone, and A. Kinsner-Ovaskainen. Silver Nanoparticles and Metallic Silver Interfere with the Griess Reaction: Reduction of Azo Dye Formation via a Competing Sandmeyer-Like Reaction. *Chemical Research in Toxicology*, 30(4):1030–1037, 2017. ISSN 0893-228X. doi: 10.1021/acs.chemrestox.6b00280.

[72] S. Blomqvist, K. Hjellström, and A. Sjösten. Interference from arsenate, fluoride and silicate when determining phosphate in water by the phosphoantimonylmol ybdenum blue method. *International Journal of Environmental Analytical Chemistry*, 54(1):31–43, 1993. ISSN 0306-7319. doi: 10.1080/03067319308044425.

[73] D. Fanelli. How many scientists fabricate and falsify research? a systematic review and meta-analysis of survey data. *PLOS ONE*, 4(5):e5738, 2009. doi: 10.1371/journal.pone.0005738.

[74] P. Young. Data-based mechanistic modelling of environmental, ecological, economic and engineering systems. *Environmental Modelling & Software*, 13(2): 105–122, 1998.

[75] P. Young. Data-based mechanistic modelling and validation of rainfall-flow processes. *Model validation: perspectives in hydrological science*, pages 117–161, 2001.

[76] P. Young. Top-down and data-based mechanistic modelling of rainfall–flow dynamics at the catchment scale. *Hydrological processes*, 17(11):2195–2217, 2003.

[77] A. R. Schor. A method for approximating and controlling the distributed parameter model of a mimo chemical diffusion system. Master's thesis, Massachusetts Institute of Technology, 2010.

[78] P. K. Sahu, A. Golia, and A. K. Sen. Analytical, numerical and experimental investigations of mixing fluids in microchannel. *Microsystem Technologies-Micro-*

and Nanosystems-Information Storage and Processing Systems, 18(6):823–832, 2012. ISSN 0946-7076. doi: 10.1007/s00542-012-1511-3.

[79] J. B. Fox Jr. Kinetics and mechanisms of the griess reaction. *Analytical Chemistry*, 51(9):1493–1502, 1979. ISSN 00032700.

[80] J. H. Margeson, J. C. Suggs, and M. R. Midgett. Reduction of nitrate to nitrite with cadmium. *Analytical Chemistry*, 52(12):1955–1957, 1980. doi: 10.1021/ac50062a039.

[81] I. M. P. de Vargas Sansalvador, C. D. Fay, J. Cleary, A. M. Nightingale, M. C. Mowlem, and D. Diamond. Autonomous reagent-based microfluidic ph sensor platform. *Sensors and Actuators B: Chemical*, 225:369 – 376, 2016. ISSN 0925-4005. doi: https://doi.org/10.1016/j.snb.2015.11.057.

[82] A. Lace, D. Ryan, M. Bowkett, and J. Cleary. Arsenic detection in water using microfluidic detection systems based on the leucomalachite green method. *Analytical Methods*, 11(42):5431–5438, 2019. doi: 10.1039/c9ay01580a. cited By 0.

[83] Irish Environmental Protection Agency. Water qualtiy in 2019 – an indicators report, 2020.

[84] J. Wen, K. Shi, Q. Sun, Z. Sun, and H. Gu. Measurement for surface tension of aqueous inorganic salt. *Frontiers in Energy Research*, 6:12, 2018. ISSN 2296-598X. doi: 10.3389/fenrg.2018.00012.

[85] H. Swanson and H. Baldwin. A primer on water quality: Water properties and measurements. *US Geological Survey. Available from: https://www.usgs.gov/special-topic/water-science-school/science/turbidity-and-water [Accessed 10 December 2019]*, 1965.

[86] A. Savitzky and M. J. Golay. Smoothing and differentiation of data by simplified least squares procedures. *Analytical chemistry*, 36(8):1627–1639, 1964.

[87] *ADS111x Ultra-Small, Low-Power, I 2C-Compatible, 860-SPS, 16-Bit ADCs With Internal Reference, Oscillator, and Programmable Comparator*. Texas Instruments, January 2018. URL `http://www.ti.com/lit/ds/symlink/ads1115.pdf`.

[88] American Public Health Association. *4500-NO2 – NITROGEN (NITRITE) (2017)*. doi: 10.2105/SMWW.2882.088.

[89] I. Ogilvie, V. Sieben, C. Floquet, R. Zmijan, M. Mowlem, and H. Morgan. Reduction of surface roughness for optical quality microfluidic devices in pmma and coc. *Journal of Micromechanics and Microengineering*, 20(6):065016, 2010.

[90] M. A. Ansari, K.-Y. Kim, K. Anwar, and S. M. Kim. A novel passive micromixer based on unbalanced splits and collisions of fluid streams. *Journal of micromechanics and microengineering*, 20(5):055007, 2010.

[91] M. N. Almasri and J. J. Kaluarachchi. Assessment and management of long-term nitrate pollution of ground water in agriculture-dominated watersheds. *Journal of Hydrology*, 295(1-4):225–245, 2004.

[92] J. Aubin, D. F. Fletcher, and C. Xuereb. Design of micromixers using cfd modelling. *Chemical Engineering Science*, 60(8-9):2503–2516, 2005.

[93] R. R. Gidde, P. M. Pawar, B. P. Ronge, N. D. Misal, R. B. Kapurkar, and A. K. Parkhe. Evaluation of the mixing performance in a planar passive micromixer with circular and square mixing chambers. *Microsystem Technologies*, 24(6): 2599–2610, 2018.

[94] Y. Liu, Y. Deng, P. Zhang, Z. Liu, and Y. Wu. Experimental investigation of passive micromixers conceptual design using the layout optimization method. *Journal of Micromechanics and Microengineering*, 23(7):075002, 2013.

[95] J. E. Guyer, D. Wheeler, and J. A. Warren. Fipy: Partial differential equations with python. *Computing in Science & Engineering*, 11(3):6–15, 2009.

[96] M. Alnæs, J. Blechta, J. Hake, A. Johansson, B. Kehlet, A. Logg, C. Richardson, J. Ring, M. E. Rognes, and G. N. Wells. The fenics project version 1.5. *Archive of Numerical Software*, 3(100), 2015.

[97] D. Stoecklein, K. Owsley, C.-Y. Wu, D. Di Carlo, and B. Ganapathysubramanian. uflow: software for rational engineering of secondary flows in inertial microfluidic devices. *Microfluidics and Nanofluidics*, 22(7):74, 2018.

[98] M. Shariati-Rad, M. Irandoust, and M. Haghighi. Chemometrics study of the kinetics of the griess reaction. *Journal of Chemometrics*, 28(2):93–99, 2014.

[99] *Griess Reagent Kit for Nitrite Determination (G-7921)*. Molecular Probes, July 2003. URL {http://tools.thermofisher.com/content/sfs/manuals/mp07921.pdf}.

[100] K. Deb, A. Pratap, S. Agarwal, and T. Meyarivan. A fast and elitist multiobjective genetic algorithm: Nsga-ii. *IEEE Transactions on Evolutionary Computation*, 6 (2):182–197, 2002.

[101] F. Pedregosa, G. Varoquaux, A. Gramfort, V. Michel, B. Thirion, O. Grisel, M. Blondel, P. Prettenhofer, R. Weiss, V. Dubourg, et al. Scikit-learn: Machine learning in python. *Journal of machine learning research*, 12(Oct):2825–2830, 2011.

[102] F.-A. Fortin, F.-M. D. Rainville, M.-A. Gardner, M. Parizeau, and C. Gagné. Deap: Evolutionary algorithms made easy. *Journal of Machine Learning Research*, 13(Jul):2171–2175, 2012.

[103] J. D. Hunter. Matplotlib: A 2d graphics environment. *Computing in science & engineering*, 9(3):90, 2007.

[104] B. Gutmann, D. Cantillo, and C. O. Kappe. Continuous-flow technology—a tool for the safe manufacturing of active pharmaceutical ingredients. *Angewandte Chemie International Edition*, 54(23):6688–6728, 2015.

[105] K. Ruiz-Mirazo, C. Briones, and A. de la Escosura. Prebiotic systems chemistry: new perspectives for the origins of life. *Chemical Reviews*, 114(1):285–366, 2014.

[106] Á. I. López-Lorente, M. Valcárcel, and B. Mizaikoff. Continuous flow synthesis and characterization of tailor-made bare gold nanoparticles for use in sers. *Microchimica Acta*, 181(9-10):1101–1108, 2014.

[107] D. Huh, Y.-s. Torisawa, G. A. Hamilton, H. J. Kim, and D. E. Ingber. Microengineered physiological biomimicry: organs-on-chips. *Lab on a Chip*, 12(12): 2156–2164, 2012.

[108] C. T. Culbertson, T. G. Mickleburgh, S. A. Stewart-James, K. A. Sellens, and M. Pressnall. Micro total analysis systems: Fundamental advances and biological applications. *Analytical chemistry*, 86(1):95–118, 2013.

[109] D. J. Kinahan, S. M. Kearney, N. A. Kilcawley, P. L. Early, M. T. Glynn, and J. Ducrée. Density-gradient mediated band extraction of leukocytes from whole blood using centrifugo-pneumatic siphon valving on centrifugal microfluidic discs. *PloS one*, 11(5):e0155545, 2016.

[110] A. Manz, N. Graber, and H. á. Widmer. Miniaturized total chemical analysis systems: a novel concept for chemical sensing. *Sensors and actuators B: Chemical*, 1(1-6):244–248, 1990.

[111] B. Raghuraman, G. Gustavson, R. E. G. V. Hal, E. Dressaire, and O. Zhdaneev. Extended-Range Spectroscopic pH Measurement Using Optimized Mixtures of Dyes. *Applied Spectroscopy*, 60(12):1461–1468, 2006. doi: 10.1366/000370206779321535. URL `https://doi.org/10.1366/000370206779321535`. PMID: 17217597.

[112] P. C. Young. *Recursive estimation and time-series analysis: an introduction*. Springer Science & Business Media, 2012.